ARTICLE TYPE www. rsc.org/xxxxxx | XXXXXXXX

Fundamentals of electro- and thermochemistry in the anode of solid-oxide fuel cells with hydrocarbon and syngas fuels—a review

Jeffrey Hanna,*[a] Won Yong Lee,[a] Yixiang Shi,[b] and Ahmed F. Ghoniem[a]

Received Xth XXXXXXXXXX 20XX, Accepted Xth XXXXXXXXX 20XX
First published on the web Xth XXXXXXXXXX 200X
DOI: 10.1039/b000000x

High fuel flexibility of solid-oxide fuel cells (SOFCs) affords the possibility to use relatively cheap, safe, and readily available hydrocarbon (*e.g.*, CH_4) or coal syngas (*i.e.*, CO-H_2 mixtures) fuels. Utilization of such fuels would greatly lower fuel cost and increase the feasibility of SOFC commercialization, especially for near-term adoption in anticipation of the long-awaited so-called "hydrogen economy." Current SOFC technology has shown good performance with a wide range of hydrocarbon and syngas fuels, but there are still significant challenges for practical application. In this paper, the basic operating principles, state-of-the-art performance benchmarks, and SOFC-relevant materials are summarized. More in-depth reviews on those topics can be found in Kee and co-workers [*Combust. Sci. and Tech.*, 2008, **180**, 1207–1244 and *Proc. Combust. Inst.*, 2005, **30**, 2379–2404] and McIntosh and Gorte [*Chem. Rev.*, 2004, **104**, 4845–4865]. The focus of this review is on the fundamentals and development of detailed electro- and thermal (or simply, electrothermal) chemistry within the SOFC anode, including electrochemical oxidation mechanisms for H_2, CO, CH_4, and carbon, as well as the effects of carbon deposition and sulfur poisoning. The interdependence of heterogeneous chemistry, charge-transfer processes, and transport are discussed in the context of SOFC-membrane-electrode assembly (MEA) modeling.

Contents

1 Introduction

Solid-oxide fuel cells (SOFCs) are the most efficient devices known to convert the chemical energy of a fuel directly into electricity.[1] Research on SOFCs is vast, and their development has been long and continuous, primarily because these devices carry a set of attractive features.[1–17] SOFCs (and other fuel cells) offer high conversion efficiencies and an environmentally friendly alternative to modern combustion-based systems, but their high operating temperature (600–1000°C) allows greater fuel flexibility than most other fuel cells (though materials selection and sealing can be an issue at very high temperatures).

The high fuel flexibility of SOFCs affords the possibility to use relatively cheap, safe, and readily available carbon-based fuels instead of hydrogen. Additionally, CO_2 capture in SOFC-based systems can be achieved at lower cost and lower system complexity than in conventional combustion systems, because the fuel and oxidizer in a SOFC are not in direct contact as in traditional combustion processes. This facilitates CO_2 sequestration without the need for expensive gas-separation technologies.

Despite the apparent promise and advantages of SOFC as an energy-conversion technology, several obstacles must be overcome before SOFCs move beyond the early stages of commercialization. For example, improving efficiencies without the use of precious metal catalysts, finding catalysts with higher tolerances to fuel impurities, preventing deactivation of the anode as a result of carbon deposition when using carbon-based fuels, long-term operational reliability and durability, sealing problems, stack and system integration issues, and overall production costs.

A comprehensive review on the operating principles, performance, and current challenges associated with SOFCs utilizing hydrocarbon and syngas fuels can be found in Kee and co-workers[6,7] and McIntosh and Gorte.[18] In this paper, we provide a further review on the research and developmental status of typical hydrocarbon- or coal-syngas-fueled SOFCs by focusing on the following topics:

- fundamental mechanisms of electrode chemical and electrochemical reactions, specifically in the anode;
- anode materials, particularly in the context of carbon deposition and tolerance to sulfur poisoning;
- coupling of electro- and thermochemistry with transport in physics-based models of SOFC membrane-electrode assemblies (MEAs).

[a] *Department of Mechanical Engineering, Massachusetts Institute of Technology, Cambridge, MA 02139, USA. Fax: +1 617-253-5981; Tel: +1 617-253-2411; E-mail: jfhanna@mit.edu*
[b] *Department of Thermal Engineering, Tsinghua University, Beijing 100084, China.*

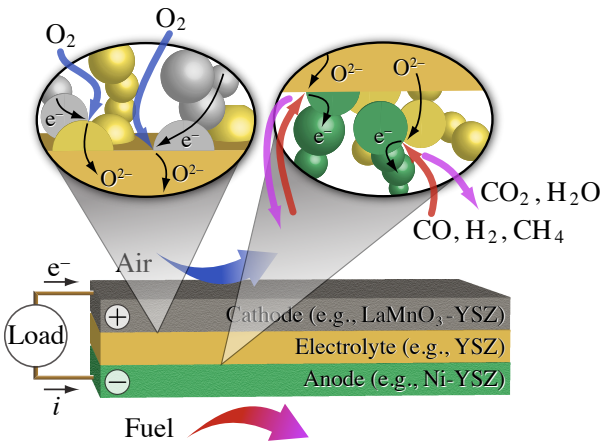

Fig. 1 The basic operating principles in a SOFC membrane-electrode-assembly (MEA). In the left bubble, oxygen molecules are reduced at the cathode and the oxygen ions are conducted through the electrolyte. The oxygen ions move through the electrolyte into the anode (right bubble), where they are used for electrochemical oxidation of fuel at the three-phase boundary (TPB). Electrons released in the charge-transfer reactions are conducted through the anode (metal), to the external circuit.

A better understanding of these topics is essential for further improvement and optimization of SOFCs operating on hydrocarbon or coal-derived fuels.

2 Operating principles and materials

The electrochemical charge-transfer reactions and some of the thermochemical (reforming) reactions in a SOFC take place in the membrane-electrode assembly (MEA) as shown in Fig. 1. At the positive electrode (cathode), oxygen is reduced to generate oxygen ions O^{2-}, which are conducted through the electrolyte to the negative electrode (anode), where they electrochemically oxidize the fuel (*e.g.*, CO, H_2, CH_4) to produce electrons, which flow through the external electrical circuit generating a current. During this process, the Gibbs free energy (or chemical potential energy) of the global reaction of fuel and oxidizer is converted into electricity and heat.

2.1 Requirements of the membrane-electrode assembly

The membrane-electrode assembly (MEA) is the heart of any fuel cell. In a SOFC, the MEA consists of a dense oxygen-ion-conducting electrolyte sandwiched between two porous electrodes. On the anode side, gas species in the fuel channel are transported through the porous cermet network of the electrode to electrochemically reactive sites known as triple- or three-phase boundaries (TPBs). It is generally accepted that current-producing charge-transfer reactions only occur at or

very near the TPB, where the electron conductor (metal), ion conductor (oxide), and necessary gas-phase reactants (in the pore space) come together. Each phase is necessary for the transport of reactants to or removal of products from the reactive site. The interdependence of heterogeneous chemistry, charge-transfer reactions, and transport (ion, electron, and gas phase)—and the influence of electrode microstructure on these processes—determine the rate and ability of the cell to deliver current.

The basic operating principles of SOFCs determine key requirements for each component. For instance, the electrolyte should possess maximum ionic conductivity and minimum electronic transport over a wide range of oxygen chemical potentials at relatively high temperature. The anode and cathode should possess high catalytic activity for fuel oxidation and oxygen reduction, respectively. In addition, the porous electrodes should be designed with appropriate microstructure to provide an abundance of chemical and electrochemical reaction sites (to promote charge-transfer), high solid-phase connectivity (for electron and ion conduction), and a connected pore network (to reduce limitations of mass transport).[19–21] If one tries to produce a high-porosity cermet, the result may be low connectivity between the solid phases and therefore low electrochemical activity; if one tries to create more surface area for electrochemistry by creating smaller pores, the result is hindered gas transport. SOFC components should also be mechanically and chemically compatible, and should be stable under fabrication and operating conditions. These requirements and other considerations (*e.g.*, material degradation issues) are the key driving forces for continued studies on SOFC materials.

2.2 Common SOFC electrolyte and electrode materials

As one of the core components of the MEA, the electrolyte is usually made of a dense solid metal-oxide. One of the most common electrolyte materials in SOFCs is yttria-stabilized zirconia (YSZ)—zirconia (ZrO_2) with 8% yttrium added as a dopant. In the temperature range 650–1000°C, YSZ is a good conductor of oxygen ions, O^{2-}.[1] In addition, a number of novel ionic conductors have been studied (for a brief review, the reader is referred to Ref. 10), *e.g.*, $La_{1-x}Sr_xGa_{1-y}Mg_yO_{3-(x+y)/2}$ (LSGM)-based perovskites; $La_2Mo_2O_9$ (LAMOX); $Bi_4V_{2-x}M_xO_{11-y}$ (BIMEVOX); several pyro-chlores with relatively high ionic transport, such as $(Gd,Ca)_2Ti_2O_{7-\delta}$; apatite materials derived from $Ln_{10-x}Si_6O_{26\pm\delta}$, where Ln represents a lanthanide-series element, collectively known as rare-earth elements;[16] as well as proton-conducting materials, which allow for a significant decrease in operating temperature while improving performance.[22] Moreover, gadolinia-doped ceria (GDC), samaria-doped ceria (SDC), and other ceria-based electrolytes have received a great deal of attention because of their ability to conduct oxygen ions at lower temperatures than YSZ.[23–27]

The cathode in SOFCs is usually composed of porous perovskite materials, which are oxides characterized by relatively good electronic conduction at high temperatures in an oxidizing atmosphere. The most widely used cathode materials in SOFCs are strontium-doped lanthanum manganite ($La_{1-x}Sr_xMnO_3$, or LSM), strontium-doped lanthanum colbaltite ($La_{1-x}Sr_xCoO_{3-\delta}$, or LSC), the relatively novel strontium-doped lanthanum ferrite ($La_{1-x}Sr_xFeO_{3-\delta}$, or LSF), and strontium-doped lanthanum cobalt ferrite ($La_{1-x}Sr_xCo_{1-y}Fe_yO_{3-\delta}$, or LSCF).[13] These cathode materials act as mixed ionic-electronic conductors (MIECs), which eliminates the need for a metal to serve as an electrocatalyst and current collector. Unfortunately, many of the cathode materials are excellent for applications in an oxidizing atmosphere, but are subject to reduction by the fuel of an SOFC and therefore cannot be used on the anode side.

SOFC anodes are generally porous ceramic-metallic (cermet) composites of an electrolyte (*e.g.*, YSZ) and a metal (such as nickel, Ni). The metal acts as a catalyst to promote fuel oxidation, and serves as an electronic conductor; while YSZ serves to conduct O^{2-} ions up into the porous anode, effectively extending the TPB region, and provides a support structure to prevent the sintering of nickel.[12,17] The YSZ also helps to closely match the thermal-expansion coefficients of the anode and electrolyte, preventing cracking and leakage caused by thermal cycling. To convert hydrocarbon fuels, Cu is preferred because of its resistance to carbon deposition, and ceria-based oxides (*e.g.*, $Ce_{1-x}Gd_xO_{2-\delta}$, or GDC) are commonly used because ceria is an excellent electrocatalyst for CH_4 (in addition to being a good oxygen-ion conductor at reduced temperatures).[8,28,29] When using natural gas or coal syngas as a fuel, possible homogeneous gas-phase reactions occurring within the anode include methane reforming, the water-gas shift (WGS), methane cracking, the Boudouard reaction, and CO hydrogenation.

Porous Ni-YSZ cermets (and small variations thereof) are currently the most common anode material used for SOFC applications because of their low cost, chemical stability in reducing atmospheres at high temperatures, and closely matched thermal-expansion coefficients with the dense YSZ electrolyte. In addition, nickel and YSZ are essentially immiscible in each other and non-reactive over a wide temperature range. This enables relatively simple preparation of Ni-YSZ anodes by sintering a mixture of NiO and YSZ powders (generally in the range of NiO:YSZ = 1:1 by weight), then reducing in an atmosphere of the gaseous fuel. However, the Ni-YSZ anode is especially prone to carbon deposition when using carbon-based fuels, and exhibits low tolerance to sulfur. Additional drawbacks include low oxidation/reduction cycling stability, and nickel agglomeration with

long-term operation.[14,15,18,30,31] Nickel is an excellent catalyst for hydrocarbon fuel reforming, shifting, and cracking, which leads to rapid carbon deposition inside the SOFC anode and causes coking and deactivation at desired operating temperatures. To some extent, optimizing SOFC operating conditions can avoid carbon deposition. For example, increasing steam content can suppress carbon deposition by steam reforming and WGS reactions. Also, reducing the operating temperature below 750°C can prevent carbon deposition on many oxides by disabling CH_4 dissociation.[24] Recent work has shown that nanostructured barium-oxide/nickel (BaO/Ni) interfaces (created by vapor deposition of BaO into Ni-YSZ) facilitate water-mediated carbon-removal reactions.[32] The nanostructures readily adsorb water, and the dissociated OH_{ad}(BaO) from H_2O_{ad}(BaO) reacts with C_{ad}(Ni) near the BaO/Ni interface to produce CO and H species, which can be electrochemically oxidized at the TPB in the anode. The BaO/Ni-YSZ anode displayed stable operation and high power density in C_3H_8, CO, and gasified carbon fuels at 750°C, with no observable microstructural change and minimal carbon buildup.

In recent years, researchers have rigorously investigated SOFC performance with different fuels, including hydrogen, hydrocarbons, and syngas, and with various material and support structures. Table 1 shows selected examples of cell performance from recent studies, which provides a representation of the state-of-the-art research and developmental status of SOFCs fueled with hydrogen, hydrocarbon, or syngas. Because materials are important for chemistry and electrochemistry, additional details of anode material development with hydrocarbon and syngas fuels will be discussed in the next section.

3 Modeling of SOFC membrane-electrode assemblies

Detailed physics-based models are important for fuel cell development because they afford the opportunity to study each process independently, as well as how one process is connected to the others. It is difficult to study them experimentally in porous electrodes because of, among other challenges, physical access limitations to inner regions of the electrode. The fundamental conservation equations (*e.g.*, momentum, energy, and species transport) that underlie all models are more or less the same, but the detailed formulations and implementations vary widely based on general assumptions and modeling specifics.

Single-cell or MEA models are critical for informing larger macroscale models, but they are also highly useful in interpreting and planning button-cell-type experiments, investigating rate-limiting processes, and exploring the impact of electrode microstructure on fuel cell performance. Many of these models employ elementary chemistry and electrochemistry coupled with complex porous-media transport in the electrodes. The level of detail in such a model can vary widely, from detailed elementary reaction mechanisms for heterogeneous chemistry[40,41] and charge-transfer[42–46] (each formulated from more specific chemical-kinetics models and pattern-anode experiments), to reduced Butler-Volmer representations based on an assumed rate-limiting or global reaction;[47–49] and from particle-level representations of the electrode microstructure,[50] to averaged homogenized parameters describing its structure. Just as well, because porous-media transport plays a central role in the performance in SOFCs, approaches to modeling mass transfer are also widely varied. Due to the level of detail and physically-based foundation of the MEA-type models, they can provide excellent predictive capabilities that can be used for SOFC design and optimization.

The coupling and incorporation of electro- and thermochemistry with species transport into physics-based models are discussed below. The discussion introduces the equations that need to be solved and terms to be evaluated based on chemical and electrochemical kinetics. The fundamental equations can be solved if the species' (neutral and charged) production rates are known. These rates are determined by the mechanisms discussed in the second half of this paper.

3.1 Equilibrium, open-circuit, or Nernst potential

The reversible cell potential (Nernst potential) E_{rev} between the fuel and oxidizer streams is the theoretical maximum potential difference the cell could achieve for a given fuel composition. Because of depletion and dilution of the fuel and oxidizer streams, this potential can vary along the length of the cell. The Nernst potential is calculated as

$$E_{\text{rev}} = -\frac{\Delta_r G}{n_e F} = -\frac{\Delta G^\circ}{n_e F} - \frac{RT}{n_e F} \ln\left(\prod_k p_k^{\nu_k}\right) \qquad (1)$$

where $\Delta_r G$ and ΔG° are the temperature-dependent Gibbs free energy of reaction and standard-state free energy change, respectively, associated with the global oxidation reaction, n_e is the number of transferred electrons, $F = 96485.34$ C/mol is the Faraday constant, R is the universal gas constant, T is the temperature, p_k is the partial pressure of species k (in atmospheres), and ν_k are the stoichiometric coefficients in the global reaction (with $\nu_k < 0$ for reactants). Assuming chemical equilibrium exists for species in the anode channel, $\prod_k p_{k,a}^{\nu_{k,a}} = K_p = \exp(-\Delta G^\circ / RT)$, where K_p is the thermodynamic equilibrium constant. The Nernst potential can therefore be written in terms of the oxygen partial pressures in the anode and cathode channels

$$E_{\text{rev}} = |\nu_{O_2}| \frac{RT}{n_e F} \ln\left(\frac{p_{O_2,c}}{p_{O_2,a}}\right) \qquad (2)$$

Table 1 Impact of fuel and MEA materials on SOFC performance

Research group	MEA composition (*a*/el/*c*) [a]	T (°C)	Fuel composition	P_{peak} (W/cm^2)
Jiang and Virkar, 2003 (Ref. 33)	Ni-YSZ/YSZ-SDC/LSC-SDC	800	Pure H_2	1.8
		800	Pure CO	0.7
Liu and Barnett, 2003 (Ref. 34)	Ni-YSZ/YSZ/LSM-YSZ	800	CH_4+3% H_2O	0.96
Lin, Zhan, Liu, and Barnett, 2005 (Ref. 35)	Ni-YSZ/YSZ/(LSCF-GDC/LSCF)	800	H_2+3% H_2O	1.44
		800	CH_4+3% H_2O	1.27
Shao, Mederos, Chueh, and Haile, 2006 (Ref. 36)	Ni-SDC/SDC/SDC-BSCF (single chamber cell)	787	18.8% CH_4+16.2% O_2 +65% He (by vol.)	0.76
Hibino *et al.*, 2003 (Ref. 37)	Ru-Ni-GDC/GDC/SSC [b]	600	H_2+2.9% H_2O	0.769
		600	Dry CH_4	0.750
		600	Dry C_2H_6	0.716
		600	Dry C_3H_8	0.648
Park, Vohs, and Gorte, 2000 (Ref. 38)	Cu-CeO_2-YSZ/YSZ/LSM-YSZ (electrolyte supported)	800	Pure H_2	0.31
		800	*n*-C_4H_{10}	0.18
Zhan and Barnett, 2005 (Ref. 39)	NiO-YSZ/YSZ/(LSCF-GDC/LSCF) with an anode catalyst layer of Ru-CeO_2/PSZ/Ru-CeO_2	770	5% *iso*-C_8H_{18}+9% air +86% CO_2	0.6
Zhan and Barnett, 2006 (Ref. 26)	NiO-SDC/SDC/(LSCF-SDC/LSCF) with an anode catalyst layer of Ru-CeO_2/PSZ-CeO_2/Ru-CeO_2	600	H_2+3% H_2O	1.00
		590	6% *iso*-C_8H_{18}+94% air	0.60
Yang *et al.*, 2011 (Ref. 32)	(BaO/Ni-YSZ)/YSZ/(SDC buffer layer/LSCF)	750	Dry C_3H_8	0.88
		750	CO+3% H_2O	0.70
		850	96% CO+1% H_2 +H_2O, CO_2, and CH_4 [c]	1.08

[a] The membrane-electrode assembly (MEA) composition follows as "*a*" for anode/"el" for electrolyte/"*c*" for cathode. All cells are anode supported unless otherwise noted.
[b] The cathode material is $Sm_{0.5}Sr_{0.5}CoO_3$ (SSC).
[c] This fuel mixture was produced using an integrated fluidized-bed gasifier operating with solid carbon and CO_2+3% H_2O.

where $|\nu_{O_2}|$ is the absolute value of the stoichiometric coefficient for oxygen, and $p_{O_2,c}$ and $p_{O_2,a}$ are the partial pressures of oxygen (in atmospheres) at the cathode and anode (subscripts c and a), respectively. The anodic partial pressure $p_{O_2,a}$ is determined by equilibrium chemistry in the anode fuel channel. Note that regardless of which oxidation reaction is taking place, the number of electrons per mole of oxygen is constant (*i.e.*, $n_e/|\nu_{O_2}| = 4$). This is because the stoichiometry is set by the cathodic reduction reaction, and is independent of fuel type (and therefore, the anodic half-cell reaction). The influence of the anodic chemistry and electrochemistry appears indirectly through the anode oxygen partial pressure $p_{O_2,a}$.

The overall half-cell reduction-oxidation (redox) reactions for four typical fuels (anode) and oxygen (cathode) can be written as

Anode half-cell oxidation reactions:

$$H_2(g) + O^{2-}(\text{el}) \rightleftharpoons H_2O(g) + 2e^-(a) \quad (3)$$

$$CO(g) + O^{2-}(\text{el}) \rightleftharpoons CO_2(g) + 2e^-(a) \quad (4)$$

$$CH_4(g) + 4O^{2-}(\text{el}) \rightleftharpoons CO_2(g) + 2H_2O(g) + 8e^-(a) \quad (5)$$

$$C(s) + 2O^{2-}(\text{el}) \rightleftharpoons CO_2(g) + 4e^-(a) \quad (6)$$

Cathode half-cell reduction reaction:

$$O_2(g) + 4e^-(a) \rightleftharpoons 2O^{2-}(\text{el}) \quad (7)$$

Note that this nomenclature uses generic names in place of specific material names (*i.e.*, "el" for electrolyte instead of "YSZ"); both will be used in this paper. To make the Nernst

equation concrete, consider the case of CO electrochemical oxidation, for which the global oxidation reaction is

$$\mathrm{CO}(g,a)+\frac{1}{2}\mathrm{O_2}(g,a)\rightleftharpoons \mathrm{CO_2}(g,a)$$

The reversible potential follows as

$$E_{\mathrm{rev}}=\frac{RT}{2F}\ln\left(\frac{p_{\mathrm{O_2},c}^{1/2}}{p_{\mathrm{O_2},a}^{1/2}}\right)=\frac{RT}{4F}\ln\left(\frac{p_{\mathrm{O_2},c}}{p_{\mathrm{O_2},a}}\right)$$

The approach to computing the reversible cell potential in Eq. 1 or Eq. 2 is not obvious when many different global oxidation reactions can be written. For example, consider the case of full or partial oxidation of methane, (*i*) $CH_4 + 2O_2 \rightleftharpoons CO_2 + 2H_2O$ or (*ii*) $CH_4 + (1/2)O_2 \rightleftharpoons CO + 2H_2$, followed by oxidation of carbon monoxide and hydrogen, $CO + (1/2)O_2 \rightleftharpoons CO_2$ and $H_2 + (1/2)O_2 \rightleftharpoons H_2O$. It is not obvious which, if any, should be used to calculate E_{rev}, and the answer depends on which of the anode-side half reactions is in partial equilibrium. If even a small amount of H_2 is present in the fuel stream, reaction 3 is likely to be close to partial equilibrium at open circuit, since the elementary steps that comprise this global half reaction are all fast and reversible.[7] Even if the entering fuel stream contains no H_2, it may be generated in situ within the anode by catalytic cracking, reforming, and/or shifting chemistry with a hydrocarbon fuel. The open-circuit voltage (OCV) will therefore generally be close to the reversible potential for hydrogen oxidation, and not the higher value that would be obtained for the global hydrocarbon-oxidation reaction.[7]

Fig. 2 shows the calculated reversible cell potential of different fuels over a range of temperatures using Eq. 2. The results indicate that the reversible cell potential from the oxidation of H_2 (top left panel) or CO (top right) decreases with a higher system temperature and increases with a higher system pressure. Alternatively, the reversible cell potential from the *full* oxidation of CH_4 (bottom left, straight lines) or solid carbon (bottom right, slight negative-sloping line) is pressure independent. The influence of controlling oxidation reaction on the OCV is illustrated graphically in the bottom two panels. For both, the curves (as opposed to the straight lines) are calculated assuming all anode-side half reactions are in partial equilibrium, so the fuel stream is in a state of full chemical equilibrium and the reversible potential is calculated according to Eq. 2 using the equilibrium anode-side oxygen partial pressure. For methane oxidation, it is immediately evident that full oxidation (straight lines) of CH_4 determines the OCV at lower temperatures, while partial oxidation (not shown) of CH_4 is correlated to the positive-sloping behavior at higher temperatures and higher methane partial pressures. Moreover, oxidation of H_2 contributes to the decreasing OCV at higher temperatures and higher product partial pressures. For the electrochemical oxidation of solid carbon, the competing oxidation mechanisms and their influence on the reversible cell potential are very clear—at lower temperatures, full oxidation to CO_2 is favored, while partial oxidation to CO is preferred at higher temperatures.

3.2 Current-dependent overpotentials

Under operating conditions, the actual operating cell voltage E_{cell} will be reduced from the open-circuit potential by several irreversibilities. These irreversibilities are associated with various internal losses (polarizations), each characterized as a voltage loss (overpotential). Common losses include the ohmic polarization loss η_{ohm} due to electronic and ionic resistivities; activation polarization losses (at the anode $\eta_{\mathrm{act},a}$ and cathode $\eta_{\mathrm{act},c}$) due to reaction barriers and charge-transfer limitations; concentration polarization losses (at the anode $\eta_{\mathrm{conc},a}$ and cathode $\eta_{\mathrm{conc},c}$) due to spatial variations in reactant and product concentrations at chemically active sites (controlled by gas-phase transport); and other losses η_{other} from mechanical contact resistance between the electrodes and the electrolyte structure, current leakage, leakage of oxygen from the cathode to the anode due to inadequate sealing, and so on. In terms of current-dependent overpotentials, the operating cell potential may be written as

$$\begin{aligned}E_{\mathrm{cell}} = E_{\mathrm{rev}} &-\eta_{\mathrm{act},a}(i)-\eta_{\mathrm{conc},a}(i)-\eta_{\mathrm{ohm}}(i)\\ &-\eta_{\mathrm{act},c}(i)-\eta_{\mathrm{conc},c}(i)-\eta_{\mathrm{other}}(i)\end{aligned}\qquad(8)$$

Each of the overpotentials increases with increasing current density i, so the difference $E_{\mathrm{rev}}-E_{\mathrm{cell}}$ also increases (*i.e.*, as the cell delivers higher current, the internal losses increase, and the operating potential moves further from the reversible potential). The limiting current is reached when the sum of the internal losses equals the reversible potential and $E_{\mathrm{cell}} = 0$. Moreover, each of the overpotentials can be obtained from MEA models, facilitating a better understanding of the sources of loss and how to minimize them.

There are inherent limitations to beginning with the Nernst potential and subtracting various overpotentials according to Eq. 8, namely its application to equilibrium fuel mixtures only (*e.g.*, it cannot be applied to non-equilibrated CH_4-H_2O mixtures) and the required Butler-Volmer assumption used to compute an activation overpotential (which disallows the use of a full elementary kinetic description of the electrochemistry). However, this traditional view of fuel-cell function has practical utility in developing predictive models, and provides a platform to research, characterize, and understand each of the polarization losses. The reader is referred to Kee and coworkers[47,48,52] for an explanation and discussion of each of the overpotentials. We provide an overview of the concentration and ohmic overpotentials in Appendix A.

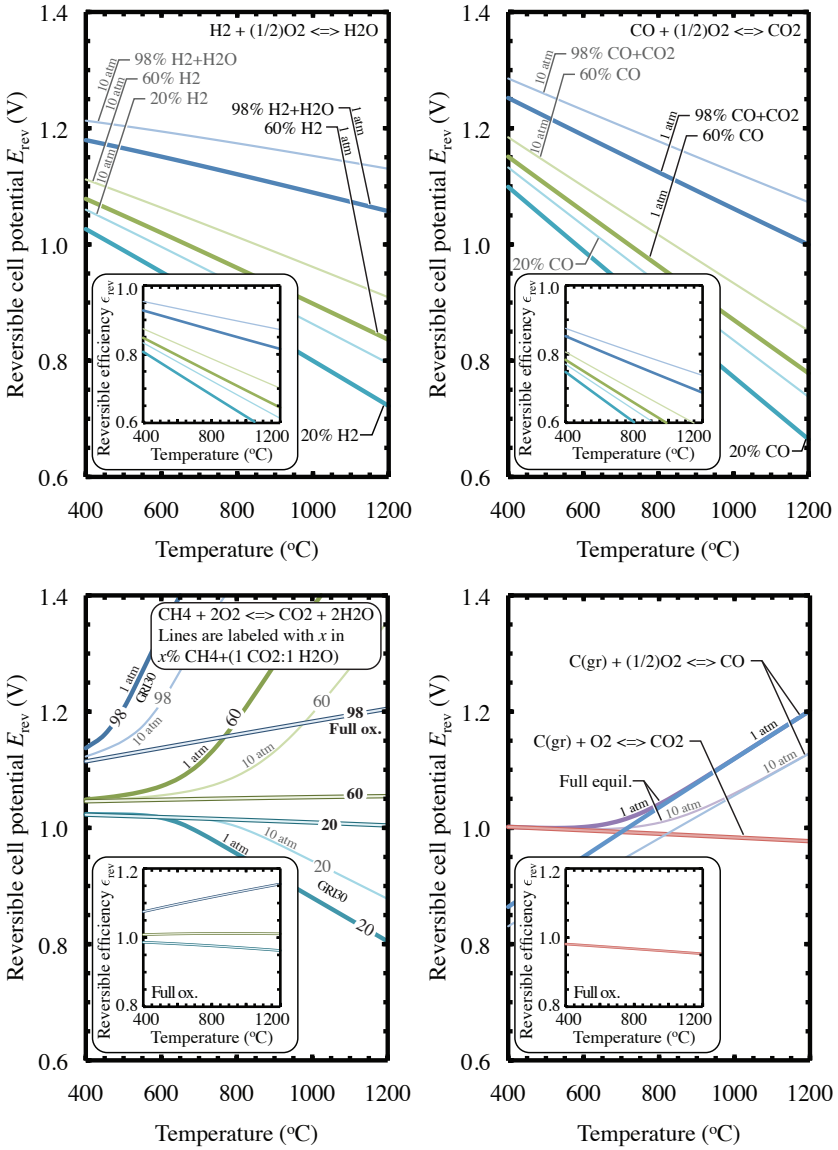

Fig. 2 Reversible cell potentials E_{rev} (or open-circuit voltages OCV) and thermodynamic efficiencies ε_{rev} (insets) for different fuels over a range of temperatures at pressures of 1 atm (thick lines) and 10 atm (thin lines). The fuel streams are equilibrated mixtures of the indicated ratios for fuel and oxidation products—as the fuel becomes more diluted, think of this as being representative of moving along the flow channel. The OCV is calculated assuming air as the oxidant. The reversible efficiency is calculated from $\varepsilon_{rev} = \Delta_r G/\Delta_r H = |\nu_{O_2}|(RT/\Delta H^\circ)\ln(p_{O_2,a}/p_{O_2,c}) = -n_e F E_{rev}/\Delta H^\circ$, where ΔH° is the temperature-dependent standard-state enthalpy change associated with the global oxidation reaction. For ease of comparison, all plots use the same horizontal and vertical scaling (the insets do not). The top left panel is for H_2 electrochemical oxidation, top right for CO electrochemical oxidation, bottom left for electrochemical oxidation of CH_4, and bottom right for electrochemical oxidation of solid graphitic carbon C(gr). For methane oxidation, the straight lines give the OCV calculated assuming full oxidation of methane to CO_2 and H_2O (pressure independent), and the curves give the OCV from a full equilibrium calculation using the GRI30 mechanism in Cantera.[51] Reversible efficiencies are calculated based only on the full oxidation of methane. For carbon oxidation, the two straight lines assume oxidation to CO only (positive slope) or CO_2 only (slight negative slope and independent of pressure) over the entire temperature range, whereas the curved line accounts for the thermodynamically favored oxidation product (which shifts from CO_2 at lower temperatures, to CO at higher temperatures).

Fig. 3 illustrates the dependence of cell voltage and power density on current density for a fuel mixture of 50% H_2 in H_2O. The shaded areas elucidate the relative magnitudes and contributions of the various overpotentials plotted in a cumulative fashion (*i.e.*, each overpotential appears as its value plus the sum of overpotentials below it). In other words, the top of the shaded region is a quantitative measure of the total amount of available chemical potential that is used to overcome internal losses, decreasing the cell potential from its open-circuit value. The curves are calculated using a one-dimensional anode-supported MEA model already described in the literature.[47–49] Because the cathode is very thin, the cathode concentration overpotential is essentially zero. Different MEA structures will have different characteristic overpotentials and performance curves based on materials and fabrication (*e.g.*, see Ref. 53), microstructure (*e.g.*, see Ref. 44), and operating conditions (*e.g.*, see Ref. 33)—for an experimental investigation of these effects, see Ref. 54. Nonetheless, the principles remain the same. At open circuit (*i.e.*, no current flow), the cell potential is given by the Nernst potential. As the current density increases, so too do the overpotentials, until the total losses equal the Nernst potential. At this current, the cell voltage and power go to zero. This is known as the limiting current density and occurs when all the available chemical potential is used to overcome internal losses. Generally, at low currents, the cell response is dominated by charge-transfer reaction kinetics quantified by the activation overpotentials. The linear central portion of the cell voltage curve is often attributed to ohmic losses, while the concentration overpotentials affect the shape of the curve at high current densities (and are therefore typically responsible for limiting the maximum attainable current from the cell). At high current densities, reactants are quickly used in charge-transfer reactions and new reactants cannot be sufficiently supplied through the phases of the porous electrodes.

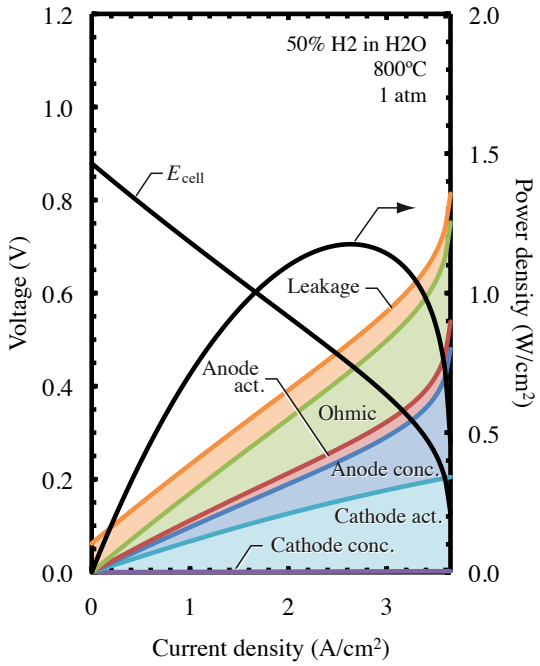

Fig. 3 Dependence of cell voltage, overpotentials, and power density on current density. Each of the overpotential curves is illustrated in a cumulative fashion, meaning that overpotential is added to the sum of overpotentials appearing below it. The curves are calculated using a one-dimensional MEA model described in Ref. 48 with modified transport parameters and constant leakage overpotential $\eta_{leak} = 0.0618$ V from Ref. 49. The physical parameters describing the structure of the anode-supported MEA are described in the aforementioned references and based on button-cell experiments from Ref. 33. The anode is a porous Ni-YSZ cermet that is 1.22 cm thick; the electrolyte is dense YSZ that is 25 μm thick; and the cathode is a 30 μm thick porous LSM structure. A modified Butler-Volmer formulation is used based on an assumption that $H(Ni) + OH^-(YSZ) \rightleftharpoons (Ni) + H_2O(YSZ) + e^-(Ni)$ is the rate-limiting charge-transfer step.

3.2.1 Activation overpotential. Because the electrodes are electronic conductors and the electrolyte is an ionic conductor, the charge cannot directly move between the electrode and electrolyte. Alternatively, one or more electrochemical charge-transfer reactions are needed. Since the electrodes and the electrolyte all have free charge carriers, each one is, to a good approximation, internally charge neutral, with any excess charge being distributed on its surface. The interface behaves as a capacitor, with buildup of excess charge on one side of the interface and equal but opposite charge on the other. The very thin (nanometer scale) region at the interface where charge is stored is termed the electric double layer, and the electric potential varies sharply in this region. As electrons are transported across the double-layer region, charge-transfer reactions must overcome the potential difference from one side to the other. The electric potential difference between the electrode and electrolyte $E_i = \Phi_i - \Phi_{e,i}$ is written in terms of the electrode potential Φ_i and the potential within the electrolyte $\Phi_{e,i}$ just outside the double-layer region at the electrode/electrolyte interface. Here, as before, i is used as a general index to indicate "a" for anode or "c" for cathode. This potential difference less the equilibrium potential difference E_i^{eq} (*i.e.*, the potential difference with no net current flow) is the activation overpotential $\eta_{act,i} = E_i - E_i^{eq}$. Other than being a function of current density, the activation overpotential depends on charge-transfer kinetics, which are sometimes controlled by surface diffusion or adsorption/desorption reactions.

Charge-transfer processes are among the least understood aspects of fuel cell chemistry. A number of charge-transfer mechanisms have been proposed in the literature, even for the

relatively simple electrochemical oxidation of pure H_2, and many of these are discussed in the sections to follow. The main focus of this paper concerns the electrochemistry of H_2, CO, and syngas mixtures. A hydrocarbon fuel is generally reduced to these active species through reforming and shifting processes (internal or external of the anode) and/or partial oxidation reactions within the anode. For fuels containing only a small amount of H_2, it is generally assumed that the hydrogen electro-oxidation pathway is dominant.[48] Although this is a nearly universal assumption in SOFC modeling, it is also well known that cells can run on pure CO.[33] Zhu *et al.*[48] noted that as the incorporation of elementary electrochemistry into SOFC modeling advances, it will be important to include multiple competing charge-transfer pathways in the electrochemical reaction mechanism.

In general, proposed mechanisms are either used (*i*) to support experimental observations by structure, *e.g.*, dependence on global oxidation reaction species partial pressures, or identifying the anodic and cathodic charge-transfer coefficients from Tafel plots; or (*ii*) to be predictive tools, in which case the kinetic parameters must be known for all reactions in the mechanism. Models that incorporate detailed multistep electrochemistry consisting of elementary reactions involving only a single transferred electron with no *a priori* assumption about a rate-limiting process (*e.g.*, see Refs. 42–46) will almost certainly be necessary when multiple competing charge-transfer pathways are open. Some modeling efforts consider only a global charge-transfer process;[55] while others begin with a detailed multistep mechanism, but reduce the full mechanism to a single rate-limiting step and derive a Butler-Volmer formalism[56] by assuming all other reactions are in equilibrium.[20,21,47–49,57,58]

The activation overpotentials quantify the polarization losses in each electrode due to charge-transfer limitations and reaction barriers. Just as the reactants in a chemical reaction process must overcome an energy barrier, *i.e.*, the activation energy, the reactants in charge-transfer electrochemical reactions must overcome not only a thermal energy barrier, but also an electric potential.[47] Temperature-dependent rate constants for a chemical reaction are typically expressed using an Arrhenius relation of the form $k = AT^n \exp(-E/RT)$, where A is a pre-factor and E is the activation energy. Similarly, the rate expressions for an electrochemical reaction can be written generally as

$$k = AT^n \exp(-E/RT) \exp\left(\pm\alpha \frac{n_e F \eta_{\mathrm{act},i}}{RT}\right), \qquad (9)$$

where A is again a pre-factor, E the activation energy, n_e the number of electrons transferred in the reaction, F is Faraday's constant, and $\eta_{\mathrm{act},i}$ is the activation overpotential for electrode i. The sign of the argument in the last exponential is positive if the reaction proceeds in the anodic direction (*i.e.*, the reaction produces electrons) and negative if the reaction proceeds in the cathodic direction (consuming electrons). The parameter α is usually called a charge-transfer coefficient, the asymmetry factor, or conversely, the symmetry factor. Its value sets the fraction of overpotential barrier height to the charge-transfer reaction in the anodic and cathodic directions. For elementary reactions transferring a single electron, it is common to write α as β, the latter of which are constrained by $\beta_c = 1 - \beta_a$, where subscripts "a" and"c" indicate the anodic or cathodic reaction directions, respectively. For a reaction transferring more than one electron, α_a and α_c are not so simply related.[52]

3.3 Role of electrochemistry in SOFC anode models

The discussion in this section centers around approaches to representing charge-transfer chemistry in models of SOFC electrodes, particularly the anode. It is worthwhile to mention these approaches before reviewing various electrochemical oxidation mechanisms to provide a baseline for the type of data needed and the different ways of using that data.

3.3.1 Formulation for detailed kinetics. For any phase p (*e.g.*, gas, anode surface, oxide surface), complex chemical, electrochemical, and transport interactions are linked through a reaction-diffusion equation

$$\frac{\partial [X_k]}{\partial t} = -\nabla \cdot \mathbf{J}_k + \dot{s}_{p,k} + \sum_{q \neq p} \gamma_q \dot{s}^{\sim}_{q,k}, \quad k = 1, 2, ..., K_p \qquad (10)$$

where k is a species in phase p of the K_p that are assumed to exist. The term $\mathbf{J}_k$ is the net molar flux vector for species k, $\dot{s}_{p,k}$ is the production rate of k due to reactions taking place in phase p, and $\dot{s}^{\sim}_{q,k}$ is the production rate of k due to reactions taking place in phase q. The final term is summed over all phases q in which k participates in any reactions associated with that phase. These production rates are multiplied by a length scaling factor γ_q, having units of inverse length (*e.g.*, if the above equation is applied to a gas-phase species involved in any heterogeneous surface reactions, then $\gamma_q = A_s$ is the specific catalyst area). The units of each of the aforementioned terms depends on what phases are being considered. The concentration of species k is $[X_k]$.

The net production rates are in general given by

$$\dot{s}_k = \sum_i \nu_{ki} q_i, \qquad (11)$$

where q_i is the rate of reaction i and ν_{ki} is the net stoichiometric coefficient of species k in reaction i (taken to be positive for products and negative for reactants). The reaction rates are computed from mass-action kinetics,[59] with temperature-dependent rate coefficients in Arrhenius form $k_i = A_i T^{n_i} \exp(-E_i/RT)$.[48] To compute the net production

rates, a reaction mechanism is needed. For example, the reactions of methane on nickel-based catalysts have been extensively studied in the literature, resulting in a reaction mechanism (see Table 8) consisting of 42 irreversible reactions among 6 gas-phase and 12 adsorbed species.[40,41] The multistep heterogeneous chemistry describing the reforming of methane on nickel can be used to calculate $\dot{s}_{\text{gas},k}^{\sim}$ for each gas species k. This mechanism has been adopted in whole or in part in many SOFC models.[42–44,48,49,57] The same mechanism is used to calculate $\dot{s}_{\text{surf},k}$ for each surface species. Likewise, a mechanism describing homogeneous gas-phase thermochemistry can be included to compute $\dot{s}_{\text{gas},k}$. Important thermochemical reactions (*e.g.*, reforming, water-gas shift, POx) are discussed in later sections of this paper.

The species molar fluxes $\mathbf{J}_k$ are evaluated with a transport model[60] (*e.g.*, Fick's laws of diffusion, dusty-gas formulations,[61] Stefan-Maxwell diffusion). Species transport in fuel cells has also been modeled using lattice-Boltzmann models[62–64] and Monte-Carlo-type simulations to predict species diffusivities.[19] Fuel cell models must accurately represent the major physical processes that affect transport in porous media, including molecular diffusion, Knudsen diffusion, surface diffusion, and viscous Darcy flow.

3.3.1.1 Gas transport. The most comprehensive transport model is arguably the dusty-gas model (DGM),[61] which is a multicomponent transport model derived from kinetic theory. It is applicable over a full range of Knudsen numbers, from values much larger than one (molecule-wall collisions dominate, and Knudsen diffusion is the controlling mechanism), to values much less than one (molecule-molecule collisions dominate, and bulk diffusion is controlling).[48] The DGM can be written as an implicit relationship among the molar concentrations $[X_k]$ (mol/m^3/s), molar fluxes $\mathbf{J}_k$ (mol/m^2/s), concentration gradient, and pressure gradient as

$$\sum_{\ell\neq k}\frac{[X_\ell]\mathbf{J}_k-[X_k]\mathbf{J}_\ell}{[X_T]D^{\text{e}}_{k\ell}}+\frac{\mathbf{J}_k}{D^{\text{e}}_{k,\text{Kn}}}=-\nabla[X_k]-\frac{[X_k]}{D^{\text{e}}_{k,\text{Kn}}}\frac{B}{\mu}\nabla p, \quad (12)$$

for $k=1,2,...,K_g$. Here, $[X_T]=p/RT$ is the total molar concentration, B is the permeability of the porous electrode, μ the mixture viscosity, and $D^{\text{e}}_{k\ell}$ and $D^{\text{e}}_{k,\text{Kn}}$ the effective ordinary and Knudsen diffusion coefficients, respectively (m^2/s for both). Because Knudsen diffusion is governed by molecule-wall collisions, it is highly dependent on the porous electrode microstructure, including porosity ϕ, tortuosity τ, and average pore radius r_p. The effective diffusivities can be evaluated as

$$D^{\text{e}}_{k\ell}=\frac{\phi}{\tau}D_{k\ell}, \qquad D^{\text{e}}_{k,\text{Kn}}=\frac{2}{3}r_p\frac{\phi}{\tau}\sqrt{\frac{8RT}{\pi W_k}}, \quad (13)$$

where W_k is the molecular weight of species k. The ordinary multicomponent binary diffusion coefficients $D_{k\ell}$ and mixture viscosity μ are determined from kinetic theory.[59] Alternatively, software packages such as Cantera[51] can be used to easily compute these.

3.3.1.2 Surface transport. In one dimension, without loss of generality, the molar fluxes (mol/m/s) are related to the diffusion coefficients D_k (m^2/s) as

$$J_k=-D_k\frac{\partial[X_k]}{\partial x}, \quad k=1,2,...,K_s \quad (14)$$

The surface concentrations $[X_k]$ (mol/m^2) are related to the coverages θ_k by the available site density as $[X_k]=\Gamma\theta_k$. The number of surface adsorbates is K_s. These equations can be applied to the metal and electrolyte surfaces, but the allowable surface species, diffusion coefficients, and reaction mechanisms are different for each surface. As it relates to the multistep mechanism in Table 3, the flux, diffusion coefficient, and net production rate of each adsorbate on nickel can be calculated based on reactions 1–5; likewise for surface species on YSZ using reactions 6–9.

The solution to Eq. 10 and its coupling to the appropriate relation for $\mathbf{J}_k$ depends upon boundary conditions, and this is where the charge-transfer reactions enter. The reaction-diffusion equation is a parabolic partial differential equation requiring two boundary conditions on the species concentrations $[X_k]$. Typically, depending on model geometry, one of these can be a zero-flux condition at a symmetry plane so that $\partial[X_k]/\partial x=0$ at the x-location of the symmetry plane (*e.g.*, patterned anode geometries). For porous electrodes, the concentration itself is specified at the channel/electrode interface. The other boundary condition applies at the TPB and relates the flux to the production (or consumption) of species due to charge-transfer reactions at the TPB. For the metal (Ni) surface,

$$D_k\frac{\partial[X_k]}{\partial x}\bigg|_{\text{TPB}}=\dot{c}_k, \quad k=1,2,...,K_{s,\text{Ni}}. \quad (15)$$

The term $\dot{c}_k$ is the net production rate of species k due to charge-transfer chemistry at the TPB. It is nonzero only for surface species that participate directly in the charge-transfer reactions. Just as the species production rates $\dot{s}_k$ due to nonfaradaic chemistry act as sources or sinks for a given phase, the production rates from charge-transfer chemistry act as sources or sinks at the TPB. As with the metal surface, the adsorbates on the electrolyte (YSZ) are subject to an equal and opposite condition

$$D_k\frac{\partial[X_k]}{\partial x}\bigg|_{\text{TPB}}=-\dot{c}_k, \quad k=1,2,...,K_{s,\text{YSZ}}. \quad (16)$$

In Eqs. 15 and 16, $K_{s,\text{Ni}}$ and $K_{s,\text{YSZ}}$ refer to the number of species on the nickel and YSZ surfaces, respectively. Because the TPB is defined as the three-phase boundary between gas,

metal, and oxide phases, a similar equation can be written for gas species involved in charge-transfer chemistry.

Unlike the surface production rates, the rates of reaction and production rates of species from electrochemical reactions are dependent on the electric-potential difference across the double layer at the TPB interface. Species production rates at the TPB are calculated from

$$\dot{c}_k = \sum_i \nu_{ki} q_i \tag{17}$$

where ν_{ki} are the stoichiometric coefficients for species k in reaction i and q_i is the rate of reaction i. Of primary interest is the production rate of electrons $\dot{c}_\mathrm{e} = \sum_i \nu_{\mathrm{e}i} q_i$, where $\nu_{\mathrm{e}i}$ is positive for reactions written in the anodic direction, and negative for those written in the cathodic direction.

For a generic elementary charge-transfer reaction written in the anodic direction (*i.e.*, producing electrons)

$$\mathrm{A}^{z_\mathrm{A}} + \mathrm{B}^{z_\mathrm{B}} \rightleftharpoons \mathrm{C}^{z_\mathrm{C}} + \mathrm{D}^{z_\mathrm{D}} + \mathrm{e}^- \tag{18}$$

where k^{z_k} is a generic representation for a species k (A, B, C, or D) having charge z_k (positive, neutral, or negative). Along with element balance, it is necessary that the reaction be charge balanced, which requires $z_\mathrm{A} + z_\mathrm{B} = z_\mathrm{C} + z_\mathrm{D} - 1$.

The net rate of progress is the difference between the anodic and cathodic rates

$$q = q_a - q_c \tag{19}$$

As with all reaction rates, these are a function of temperature, but they also depend on the electric-potential difference $E_a = \Phi_a - \Phi_{e,a}$ across the double layer. Admittedly, there can be much confusion surrounding the various defined potential differences within each anode and across the cell itself. Here we use E_a to represent the potential difference across the anode/electrolyte interface. Similarly, the potential difference across the cathode/electrolyte interface is E_c. The electric potential difference between the anode and electrolyte E_a is written in terms of the anode potential Φ_a and the potential within the electrolyte $\Phi_{e,a}$ just outside the double-layer region at the anode/electrolyte interface. As introduced in the previous subsection, the activation overpotential at the anode $\eta_{\mathrm{act},a} = E_a - E_a^\mathrm{eq}$ is defined to be the difference between E_a and E_a^eq, the latter of which is the equilibrium potential difference across the double layer. The ohmic overpotential $\eta_\mathrm{ohm} = \Phi_{e,a} - \Phi_{e,c}$ (defined in Eq. A-10), is the potential difference across the electrolyte, and $E_\mathrm{cell} = \Phi_c - \Phi_a = E_\mathrm{rev} - \eta_{\mathrm{act},a} - \eta_\mathrm{ohm} - \eta_{\mathrm{act},c}$, where $E_\mathrm{rev} = E_c^\mathrm{eq} - E_a^\mathrm{eq}$ at the TPB.

The anodic and cathodic rates of reaction can be written as

$$q_a = k_a(T) a_\mathrm{A} a_\mathrm{B} \exp\left(\frac{\beta_a F E_a}{RT}\right) \tag{20}$$

and

$$q_c = k_c(T) a_\mathrm{C} a_\mathrm{D} \exp\left(-\frac{\beta_c F E_a}{RT}\right) \tag{21}$$

The temperature-dependent rate constants k_a and k_c can typically be written in Arrhenius form, and the application of this approach requires these values for all reactions, akin to combustion. The species activities are a_k. The anodic and cathodic symmetry factors β_a and β_c determine the relative contributions of the anodic and cathodic currents to the net current. These factors are sometimes called the charge-transfer coefficients, and for elementary reactions, take on values $0 < \beta < 1$, and are constrained by $\beta_a + \beta_c = 1$. In global reactions, symmetry factors are generally called α not β, and there are no specific constraints on the values of α.[43] The rates of all charge-transfer reactions are evaluated to produce the faradaic current at the TPB

$$i_\mathrm{TPB} = F \sum_i (q_{i,a} - q_{i,c}) \tag{22}$$

The faradaic current is related to the measurable current density through a parameter that characterizes the total TPB length of the electrode.

For a complete description of a computational model that couples elementary chemistry, electrochemistry, and surface transport in the vicinity of the TPB, the reader is referred to Goodwin *et al.*[42,43] or Bessler and co-workers.[45,46]

Computing the production rates from faradaic and non-faradaic reactions requires the kinetic parameters for every reaction. In almost all cases, the charge-transfer kinetics are not known, and are instead used as fitting parameters to match model predictions with actual measured cell performance. For models in which the anode potential E_a, species activities a_k, and current density i_TPB are all computed self-consistently, the Butler-Volmer form (discussed next) for representing charge transfer offers no substantial advantages compared to the elementary mass-action form. More importantly, representing reactions in mass-action form does not suffer from restrictions that are inherent in the Butler-Volmer form. Only if the charge transfer is indeed rate limiting, such that the activities are established by much faster processes (*e.g.*, adsorption/desorption), can the Butler-Volmer equation be used.

3.3.2 Butler-Volmer kinetics. The assumption of a single charge-transfer reaction, either through a global representation or reduction of a detailed mechanism controlled by a rate-limiting step, facilitates the ability to relate the current density and activation overpotential through the Butler-Volmer equation,[56]

$$i = i_0 \left[\exp\left(\alpha_a \frac{n_\mathrm{e}^\mathrm{BV} F \eta_{\mathrm{act},i}}{RT}\right) - \exp\left(-\alpha_c \frac{n_\mathrm{e}^\mathrm{BV} F \eta_{\mathrm{act},i}}{RT}\right)\right]. \tag{23}$$

This equation includes the net anodic and cathodic currents due to a single electrochemical reaction transferring n_e^BV elec-

trons. Note that we adopt a notation in which n_e^{BV} is the number of electrons transferred in the rate-limiting step that the Butler-Volmer equation represents, while n_e (used in Eq. 1, for example) is the number of electrons transferred in the anode half-cell oxidation reaction (*e.g.*, $n_e = 2$ for H_2 and CO). Of course, if the electrochemistry is only represented with a global charge-transfer reaction, $n_e^{BV} = n_e$. For an electrode i (*i.e.*, a for "anode," c for "cathode"), the activation overpotential $\eta_{act,i} = E_i - E_i^{eq}$ is the potential difference above the equilibrium electric potential between the electrode and electrolyte (this is discussed in more detail later). For global reactions, the are no constraints on the values of the symmetry factors α_a and α_c. For elementary reactions transferring a single electron (*i.e.*, $n_e^{BV} = 1$), it is common to write α as β. The anodic and cathodic symmetry factors β_a and β_c determine the relative contributions of the anodic and cathodic currents to the net current. These factors are sometimes called the charge-transfer coefficients, generally take on values between zero and one, and are constrained by $\beta_a + \beta_c = 1$. Because there is an activation overpotential for the anode and cathode, there is a different set of charge-transfer coefficients for the two electrodes. The exchange current density i_0 is the current density at the equilibrium potential difference E_i^{eq}. A high exchange current density means the charge-transfer reaction proceeds rapidly when the potential is varied from its equilibrium value.

At equilibrium and only at equilibrium, the two partial current densities at the electrode are equal in magnitude and opposite in direction. When $\eta_{act,i}$ is negative, there will be a net cathodic electron flow (transfer of negative charge) from the electrode to the electrolyte. Conversely, when $\eta_{act,i}$ is positive, there will be a net anodic electron flow from the electrolyte to the electrode. In general, the anodic and cathodic current contributions are

$$i_a = i_0 \exp\left(\alpha_a \frac{n_e^{BV} F \eta_{act,i}^{eq}}{RT}\right),$$

and

$$i_c = -i_0 \exp\left(-\alpha_c \frac{n_e^{BV} F \eta_{act,i}^{eq}}{RT}\right),$$

with net current density $i = i_a + i_c$. At equilibrium, $i_a^{eq} = -i_c^{eq} = i_0$ because $E_i = E_i^{eq}$, giving $\eta_{act,i}^{eq} = 0$.

Applying the Butler-Volmer equation for an electrochemical reaction represents a semi-empirical approach, in which parameters such as the exchange current density i_0 must be measured from experiments. The exchange current density i_0 is a measure of the electrocatalytic activity of the electrode/electrolyte interface for a given electrochemical reaction. It depends on charge-transfer kinetics (which are generally unknown and not well understood), the concentrations of reactants and products at the TPB, temperature, pressure, and microstructure of the electrode (also unknown, though recent efforts[19,44,65–70] have shed some light on this). Determining the dependence of the exchange current density on reactant and product concentrations from a detailed electrochemical reaction mechanism will reveal the apparent reaction order, which might not always be evident based on a global oxidation reaction.[48,49]

The Butler-Volmer equation is the central equation of phenomenological electrode kinetics, valid under conditions where there is a plentiful supply of reactant by easy transport to and from the electrodes in the electrolyte.[71] This ensures the rate of reaction is indeed controlled by the electric charge transfer at the TPB, and not by transport of ions to the electrode or away from it. One interesting limiting case of the Butler-Volmer equation is discussed below, specifically in the context of an elementary charge-transfer reaction (*i.e.*, a reaction involving only one exchanged electron).

3.3.2.1 The high overpotential case. When $\eta_{act,i} \gg RT/\beta F$ (here, β is used as a generic representation of β_a or β_c),† one of the exponential terms in the Butler-Volmer equation will be negligible:

$$i = i_0 \exp\left(\beta_a \frac{F\eta_{act,i}}{RT}\right) \quad \text{for} \quad \frac{\beta_a F \eta_{act,i}}{RT} \gg 1, \qquad (24)$$

or

$$i = -i_0 \exp\left(-\beta_c \frac{F\eta_{act,i}}{RT}\right) \quad \text{for} \quad -\frac{\beta_c F \eta_{act,i}}{RT} \gg 1. \qquad (25)$$

The anodic and cathodic branches of the current density are easily manipulated to produce

$$\eta_{act,i} = \begin{cases} \frac{RT}{\beta_a F} \ln\left(\frac{i}{i_0}\right) & : \quad \frac{\beta_a F \eta_{act,i}}{RT} \gg 1 \\ -\frac{RT}{\beta_c F} \ln\left(-\frac{i}{i_0}\right) & : -\frac{\beta_c F \eta_{act,i}}{RT} \gg 1 \end{cases} \qquad (26)$$

These two relationships represent Tafel-type equations[56,71] (*i.e.*, an equation such that $\eta_{act,i} \propto \ln i$, which produces straight lines on a semi-logarithmic plot). This sort of plot is useful for determining the anodic and cathodic charge-transfer coefficients β_a and β_c from the slope of the line. That is, it is relatively simple to set up an experiment to vary the activation overpotential and measure the current with all other conditions held fixed. Since the other constants in the lead term are known, the charge-transfer coefficients can be found for both positive bias (anodic branch) and negative bias (cathodic branch) overpotentials.

Absent this information, it is quite common and reasonable to take $\beta_a = \beta_c = 1/2$ for elementary charge-transfer reactions,[56,71] which corresponds to a symmetrical energy barrier at the charge-transfer interface. The remaining unknown

† Assuming a typical value of $\beta = 1/2$, $RT/\beta F = 0.15$ V at 600°C, and 0.22 V at 1000°C. SOFCs are normally operated in the range 600–1000°C.

in many of these equations is the exchange current density i_0. This parameter represents a kinetic equilibrium of the exchange of charge across the TPB. It is a significant and useful arbiter of the dynamic nature of the electrode reaction that determines the rate of electrode reactions for any potential difference E_i across the electrode.[71]

4 Electrochemistry in SOFC anodes

The reaction mechanism describing chemistry and electrochemistry within a SOFC anode is extremely complex. The elementary reaction steps may include homogeneous gas-phase chemistry, heterogeneous surface reactions of ad/desorbing species, homogeneous surface dissociation and reactions between adsorbed species, and heterogeneous charge-transfer reactions. To complicate things further, reaction kinetics are governed by a host of phenomena spanning many length scales (*e.g.*, continuum mass transport, heat transfer, percolation theory, molecular and Knudsen diffusion, surface diffusion, catalysis, thermodynamics). Understanding of the reaction mechanism and chemical and electrochemical kinetics are paramount to optimize the anode and operating conditions.

The primary focus for studying the anode reaction mechanism is to identify the rate-limiting step (or steps, which likely depend on temperature, current density, and/or other variables). The rate-limiting or rate-determining step (RDS) controls the rate at which all other elementary steps can proceed—just as its name implies—and therefore, the ability of the cell to produce current. Its identification is necessary for electrode performance improvement by minimizing its limiting effects. Knowledge of the RDS informs electrode design and optimization (*e.g.*, by using different materials, changing the operating conditions, or altering the microstructure). To pinpoint the RDS, detailed knowledge of chemical and electrochemical reaction rates is required, as well as an understanding of the surface species and their conversion paths, and the combinations of elementary reaction parameters. In addition, the rate-limiting step depends on the materials and operating conditions, such as temperature, fuel composition, polarization voltage, and more. Because of the complexity and interrelation of so many variables, various rate-limiting steps have been proposed in the literature under different operating conditions,[72,73] including reactivities and charge transfer,[74–76] surface diffusion,[75,77] adsorption,[75] sintering and/or impurities, rates of hydrogen desorption, catalytic effects of water, the role of the YSZ support, and others.

In this section, recent studies on SOFC anode reaction mechanisms are summarized, with primary focus on the elementary electrochemical oxidation reaction mechanisms of H_2, CO, CH_4, and solid carbon; these constitute the main species in practical fuels such as hydrocarbons, coal syngas, and biogas. Furthermore, particular attention is given to carbon deposition and issues related to sulfur poisoning.

4.1 H_2 electrochemical oxidation

As discussed in the foregoing section, the Ni-YSZ cermet anode is the most widely studied anode for SOFC applications. This cermet structure effectively increases adhesion between anode and electrolyte, and achieves large electrochemical active area by extending the three-phase boundaries (TPBs) from the anode/electrolyte interface, up into the porous anode. Due to the complex microstructure of typical Ni-YSZ cermet anodes, the three phases (*i.e.*, metal, oxide, and pore/gas) are composed of various interconnected networks.[19,68,70] These networks form a highly convoluted structure marked by TPB regions that cannot easily be probed by experiment. Since the TPB is where current-producing reactions occur, exposing this area to study is necessary to make clear the reaction path in the anode. Therefore, researchers carry out studies on anode reaction mechanisms using electrodes that are designed to have geometrically simple TPBs, *e.g.*, so-called point or pattern anodes.[77–79] However, a point or pattern electrode in a flowing system may not necessarily be affected by the same phenomena as a porous cermet, because the inherent and deliberate open design of the MEA and TPB facilitates gas transport—gas-phase reactants are always readily available, and products are whisked away from reactive sites (*i.e.*, species residence times near the TPB are greatly reduced compared to a true porous cermet). For example, a point or pattern anode would not be expected to exhibit significant readsorption of the water vapor created by reaction because that water vapor is removed by the gas stream (whereas in a porous cermet, the water vapor must diffuse through the pores).[73]

There are three different main reaction mechanisms that have been proposed: (*i*) hydrogen spillover, (*ii*) oxygen spillover, and (*iii*) interstitial hydrogen charge transfer (see Ref. 80 for additional discussion and references on each of these). The term spillover is used to describe the process by which a molecule adsorbs or reacts on one of the phases (Ni or YSZ) before diffusing over onto the second phase, where it is free to react with other adsorbed species on that phase.

4.1.1 Hydrogen spillover. A hydrogen-spillover mechanism was first reported by Mogensen and Lindegaard[81] Gas-phase molecular hydrogen $H_2(g)$ is adsorbed and subsequently dissociates on the Ni surface (Ni). The adsorbed hydrogen atoms H(Ni) are then transported as protons H^+(Ni)—which requires the release of an electron to the anode e^-(Ni)—to the TPB region. Oxygen ions on the electrolyte O^{2-}(YSZ) react with the protons and form adsorbed hydroxyl ions OH^-(YSZ). Two hydroxyl ions then react on the YSZ surface to form water and O^{2-}(YSZ). The hypothesized elementary reactions for

this mechanism are[81]

1. Adsorption/desorption on the Ni surface
   $H_2(g) + 2(\mathrm{Ni}) \rightleftharpoons 2\mathrm{H(Ni)}$
2. Ionization of adsorbed atomic hydrogen on the Ni surface
   $2 \times \left[\mathrm{H(Ni)} \rightleftharpoons \mathrm{H^+(Ni)} + \mathrm{e^-(Ni)} \right]$
3. Diffusion of $\mathrm{H^+(Ni)}$ to the TPB
4. Charge transfer at the TPB region
   $2 \times \left[\mathrm{H^+(Ni)} + \mathrm{O^{2-}(YSZ)} \rightleftharpoons \mathrm{(Ni)} + \mathrm{OH^-(YSZ)} \right]$
5. Formation of water by reactions on the YSZ surface
   $2\mathrm{OH^-(YSZ)} \rightleftharpoons \mathrm{(YSZ)} + \mathrm{H_2O}(g) + \mathrm{O^{2-}(YSZ)}$

This mechanism was proposed after interpretation of measured electrochemical impedance spectra (EIS) for oxidation of H_2 on a Ni-YSZ cermet electrode. The EIS data show two separate circles dependent on H_2 partial pressure p_{H_2}, as well as the ratio of p_{H_2}/p_{H_2O}. It was suggested that the high-frequency semicircle (low p_{H_2} values, 0.05–0.3 atm) is related to proton transfer across the TPB (step 4), and is limited by the TPB length—here, the reaction rate has a first-order dependence on H_2 partial pressure (*i.e.*, the rate scales with p_{H_2}). The second semicircle at lower frequencies (high p_{H_2} values, 0.5–0.97 atm) is attributed to a reaction resistance caused by the formation of water (step 5), which is assumed to occur on the YSZ surface. The adsorption/desorption of hydrogen on the Ni surface (step 1) could also be rate-determining in this limit. In the range of high H_2 partial pressures, a reaction order of two was found (*i.e.*, the rate scales with $p_{H_2}^2$), which is not consistent with the suggested mechanism.

De Boer[76] later proposed a slightly different reaction process to enable discussion of his own data from experiments on porous nickel electrodes on YSZ. The inclusion of step 3, involving interstitial protons as a mediator in the reaction scheme, was first proposed by Mogensen and co-workers.[76,82] De Boer notes, however, that there is no direct evidence from experiment for the involvement of interstitial protons in the reaction kinetics. De Boer's mechanism still involves the hydroxyl intermediate on the YSZ surface, but without the existence of chemisorbed protons on the nickel surface (only neutral hydrogen atoms):[76]

1. Adsorption/desorption on the Ni surface
   $H_2(g) + 2(\mathrm{Ni}) \rightleftharpoons 2\mathrm{H(Ni)}$
2. Charge-transfer bulk reaction at the TPB region
   $\mathrm{H(Ni)} + \mathrm{O_O^\times(Ni)} \rightleftharpoons \mathrm{(Ni)} + \mathrm{OH_O^\cdot(Ni)} + \mathrm{e^-(Ni)}$
3. Transfer of hydroxyl ions between surface and bulk YSZ
   $\mathrm{OH_O^\cdot(Ni)} + \mathrm{(Ni)} \rightleftharpoons \mathrm{OH^-(Ni)} + \mathrm{V_O^{\cdot\cdot}(Ni)}$
4. Charge-transfer surface reaction at the TPB region
   $\mathrm{H(Ni)} + \mathrm{OH^-(YSZ)} \rightleftharpoons \mathrm{(Ni)} + \mathrm{H_2O(YSZ)} + \mathrm{e^-(Ni)}$
5. Adsorption/desorption on the YSZ surface
   $\mathrm{H_2O(YSZ)} \rightleftharpoons \mathrm{(Ni)} + \mathrm{H_2O}(g)$

An important distinction between De Boer's mechanism and that of Mogensen *et al.*[81,82] is that surface-adsorbed hydrogen on the anode reacts first with an oxygen ion (in the electrolyte sublattice) to produce a protonated ion (step 2) at the TPB, then the protonated ion moves from the oxygen sublattice to the electrolyte surface (step 3) where it reacts with a second hydrogen atom (step 4). In the mechanism postulated by Mogensen *et al.*, the hydrogen atoms (albeit, protons) only react with oxygen ions and the resulting hydroxyl ions then react with each other.

Many researchers have cited De Boer's mechanism. Goodwin *et al.*[42,43] developed a complete kinetic and thermodynamic database for H_2 electrochemical oxidation on nickel according to De Boer's mechanism. Zhu *et al.*[48] detailed a computational framework for modeling chemically reacting flow in anode-supported SOFCs using a modified version of the De Boer reactions (all charge-transfer reactions involve surface species only, and oxygen ions are transferred between the surface and bulk YSZ instead of hydroxyl ions). The novel approach by Zhu *et al.* assumed that the rate-limiting oxidation step is H(Ni) reacting with $\mathrm{OH^-(YSZ)}$ at the TPB, forming adsorbed $\mathrm{H_2O(YSZ)}$ as described by step 4 in De Boer's scheme. The other reactions are assumed to be equilibrated. Under this assumption, the Butler-Volmer form of the relationship between current density and activation overpotential can be formulated as[48]

$$i = i_0 \left[\exp\left(\frac{(\beta_{4,a}+1)F\eta_{\mathrm{act},a}}{RT} \right) - \exp\left(\frac{\beta_{4,c}F\eta_{\mathrm{act},a}}{RT} \right) \right] \quad (27)$$

where $\eta_{\mathrm{act},a} = E_a - E_a^{\mathrm{eq}}$ is the anode activation overpotential and the exchange current density is given as

$$i_0 = i^*_{H_2} \frac{(p_{H_2}/p^*_{H_2})^{1/4} p^{3/4}_{H_2O}}{1 + (p_{H_2}/p^*_{H_2})^{1/2}} \quad (28)$$

The anodic and cathodic symmetry factors are constrained by $\beta_{4,a} + \beta_{4,c} = 1$, and each is taken to be 1/2, typical for

an elementary reaction.[56] The exchange current density reveals the apparent reaction order of the charge-transfer process, and it is evident that the exchange current density has a positive dependence on p_{H_2O} (*i.e.*, it is enhanced by the presence of water). Other than gas-phase partial pressures, the exchange current density depends on the parameter $i^*_{H_2}$, which itself is comprised of constants that are generally not known (*e.g.*, reaction-rate constants, reaction equilibrium constants, specific TPB length), so it is used as an empirical parameter that can be adjusted to fit measured fuel-cell performance. The parameter $p^*_{H_2}$ is determined from the balance between adsorption and desorption of hydrogen on the Ni surface. It is related to the equilibrium constant of reaction 1, $p^*_{H_2} = 1/K_1$, and more information about its calculation can be found in Ref. 48.

Lee *et al.*[49] further analyzed the possibility that a different intermediate step in the hydrogen electrochemical oxidation model is rate limiting at high current densities, and proposed a rate-limiting switchover model to explain the limiting current density. The model improves the prediction of the limiting current density and provides better agreement with experimental results. The reaction steps used by Lee *et al.*[49] and Zhu *et al.*[48] are detailed below:

1. Adsorption/desorption on the Ni surface
   $H_2(g) + 2(\text{Ni}) \rightleftharpoons 2\text{H(Ni)}$
2. Charge-transfer reactions at the TPB region
   $\text{H(Ni)} + \text{O}^{2-}(\text{YSZ}) \rightleftharpoons (\text{Ni}) + \text{OH}^-(\text{YSZ}) + \text{e}^-(\text{Ni})$
   $\text{H(Ni)} + \text{OH}^-(\text{YSZ}) \rightleftharpoons (\text{Ni}) + \text{H}_2\text{O(YSZ)} + \text{e}^-(\text{Ni})$
3. Adsorption/desorption on the YSZ surface
   $\text{H}_2\text{O(YSZ)} \rightleftharpoons (\text{YSZ}) + \text{H}_2\text{O}(g)$
4. Transfer of oxygen ions between surface and bulk YSZ
   $\text{O}^{\times}_{\text{O}}(\text{YSZ}) + (\text{YSZ}) \rightleftharpoons \text{O}^{2-}(\text{YSZ}) + \text{V}^{\cdot\cdot}_{\text{O}}(\text{YSZ})$

As with the mechanisms before it, this scheme assumes $\text{OH}^-(\text{YSZ})$ is the reaction intermediate in the two-electron charge-transfer process. The distinguishing feature of this mechanism compared to that of De Boer is that the first charge-transfer reaction is assumed to be a surface process (not interstitial), so that only oxygen ions move between the surface and bulk of the electrolyte (step 4).

Fig. 4 compares results from the rate-limiting switchover model of Lee *et al.*[49] to experimental data from Jiang and Virkar.[33] The model is formulated around a Butler-Volmer description of hydrogen charge transfer, in which the rate-limiting reaction changes from H(Ni) reacting with $\text{OH}^-(\text{YSZ})$ at the TPB (*i.e.*, the second charge-transfer reaction in the scheme above), to adsorption/desorption of H_2 on the Ni surface at current densities close to the limiting value. The model incorporates porous media transport in the electrodes, heterogeneous surface chemistry in the anode, and charge transfer at the TPB. Simulation results compare very favorably with measured performance over a wide range of compositions, with the exception of very high concentrations of H_2.

In an effort to better explain observed catalytic effects of water in the anode, Jiang and Badwal[75,83] introduced yet another mechanism for H spillover to YSZ—note that all previous mechanisms also involve hydrogen spillover to the electrolyte, as opposed to oxygen spillover to the anode—that accounts for competitive adsorption of oxygen on the anode from water dissociation. In the absence of water, however, the mechanism greatly differs from those above in that the hydrogen atom is allowed to sit on the YSZ surface after spilling over the TPB (step 3), where it reacts with an oxygen in the sublattice to form water in a two-electron process (step 4).

1. Hydrogen dissociative adsorption on the Ni surface
   a. *In dry hydrogen:*
      $H_2(g) + 2(\text{Ni}) \rightleftharpoons 2\text{H(Ni)}$
   b. *In wet hydrogen:*
      $\text{H}_2\text{O}(g) + (\text{Ni}) \rightleftharpoons (\text{Ni–O}) + \text{H}_2(g)$
      $H_2(g) + 2(\text{Ni}) \rightleftharpoons 2\text{H(Ni)}$
      $\text{H(Ni)} + (\text{Ni–O}) \rightarrow (\text{Ni}) + \text{H(Ni–O)}$

2a. Diffusion of H(Ni) to the TPB

2b. Diffusion of H(Ni–O) to the TPB

3. Hydrogen spillover at or near the TPB region
   H(Ni) and/or $\text{H(Ni–O)} \rightleftharpoons \text{H(YSZ)}$
4. Charge-transfer and H_2O formation on YSZ at the TPB
   $\text{O}^{\times}_{\text{O}}(\text{YSZ}) + 2\text{H(YSZ)} \rightleftharpoons \text{H}_2\text{O}(g) + (\text{YSZ}) + \text{V}^{\cdot\cdot}_{\text{O}}(\text{YSZ}) + 2\text{e}^-(\text{YSZ})$
   $\text{e}^-(\text{YSZ}) \rightleftharpoons \text{e}^-(\text{Ni})$

In the notation above, (Ni–O) is an active metal site adjacent to an O(Ni) or sub-NiO. Jiang and Badwal discounted the existence of adsorbed H_2O, hydroxide, or hydroxyl species on nickel because these have not been detected at elevated temperatures.[83] This follows the precedent of the previous mechanisms in which these species only exist on the electrolyte surface. Moreover, the authors comment that hydrogen dissociative adsorption (step 1a) is very fast at SOFC operating temperatures, but coverage of H(Ni) is low, indicating that surface diffusion on the metal surface (step 2a) is rate limiting in dry hydrogen.[83] In a real cermet electrode under operation with dry hydrogen, however, the oxidation process will produce H_2O, whose presence will impact the overall process. Although the site density on the nickel surface for hydrogen dissociation is reduced in wet hydrogen due to competitive adsorption of oxygen from water dissociation (the first reaction under step 1b), the overall reaction rate is increased due to the

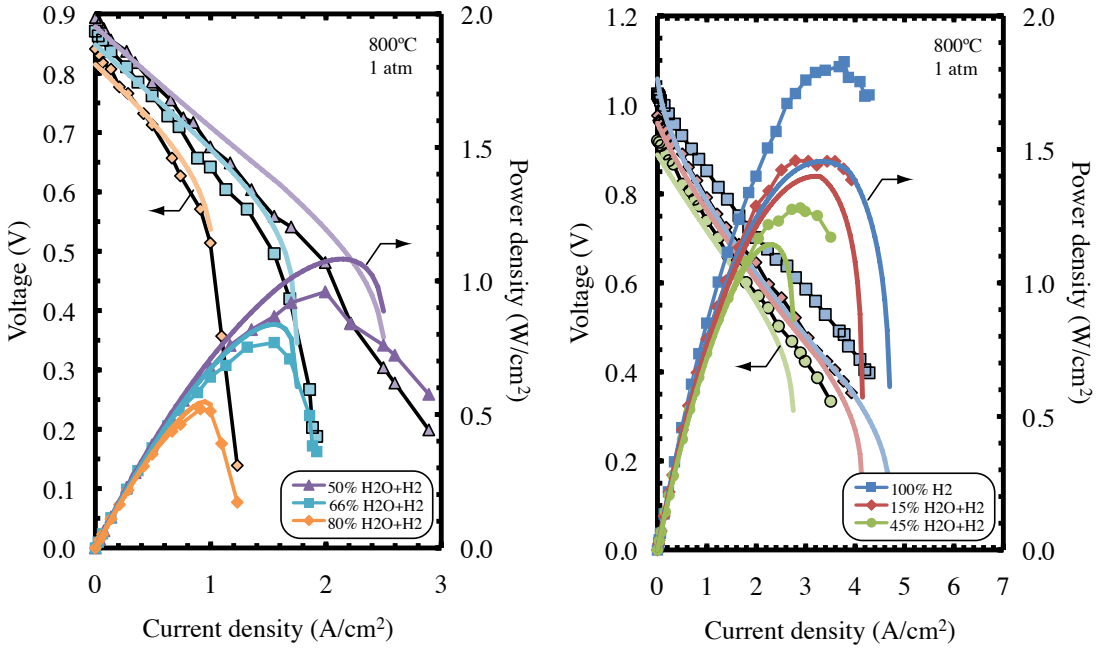

Fig. 4 Comparison of measured (symbols) and computed (solid lines) MEA performance operating on different H_2-H_2O mixtures at 800°C and 1 atm. In each panel, the symbols are experimental measurements of button-cell performance by Jiang and Virkar[33] using a Ni-YSZ porous anode. Symbols are connected for clarity. The solid lines are computed performance of the same button cell using a rate-limiting switchover model as described in Lee *et al.*[49] The left panel is for H_2 concentrations less than or equal to 50%, and the right panel for H_2 concentrations greater than 50%.

much faster surface diffusion via a spillover mechanism (step 3) that further frees up metal sites for dissociative adsorption of hydrogen.[83] The transfer of hydrogen species from Ni to YSZ (step 3) and the charge transfer on YSZ (step 4) limit the overall reaction rate in wet hydrogen.[75]

In addition to the work of Jiang and Badwal, Bieberle *et al.*[84] used nickel-patterned-anode experiments and measured EIS to postulate on the reaction mechanism and catalytic effects of water for Ni-YSZ cermets. That group also suggests a H-to-YSZ spillover mechanism, illustrated pictorially in Fig. 5. In a dry fuel gas atmosphere, the YSZ surface is assumed to be primarily covered with oxygen, and the electrochemically active sites are restricted to the vicinity of the TPB. In contrast to this, the YSZ surface is hydroxylated in a wet fuel gas atmosphere. In Fig. 5a, H_2 dissociatively adsorbs onto the Ni surface, and O^{2-} diffuses to the YSZ surface. The adsorbed hydrogen atoms are oxidized to protons H^+ on the Ni surface and the O^{2-} is removed from the electrolyte bulk, which causes an adjacent hydroxyl group on the YSZ to be deprotonated (Fig. 5b). A cascading of protonation and deprotonation of the adsorbed YSZ hydroxyl groups follows (Fig. 5c), eventually causing one of the protons on the Ni surface to jump to a nearby adsorbed hydroxyl ion on YSZ. This cascading effect represents a proton migration from the Ni surface to the location where an O^{2-} was transferred from the YSZ bulk to the YSZ surface. A second H^+ then migrates to this location and reacts with OH^- on YSZ. Water is formed

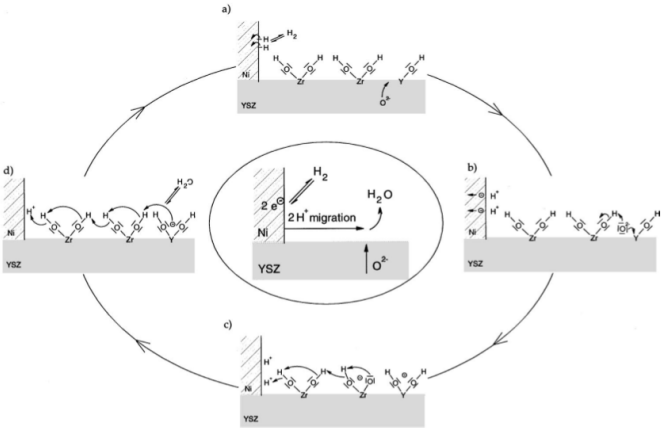

Fig. 5 Model for the catalytic effect of the addition of water in the fuel gas atmosphere on the performance of SOFC anodes. The small arrows indicate the migration of the electrons. For detailed explanations refer to the text. Picture and description from Ref. 84.

and desorbs from the YSZ surface. A summary of the stepwise mechanism described above is shown in the center of Fig. 5. This scheme is similar to a combination of that from Mogensen *et al.* (protonation as a separate step) and the modified De Boer mechanism used by Zhu *et al.* and Lee *et al.*, in which OH^-(YSZ) is first formed on the electrolyte surface by reaction of surface oxygen ions and a proton, then H_2O by reaction with another proton (instead of two hydroxides reacting on the surface). Bieberle has also investigated the catalytic effects of water in a modeling context using an oxygen-spillover mechanism that is discussed in the next section.

In general, the spillover of hydrogen from the Ni to the YSZ surface is characterized by adsorption of molecular hydrogen on the Ni surface, and desorption of water from the YSZ surface. While there is, to the best of our knowledge, no direct experimental evidence of hydrogen spillover, the feasibility of this mechanism is supported by the fast surface transport of both, adsorbed hydrogen on the Ni surface (see Ref. 33 in Bessler *et al.*[80]) and protons on the YSZ surface (see Ref. 34 in Bessler *et al.*[80]).

4.1.2 Oxygen spillover. Oxygen spillover suggests that oxygen ions are transported by surface spillover from the electrolyte (*i.e.*, YSZ) to the nickel at (or very near) the TPB, where they react with adsorbed hydrogen to generate water and electrons. Unlike hydrogen spillover, the adsorption of molecular hydrogen and desorption of water both take place on the Ni surface. Mizusaki *et al.*,[77] who introduced the concept of pattern electrodes to design the morphology and length of the TPB to study reaction kinetics, first published the oxygen-spillover mechanism. They studied hydrogen electrochemical oxidation on nickel-pattern electrodes with different pattern widths and separations. The authors argue that the observed linear relation between the electrode interface conductivity—$\sigma_E = 1/(AR_E)$, where A is the electrode area, and R_E is the resistance due to the electrode reaction obtained from the intercept of the electrode impedance arc with the real axis of the complex impedance plane (σ_E is proportional to the exchange current, which represents the magnitude of the reaction rate and reaction order)—and TPB length suggests that the rate-determining reaction process takes place around the TPB. From their measured EIS and the dependence of σ_E as a function of hydrogen and water gas-phase partial pressures (p_{H_2} and p_{H_2O}), it was concluded that the reaction site for the rate-determining step was the Ni surface close to the TPB.

Bieberle and Gauckler[78,79] compared experimental EIS to simulation results of nickel-patterned anodes exposed to gaseous H_2-H_2O mixtures. In their model, an oxygen-spillover mechanism was assumed and the unknown reaction kinetics were tuned to provide a best fit between model results and measured data. The electrochemical model is illustrated in Fig. 6, and the numbers in the figure correspond to the reaction steps below.[79]

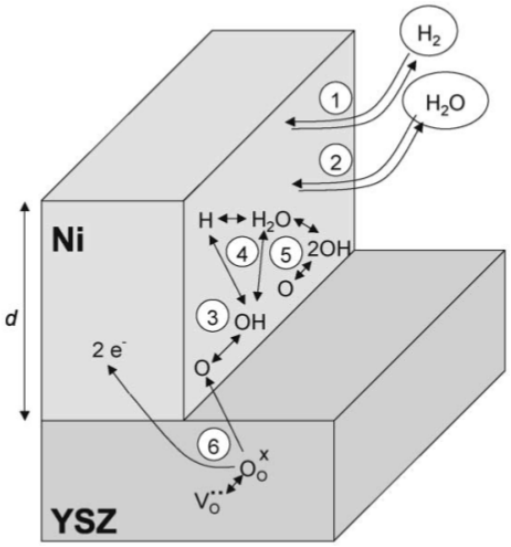

Fig. 6 Electrochemical model for the Ni-H_2-H_2O/YSZ system under SOFC operating conditions. The numbers in the figure correspond to reactions given in the text. Picture and description from Ref. 79.

Adsorption/desorption on the Ni surface:

(4) $H_2(g) + 2(Ni) \rightleftharpoons 2H(Ni)$

(5) $H_2O(g) + (Ni) \rightleftharpoons H_2O(Ni)$

Surface reactions on the Ni surface:

(6) $O(Ni) + H(Ni) \rightleftharpoons (Ni) + OH(Ni)$

(7) $H_2O(Ni) + O(Ni) \rightleftharpoons 2OH(Ni)$

(8) $H_2O(Ni) + (Ni) \rightleftharpoons OH(Ni) + H(Ni)$

Interface reaction (spillover from bulk YSZ to Ni surface):

(9) $O_O^{\times}(YSZ) + (Ni) \rightleftharpoons O(Ni) + V_O^{\cdot\cdot}(YSZ) + 2e^-(Ni)$

The model and simulations carried out by Bieberle and Gauckler were, at the time, unique in detailing the kinetics of an electrochemical model for SOFC anodes. While the validity of the modeling framework was clearly demonstrated, the number of unknowns and *a priori* assumptions limit its applicability for unambiguous interpretation of the kinetics. Differences between experiment and simulation are attributed to shortcomings of the model and the oxygen-spillover mechanism. In particular: (*i*) the YSZ surface was not considered to be electrochemically active; (*ii*) reaction-rate constants are assumed to be independent of surface coverages; and (*iii*) surface diffusion is assumed to be fast and gas-phase diffusion is not included. The authors admit that even in their detailed study, it

is risky to conclude that a specific reaction mechanism dominates.[79]

Because the oxygen spillover process does not involve the fuel species to be oxidized, it can be at the origin of electrochemical oxidation of any fuel.

4.1.3 Interstitial hydrogen charge transfer. At the high operating temperatures of SOFCs (600–1000°C), interstitial hydrogen atoms in bulk Ni and interstitial protons in bulk YSZ are known to be present in relatively high concentrations (around 0.1 mol%), with high enough diffusivities to support the anode half-cell hydrogen oxidation.[80] Charge-transfer at the Ni/YSZ interface (a two-dimensional interface, as opposed to the one-dimensional TPB) can then proceed according to $H_i^{\times}(\mathrm{Ni}) \rightleftharpoons H_i^{\cdot}(\mathrm{YSZ}) + e^{-}(\mathrm{Ni})$, where Kröger-Vink notation has been used (this reaction appears as reaction 5 in Table 2).

Holtappels *et al.*[74] suggest the possible role of interstitial hydrogen and hydroxyl formation at Ni/YSZ interfaces. This is illustrated graphically in Fig. 7(d). Interstitial hydrogen and protons are formed via adsorption and surface/bulk exchange from hydrogen on Ni and water on YSZ, respectively.[80] Because the solubility and diffusivity of H in a metal lattice is relatively high, the Ni/YSZ interface can affect the anodic reaction. The elementary reaction steps include: (1) diffusion of gas-phase reactants to the solid surfaces (*i.e.*, H_2 to Ni and H_2O to YSZ); (2) dissociative adsorption of gas-phase reactants at the solid surfaces (*e.g.*, forming H_{ad}, O_{ad}, OH_{ad}); (3) surface diffusion of adsorbed species or bulk diffusion of H within the anode metal to reaction sites; and (4) charge transfer at the TPB region or across the Ni/YSZ interface to eventually form H_2O, which desorbs from the YSZ surface.

4.1.4 Improved and combined mechanisms. Bessler *et al.*[80] address the general misunderstanding in most SOFC reaction-kinetic studies (including those discussed above) that electrochemical reaction rates depend only on reactant concentrations. To be thermodynamically sound, reaction rates and electrochemical equilibrium depend on reactant *and* product concentrations, because it is a dynamic equilibrium between forward and backward reactions. The authors develop a thermodynamic model of the TPB that describes the coupling of electroactive intermediates with global gas-phase species. The model is used to study the behavior of the reaction pathways discussed above, and results are compared to published experimental data. The five charge-transfer reactions (and associated references mentioned here in which they appear) are summarized in Table 2.[80]

The well-established activating effects of water on the anode kinetics can be explained by Nernst-potential (equilibrium-potential) effects alone, argue Bessler *et al.*, without the need to assume any additional kinetic or catalytic effect. The results indicate that all charge-transfer reactions have a strong and highly nonlinear kinetic depen-

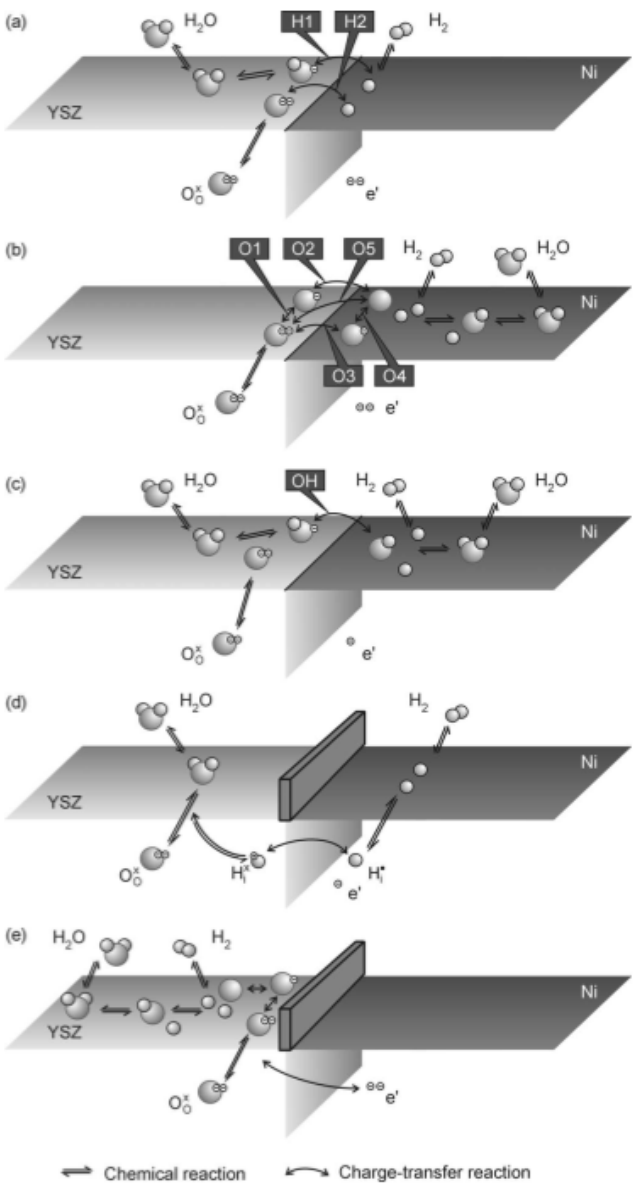

Fig. 7 Elementary kinetic scenarios at a Ni-YSZ TPB. Each charge-transfer reaction is a reversible reaction taking up or releasing charge to the valence band of the Ni electrode. (a) Spillover of hydrogen from the Ni surface onto an oxygen ion or hydroxyl ion on the YSZ surface. (b) Charge-transfer reactions with and without spillover of oxygen ions from the YSZ surface to the Ni surface. (c) Hydroxyl spillover from the YSZ surface to the Ni surface. (d) Charge transfer by an interstitial proton. (e) Charge-transfer and chemical reactions on the electrolyte surface only. The "walls" in panels (d) and (e) indicate potential segregated impurities. Graphic and description from Ref. 85.

Table 2 Elementary charge-transfer reactions analyzed in Ref. 80

No.	Label	Reaction
1	O spillover [a] (Refs. 77–79,85)	$O^{2-}(YSZ) + (Ni) \rightleftharpoons O(Ni) + (YSZ) + 2e^-(Ni)$
2	OH spillover (Ref. 85)	$OH^-(YSZ) + (Ni) \rightleftharpoons OH(Ni) + (YSZ) + e^-(Ni)$
3	H spillover to O [b] (Refs. 48,49,76,81,85)	$H(Ni) + O^{2-}(YSZ) \rightleftharpoons (Ni) + OH^-(YSZ) + e^-(Ni)$
4	H spillover to OH (Refs. 48,49,76,84,85)	$H(Ni) + OH^-(YSZ) \rightleftharpoons (Ni) + H_2O(YSZ) + e^-(Ni)$
5	H interstitial [c] (Refs. 74,80)	$H_i^{\times}(Ni) \rightleftharpoons H_i(YSZ) + e^-(Ni)$

[a] As lattice oxygen $O_O^{\times}(YSZ)$ to (Ni) (Refs. 78,79) or as written.
[b] As $H^+(Ni)$ to $O^{2-}(YSZ)$ (Ref. 81), H(Ni) to $O_O^{\times}(YSZ)$ (Ref. 76), or H(Ni) to $O^{2-}(YSZ)$ (Refs. 48,49).
[c] Refs. 75,83 include H spillover on the surface across the TPB as H(Ni) and/or H(Ni–O) $\rightleftharpoons$ H(YSZ).

dence on gas-phase hydrogen and water partial pressures due to equilibrium-potential effects, and this behavior is distinctly different for the various mechanisms. All mechanisms given in Table 2 show an increase in exchange current density with increasing p_{H_2O}. However, with increasing p_{H_2}, the O and OH spillover reactions show decreasing kinetics, while the H spillover and H interstitial reaction kinetics are increasing. This finding supports a conclusion that the dominating reaction mechanism and kinetics of charge-transfer may change with operating conditions. In addition, although the model is unable to consistently interpret all published experimental results simultaneously, they agree mostly that the rate-limiting step in pattern anodes is charge-transfer, and the observations are most consistent with a surface hydrogen spillover reaction (Table 2, No. 4) as rate-determining.

Recently, Vogler *et al.*[85] presented a quantitative elementary kinetic model of the hydrogen oxidation reaction for Ni-YSZ pattern anodes. Their model describes the coupling of surface reactions and surface diffusion with charge-transfer through spillover reactions. In total, 15 elementary steps are considered (including three surface reactions on YSZ, five surface reactions on Ni, and seven charge-transfer reactions near the TPB), which is the most comprehensive published model for H_2 electrochemical oxidation. Aside from the first four charge-transfer elementary reaction steps in the model of Bessler *et al.* (*i.e.*, Nos. 1–4 from Table 2; No. 5, H interstitial is *not* included), three additional charge-transfer reactions are considered, introducing the surface species $O^-(YSZ)$ and $O^-(Ni)$,

$$O^{2-}(YSZ) \rightleftharpoons O^-(YSZ) + e^-(Ni)$$
$$O^{2-}(YSZ) + (Ni) \rightleftharpoons O^-(Ni) + (YSZ) + e^-(Ni)$$
$$O^-(Ni) \rightleftharpoons O(Ni) + e^-(Ni)$$

These reactions appear as O1, O2, and O4, respectively, in Table III of Ref. 85. Each of these reactions, together with reaction Nos. 1–4 from Table 2 (which are O5, OH, H2, and H1, respectively), is illustrated pictorially in Fig. 7.

The possible reaction pathways for hydrogen oxidation in Vogler *et al.* are compared to experimental patterned-anode data published by Bieberle *et al.*[84] under a range of operating conditions. From various combinations of the seven charge-transfer reactions, only one reaction pathway, based on two hydrogen spillover reactions (Table 2, Nos. 3 and 4), was able to consistently describe the complete experimental data set. The double-hydrogen spillover pathway was then examined based on different modeling approaches/assumptions described in the literature: (A) a full reaction-diffusion model;[85] (B) a full reaction-diffusion model without water dissociation on YSZ, an approach previously employed by Goodwin *et al.*;[42,43] and (C) a charge-transfer model where the charge transfer takes place over the entire surface area as used by Gewies *et al.*,[86] which corresponds to the full model assuming infinitely fast surface transport. Each of the approaches involves solving Eq. 10 under the appropriate assumptions. The results are reproduced in Fig. 8 (adapted from Ref. 85), where lines in the figure are labeled with the apparent Tafel slope $\beta F/RT$ (*e.g.*, see Eq. 26). The transfer coefficient of the experimental data is close to unity, which is in good agreement with predictions from model A, whereas simulations B and C predict too high or too low apparent Tafel slopes.

4.1.5 The role of surface diffusion. Vogler *et al.*[85] also suggest that surface diffusion is a key process (at least for patterned anodes) contributing to the electrochemical behavior at the TPB. The electrochemically active surface area is confined to a narrow region (less than 100 nm) from the TPB, because of the interaction of fast surface reactions with slow surface diffusion. In fact, from all of the possible reaction pathways, the competitive adsorption of gas species on the electrode or electrolyte surface, as well as the following surface diffusion processes, are candidates for rate-limiting steps. Ihara *et al.*[87] investigated the detailed dependence of DC-polarization and interfacial conductivity of Ni-YSZ cermet anodes on the partial pressure of hydrogen. They developed a Langmuir reaction model, which links the chemical reactions on the anode with the electrical characteristics of the anode, such as the DC-polarization and the interfacial conductivity. In their

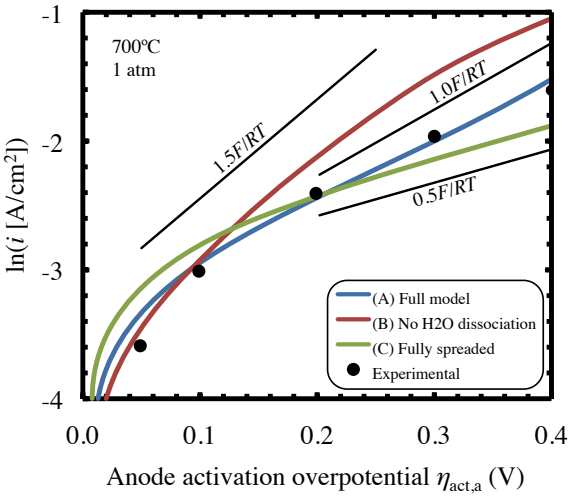

Fig. 8 Comparison of Tafel slopes for double hydrogen spillover at different model assumptions: (A) full reaction-diffusion model, (B) full reaction-diffusion model without H_2O dissociation on YSZ, and (C) fully spreaded charge-transfer model. The numbers indicate the transfer coefficient β of the apparent Tafel slope $\beta F/RT$ (see Eq. 26). Figure and description reproduced from Ref. 85, though the slopes in that reference are incorrectly labeled $\beta RT/F$.

model, they assumed competitive adsorption equilibrium of H_2, H_2O, and O on Ni surfaces at the TPB, and assumed the rate-determining step to be Langmuir-type reactions of H_{ad} with O_{ad}. Ihara *et al.* concluded that their measured dependencies and previously published dependencies were both successfully reproduced by their reaction model. Furthermore, they found the adsorption of H_2 at the TPB (which generally occurs on the metal surface) is affected by the presence of the electrolyte (YSZ) at the TPB in a cermet anode. Williford and Chick[88] proposed a model with surface diffusion to explain the limiting current density. They used an analogous circuit model to determine the dominant reaction pathway depending on operating conditions, especially when the SOFC is working at high current density or high fuel utilization. The dominant reaction pathways considered in the model include competitive adsorption of reactants in areas adjacent to the reactive TPB sites, and slow surface diffusion to the reactive sites. It was suggested that SOFC anode design improvements should focus on optimization of the reactive area, adsorption, and surface diffusion at the anode/electrolyte interface.

4.1.6 Detailed mechanism with kinetic data. Efforts[42–46] to develop detailed charge-transfer kinetics in terms of elementary reaction steps in a manner that parallels treatment of thermal heterogeneous chemistry[40,41] are very new. These mechanisms are generally based on pattern-anode experiments[77,84,85,89,90] that expose the TPB and remove any transport limitations of fuel delivery or product removal from reactive sites. It would also allow competing charge-transfer pathways to play themselves out without having to make an assumption about which is dominant in accordance with real-time operating conditions (*e.g.*, changing gas composition at the TPB) or what step is rate determining. However, there is not yet a clear understanding of the electrode kinetics, and more often than not, the number of unknowns cannot be sufficiently determined from available data. Nonetheless, the process provides significant quantitative insight about the fundamental chemical and transport processes responsible for charge transfer.[43]

Let us take, for example, a recent detailed description of the reaction mechanism for hydrogen charge transfer.[43] Table 3 outlines a set of heterogeneous surface reactions and several different charge-transfer pathways for H_2-H_2O in a Ni-YSZ anode. Reactions 1–5 describing the interactions of hydrogen, oxygen, and steam on nickel are adopted from Deutschmann and co-workers,[40,41] and are a subset of a larger mechanism describing methane reforming on nickel (see Table 8). In these reactions, (Ni) represents an empty site on the nickel surface, H(Ni) is an adsorbed H atom, and so on. Similarly, reactions 6–9 detail the interactions of species on the YSZ surface, for which there are two types of surface sites (χ) and (Zr), as well as bulk species O_O^{2-} and V_O representing a bulk oxygen ion and vacancy, respectively.‡ Of the two surface site types, (Zr) is a surface-level zirconium cation site and (χ) is defined to be the position that a surface oxygen would occupy if it were present. For all reactions in Table 3, the forward rates are in Arrhenius form, and the reverse rates are calculated from the thermodynamic properties in Table 4. This maintains strict thermodynamic consistency. Additional details about the reactions and their rates can be found in Goodwin *et al.*[43]

In addition to the surface reactions, Table 3 also lists four different charge-transfer pathways for hydrogen electrochemical oxidation. Each of these pathways is considered separately with the surface mechanisms in a model that can be used to predict polarization characteristics and Tafel plots. The predicted Tafel plots are then compared directly with patterned-anode experiments from Mizusaki *et al.*[77] and the resulting reaction-rate parameters are those that give the best fit to the experimental data for each potential mechanism.

The results of a computational model that represents the coupled behavior of elementary surface chemistry, electrochemistry, and transport in the vicinity of the TPB are illustrated in Figure 9, reproduced from Goodwin *et al.*[43]. The

‡ The notation used in this instance is chosen to match the reference from where it was obtained (Ref. 43) and does not follow standard Kröger-Vink notation, where the lattice oxygen ion would normally have neutral charge ($O_O^{\times}$) and the vacancy a double positive charge ($V_O^{\cdot\cdot}$). Instead, the lattice oxygen ion is given a double negative charge and the vacancy is neutral. In either case, the relative difference between the ion and the vacancy are identical.

Table 3 Summary of the H_2-H_2O-Ni-YSZ surface and charge-transfer reactions in Ref. 43 [a]

	Reaction	A [b] or γ_0 [c]	n	E [b] or β_a
1	$H_2 + 2(Ni) \rightleftharpoons 2H(Ni)$	0.01 [c]	0.0	0.0
2	$H_2O + (Ni) \rightleftharpoons H_2O(Ni)$	0.10 [c]	0.0	0.0
3	$H(Ni) + O(Ni) \rightleftharpoons (Ni) + OH(Ni)$	$5.00 \times 10^{+22}$	0.0	97.9
4	$H(Ni) + OH(Ni) \rightleftharpoons (Ni) + H_2O(Ni)$	$3.00 \times 10^{+20}$	0.0	42.7
5	$2OH(Ni) \rightleftharpoons H_2O(Ni) + O(Ni)$	$3.00 \times 10^{+21}$	0.0	100.0
6	$O_O^{2-} + (\chi) \rightleftharpoons O^{2-}(\chi) + V_O$	$7.30 \times 10^{+12}$	0.0	80.1
7	$H_2O + (Zr) + O^{2-}(\chi) \rightleftharpoons OH^-(Zr) + OH^-(\chi)$	1.20×10^{-4} [c]	0.0	86.8
8	$OH^-(\chi) + (Zr) \rightleftharpoons OH^-(Zr) + (\chi)$	$2.00 \times 10^{+10}$	0.0	0.0
9	$H_2 + (Zr) + O^{2-}(\chi) \rightleftharpoons H^-(Zr) + OH^-(\chi)$	1.00×10^{-8} [c]	0.0	20.0
	Oxygen spillover			
OS1	$O^{2-}(\chi) \rightleftharpoons O^-(\chi) + e^-(Ni)$	$2.66 \times 10^{+06}$	0.0	0.50 [d]
OS2	$O^-(\chi) + (Ni) \rightleftharpoons O(Ni) + (\chi) + e^-(Ni)$	$2.66 \times 10^{+08}$	0.0	0.50 [d]
	Hydrogen spillover (fixed $\beta = 1/2$)			
HF1	$H(Ni) + O^{2-}(\chi) \rightleftharpoons (Ni) + OH^-(\chi) + e^-(Ni)$	$5.00 \times 10^{+12}$	0.0	0.50 [d]
HF2	$H(Ni) + OH^-(\chi) \rightleftharpoons H_2O(Ni) + (\chi) + e^-(Ni)$	$4.09 \times 10^{+09}$	0.0	0.50 [d]
	Hydrogen spillover (single channel)			
HS1	$H(Ni) + O^{2-}(\chi) \rightleftharpoons (Ni) + OH^-(\chi) + e^-(Ni)$	$5.00 \times 10^{+12}$	0.0	0.50 [d]
HS2	$H(Ni) + OH^-(\chi) \rightleftharpoons H_2O(Ni) + (\chi) + e^-(Ni)$	$1.55 \times 10^{+09}$	0.0	0.30 [d]
	Hydrogen spillover (dual channel [e])			
HD1	$H(Ni) + O^{2-}(\chi) \rightleftharpoons (Ni) + OH^-(\chi) + e^-(Ni)$	$5.00 \times 10^{+12}$	0.0	0.50 [d]
HD2	$H(Ni) + OH^-(\chi) \rightleftharpoons H_2O(Ni) + (\chi) + e^-(Ni)$	$8.50 \times 10^{+08}$	0.0	0.25 [d]
HD3	$H(Ni) + OH^-(\chi) \rightleftharpoons H_2O(Ni) + (\chi) + e^-(Ni)$	$1.36 \times 10^{+10}$	0.0	0.80 [d]

[a] Ni surface-site density is 1.7×10^{-9} mol/cm^2. The total site density on the oxide surface is 2.5×10^{-9} mol/cm^2, with 1.25×10^{-9} mol/cm^2 available each to (Zr) and (χ) sites.

[b] Arrhenius parameters for the rate constants written in the form: $k = AT^n \exp(-E/RT)$. The units of A are given in terms of moles, centimeters, and seconds. E is in kJ/mol.

[c] Sticking coefficient in the form of $\gamma = \gamma_0 \exp(-E/RT)$. The sticking coefficient is dimensionless.

[d] Because experimental data were available only at a single temperature of 700°C (973 K), it was not possible to further separate the rate constants into an activation energy and pre-exponential factor. The number listed in the far right column is the anodic symmetry factor β_a.

[e] The physical basis for such a possibility is that reactions with the same reactants and products may occur on different types of surface sites (*e.g.*, steps or ledges), resulting in different rates.

Goodwin model (which is based on integration of Eq. 10) is applied to assist the development and evaluation of H_2 charge-transfer reaction mechanisms for Ni-YSZ anodes. Previously published patterned-anode experiments from Mizusaki *et al.* [77] are used to evaluate the different electrochemical charge-transfer mechanisms appearing in Table 3. For each of these pathways, the best-fit kinetic parameters were determined that provided a closest match to the experimental results. Of the reaction schemes, the results show that a hydrogen-spillover mechanism can explain the Mizusaki polarization measurements over a wide range of gas compositions with anodic and cathodic biases. [43]

Although much effort has been focused on the mechanisms and elementary kinetic models for H_2 oxidation in the SOFC anode, it is evident from the above discussion that there is no general consensus among researchers. In summary, the primary differences include: (*i*) the location where thermochemical and electrochemical reactions take place, *i.e.*, catalyst or electrolyte; and (*ii*) the limiting reaction steps under different operating conditions (*e.g.*, adsorption and desorption of hydrogen and water, charge-transfer reactions, surface diffusion processes). To clarify these issues, more detailed experimental data and refinement of elementary kinetic and transport parameters are required to improve quantitative model predictions over a wide range of conditions.

Table 4 Standard-state thermodynamic properties for species at 700°C from Ref. 43

Species	H° (kJ/mol)	S° (J/mol/K)
H_2	19.9	165.3
H_2O	−217.8	231.5
O_2	21.8	242.3
(Ni)	0.0	0.0
H(Ni)	−32.7	39.6
H_2O(Ni)	−281.6	122.5
OH(Ni)	−199.7	99.6
O(Ni)	−228.7	32.4
V_O	0.0	0.0
O_O^{2-}	−85.6	148.4
(χ)	0.0	0.0
$O^{2-}(\chi)$	−85.6	139.6
$O^-(\chi)$	−85.6	139.6
$OH^-(\chi)$	−173.8	124.5
(Zr)	0.0	0.0
OH^-(Zr)	−208.8	124.5
H^-(Zr)	90.3	37.0

4.2 CO electrochemical oxidation

CO and H_2 are the main species in fuel derived from steam reforming (both external and internal), coal gasification, or biogas. Research on the subject of CO electrochemical oxidation is much less expansive than H_2 electrochemical oxidation. Because of the promising and prominent role of CO as a fuel for SOFCs, knowledge and understanding of the CO reaction mechanism is of significant importance.

Some study of CO electrochemistry using nickel-pattern anodes, nickel-point anodes, and Ni-YSZ porous anodes can be found in the literature. It is generally agreed that the electrochemical reaction rate of CO is lower than that of H_2.[33,91–93] When pure CO is supplied to a porous Ni-YSZ anode, Jiang and Virkar[33] report that the maximum power density reaches only about 40% of that obtained using pure H_2. Similarly, according to experimental results using a nickel-patterned anode on YSZ by Sukeshini *et al.*,[90] the maximum power density using CO is about 50% of that obtained from using H_2 only. While the lower power density from patterned-anode experiments is likely the result of charge-transfer kinetics alone, the reduced power output from the porous anode is a combination of slow CO electrochemical kinetics and increased resistance to transport of CO to reaction sites because the relatively heavy CO molecules are characterized by a lower diffusivity than their lighter H_2 counterparts. Therefore, in real systems (*i.e.*, those using porous electrodes), not only will CO be slower to reach the TPB, but it will also be slower to react there.

Matsuzaki and Yasuda[91] studied the electrochemical oxidation rate of H_2 and CO with a porous Ni-YSZ cermet electrode and YSZ electrolyte under constant oxygen partial pressure. They found that the polarization resistance increased when the CO concentration ratio $p_{CO}/(p_{H_2}+p_{CO})$ exceeded 0.2 at 750°C and 0.5 at 1000°C. The electrochemical oxidation rate of H_2 was 1.9–2.3 times higher than that of CO at 750°C, and 2.3–3.1 times higher at 1000°C. Even though the CO electro-oxidation rate is slower than H_2, Matsuzaki and Yasuda's results indicate that it has the same order of magnitude, differing only by a factor of two or three. That being the case, understanding the mechanism for electrochemical conversion of CO is absolutely necessary for systems using CO-dominant fuels, and may play a non-negligible role as a parallel charge-transfer pathway to H_2 electro-oxidation.

4.2.1 CO electrochemical oxidation mechanisms. A wide range of experimental conditions and electrode materials has resulted in several proposed reaction mechanisms and various rate-determining steps for CO electrochemical oxidation. Perhaps the first CO electro-oxidation mechanisms were proposed by Etsell and Flengas[94] for CO electrochemical oxidation on porous Pt-YSZ electrodes. The authors offered two possible mechanisms based on studies of the anodic reactions in the range 700–1100°C. The two mechanisms are:

1. Oxygen participation in charge transfer
$$O_O^\times(\text{YSZ}) + (\text{Pt/YSZ}) \rightleftharpoons O(\text{Pt/YSZ}) + V_O^{\cdot\cdot}(\text{YSZ}) + 2e^-(\text{Pt})$$
$$CO(g) + O(\text{Pt/YSZ}) \rightleftharpoons CO_2(g) + (\text{Pt/YSZ})$$
2. CO participation in charge transfer
$$CO(g) + O_O^\times(\text{YSZ}) \rightleftharpoons CO_2(g) + V_O^{\cdot\cdot}(\text{YSZ}) + 2e^-(\text{Pt})$$

In the notation above, the only surface species is adsorbed atomic oxygen O(Pt/YSZ) on the metal or electrolyte surface, and empty surface sites (Pt/YSZ). Within the YSZ electrolyte, $O_O^\times$(YSZ) is a lattice oxygen and $V_O^{\cdot\cdot}$(YSZ) is an oxygen vacancy. The only other species e^-(Pt) is an electron within the Pt anode.

Mechanism 1 postulates that adsorbed oxygen O(Pt/YSZ) is formed via the electrochemical charge-transfer reaction transferring oxygen from bulk YSZ to the anode or electrolyte surface. The adsorbed oxygen is subsequently used in the second reaction to oxidize gaseous CO, producing gas-phase CO_2. In other words, CO does not participate in the charge-transfer reaction directly, and instead reacts with the intermediate O(Pt/YSZ) from the charge-transfer reaction (*i.e.*, the first reaction in mechanism 1) involving oxygen species only. This mechanism also appears in Table 5 as mechanism 1 (note the nomenclature uses generic material names in place of spe-

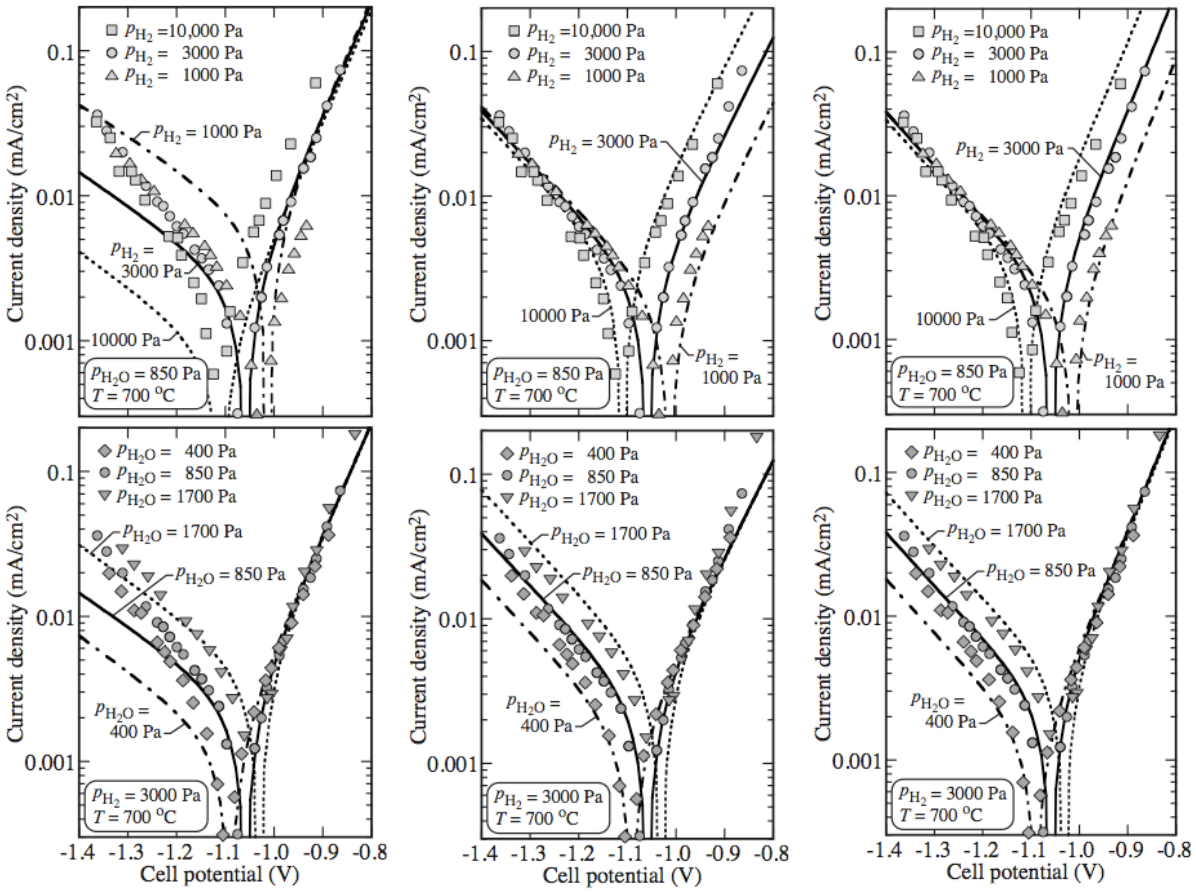

Fig. 9 Comparison between the H_2 charge-transfer mechanisms in Table 3 and the Mizusaki[77] measurements in the form of Tafel plots. The left pair of plots show results using the oxygen-spillover model (reactions OS1 and OS2). The center pair of plots show results using the single-channel hydrogen-spillover model (reactions HS1 and HS2). This model is an improvement on the fixed-β model. The right pair of plots show results using the dual-channel hydrogen-spillover model (reactions HD1, HD2, and HD3). The physical basis for such a possibility is that reactions with the same reactants and products may occur on different types of surface sites (*e.g.*, steps or ledges), resulting in different rates. In all cases, the upper panel is for fixed p_{H_2O} and varying p_{H_2}. The lower panel is for fixed p_{H_2} and varying p_{H_2O}. The system is isothermal at 700°C and 1 atm. The reaction A parameters are adjusted to achieve a best fit to the data. Figures and caption adapted from Goodwin *et al.*[43]

cific names, *e.g.*, "a" for anode instead of "Pt"). Under conditions when the charge-transfer reaction in mechanism 1 is slow, the exchange current density has the following form[94]

$$i_0 = k(1-\theta_{CO})\left(\frac{p_{CO_2}}{p_{CO}}\right)^{1-\alpha} \tag{29}$$

where k is a constant, θ_{CO} is the surface CO coverage, and α is around 1/2.

In contrast to this, gas-phase CO and CO_2 are directly involved in the electrochemical reaction of mechanism 2 (above) appearing in Etsell and Flengas. An exchange current density derived from mechanism 2 has the form[94]

$$i_0 = k(1-\theta_{CO})p_{CO_2}^{1-\alpha}p_{CO}^{\alpha}, \tag{30}$$

which supports the experimental observations of Etsell and Flengas in that it increases with increasing CO partial pressure (unlike Eq. 29). The same dependence is obtained if CO is assumed to be adsorbed on the surface (with an additional adsorption/desorption reaction added), and based on these findings, the authors note that gaseous or adsorbed CO and gaseous CO_2 must participate directly in the electrochemical steps of the electrode reaction. For a relatively invariant surface coverage θ_{CO}, and for $\alpha \approx 1/2$, the exchange current density of Eq. 30 will peak near 50% CO in CO_2. Aaberg *et al.*[97] later report that the measured exchange current density for CO-CO_2 mixtures on Ni-YSZ cermet anodes has a maximum around 45% CO in CO_2, which is in direct agreement with this. The experimental data of Aaberg *et al.* correspond, to some extent, to the second mechanism of Etsell and Flen-

Table 5 CO electrochemical oxidation mechanisms appearing in Ref. 95 [a]

Mechanism	Description and charge-transfer steps
1	*Oxidation of gaseous CO by adsorbed atomic oxygen.* Transfer of oxygen from the bulk electrolyte across the gas/electrolyte interface close to the TPB, followed by oxidation of CO by adsorbed atomic oxygen O_{ad} on the surface of the *electrode or electrolyte* (see Etsell and Flengas[94]) $$O_O^{\times}(\text{el}) + (a/\text{el}) \rightleftharpoons O(a/\text{el}) + V_O^{\cdot\cdot}(\text{el}) + 2e^-(a)$$ $$CO(g) + O(a/\text{el}) \rightleftharpoons CO_2(g) + (a/\text{el})$$
2	*Oxidation of adsorbed CO by adsorbed atomic oxygen.* In a CO_2-rich atmosphere, surface-adsorbed oxygen *on the electrolyte* reacts at the TPB with CO_{ad} on the anode forming adsorbed CO_2 species, also on the anode (see Mizusaki *et al.*[96]) $$O_O^{\times}(\text{el}) + (\text{el}) \rightleftharpoons O(\text{el}) + V_O^{\cdot\cdot}(\text{el}) + 2e^-(a)$$ $$CO(a) + O(\text{el}) \rightleftharpoons CO_2(a) + (\text{el})$$ [b]
3	*Oxidation of adsorbed CO by lattice oxygen in the electrolyte.* The lifetime of adsorbed atomic oxygen on the electrolyte is sufficiently short so that charge transfer proceeds directly between CO_{ad} and lattice oxygen close to the TPB $$CO(g) + (a/\text{el}) \rightleftharpoons CO(a/\text{el})$$ $$O(a/\text{el}) + O_O^{\times}(\text{el}) \rightleftharpoons CO_2(g) + V_O^{\cdot\cdot}(\text{el}) + 2e^-(a) + (a/\text{el})$$
4	*Oxidation of adsorbed, diffusing CO by lattice oxygen in the electrolyte.* Adsorbed CO moves to the TPB via surface diffusion, where it reacts with a lattice oxygen to produce $CO_2(g)$ $$CO(g) + (a/\text{el}) \rightleftharpoons CO(a/\text{el})$$ [c] $$CO(a/\text{el}) + O_O^{\times}(\text{el}) \rightleftharpoons CO_2(g) + V_O^{\cdot\cdot}(\text{el}) + 2e^-(a) + (a/\text{el})$$ Coverage of CO_{ad} controlled by surface diffusion $$\frac{\partial(\Gamma\theta_{CO})}{\partial t} = D_{ad}\frac{\partial^2(\Gamma\theta_{CO})}{\partial y^2} + k_{ad,CO}p_{CO}\Gamma(1-\theta_{CO}) - k_{des,CO}(\Gamma\theta_{CO})$$ [d]

[a] When appropriate, the originating reference is given in parentheses for each mechanism. Note the nomenclature uses generic material names in place of specific names (*e.g.*, "*a*" for anode catalyst instead of "Pt" or "Ni").

[b] In Ref. 95 this reaction appears as $CO_2(g) + (\text{el}) + (a) \rightleftharpoons O(\text{el}) + CO(a)$ coupled with the adsorption/desorption reaction $CO(a) \rightleftharpoons (a) + CO(g)$.

[c] The forward and reverse rate coefficients of this reaction are $k_{des,CO}$ and $k_{ad,CO}$, respectively. These appear in the diffusion equation described in the footnote below.

[d] In this equation, Γ is the total number of available adsorption sites and D_{ad} is the surface diffusion coefficient. The surface coverage of adsorbed CO is θ_{CO} and the rate coefficients are described in the footnote above.

gas, where CO and CO_2 are directly involved in the charge-transfer step. These authors also note that the CO polarization resistance is 2–5 times higher than H_2.

Mizusaki *et al.*[96] also studied CO oxidation on porous Pt-YSZ electrodes for typical SOFC operating temperatures in the range 600–1000°C. In an effort to avoid carbon deposition and subsequent fouling of the anode, the CO-CO_2 ratio of the fuel stream was selected to be CO_2-rich for most cases (i.e, ratios in the range 10^{-4}–10^{1}). Based on their experimental observations, Mizusaki *et al.* suggest a reaction rate proportional to 1/2-powers of the reactant activities (*i.e.*, gas-phase partial pressures and surface coverages), which is controlled by a simple chemical step at the TPB between adsorbed CO and CO_2 on the Pt surface and adsorbed oxygen on the electrolyte surface. In equation form,

$$O_O^{\times}(\text{YSZ}) + (\text{YSZ}) \rightleftharpoons O(\text{YSZ}) + V_O^{\cdot\cdot}(\text{YSZ}) + 2e^-(\text{Pt})$$

$$CO(\text{Pt}) + O(\text{YSZ}) \rightleftharpoons CO_2(\text{Pt}) + (\text{YSZ})$$

This appears as mechanism 2 in Table 5, and is very similar to mechanism 1 of Etsell and Flengas. The difference is that adsorbed oxygen O(YSZ) is assumed to exist only on the electrolyte surface, and that both adsorbed CO and CO_2 participate in the chemical step (second reaction) as opposed to both being gas-phase species (or even adsorbed CO and gaseous CO_2).

4.2.2 The role of surface diffusion. Matsuzaki and Yasuda[91] investigated the characteristics of CO electrochemical oxidation at the interface of a porous Ni-YSZ cermet elec-

trode and YSZ electrolyte, and concluded that the lower electrochemical oxidation rate of CO (compared to that of H_2) is caused mainly by the larger diffusion resistance of CO on the electrode surface at 750°C. At higher temperature (1000°C), both surface diffusion and charge-transfer resistance contribute to slow oxidation rates. Lauvstad *et al.*[95,98] studied the polarization curves and impedance response of a solid metal point electrode in contact with a solid, oxygen-ion conducting electrolyte (*i.e.*, Pt or Ni on YSZ) in CO-CO_2 atmospheres. This setup minimizes any limitations caused by gas-phase mass transport so that reaction pathways and rate-determining steps can be deduced. The overall electrochemical reaction is assumed to proceed in elementary steps, such as adsorption, diffusion of adsorbed species, and charge transfer. They analyze four electrochemical oxidation mechanisms of CO with different charge-transfer steps. The four mechanisms are detailed in Table 5. Mechanisms 1 and 2 were adopted from Etsell and Flengas,[94] and Mizusaki *et al.*,[96] respectively, and include gas-phase species or species adsorbed on the surface of the electrode and/or electrolyte. For mechanism 2, Lauvstad *et al.* only consider the adsorbed species O_{ad} and CO_{ad} and assume gaseous $CO_2(g)$. This is in contrast to Mizusaki *et al.* who assume adsorbed $CO_2(a)$ on the anode surface. Charge transfer for this mechanism is assumed to proceed as in mechanism 1 with "*a*/el" (indicating anode or electrolyte) replaced with "el" (electrolyte only). Mechanism 3 is a limiting case of mechanism 2, where Lauvstad *et al.* assume the lifetime of adsorbed atomic oxygen on the electrolyte surface to be sufficiently short so that charge transfer occurs directly between CO_{ad} (the only adsorbed species) and lattice oxygen near the TPB. This mechanism is essentially the same as mechanism 1—under the same assumption regarding the lifetime of O_{ad}—with adsorbed rather than gaseous CO. Mechanism 4 includes the same adsorption/desorption/charge-transfer reactions of mechanism 3, with the incorporation of surface diffusion of CO_{ad} species, which may exist on the electrode and/or electrolyte surface. In all other mechanisms, surface diffusion is assumed fast so that adsorbed species coverages are uniform.

Among these four possible mechanisms, modeling results[95] and experimental measurements[98] of polarization curves and EIS indicate that mechanism 2 qualitatively mimics the experimental impedance spectra over the entire frequency range under all experimental conditions for both (Pt and Ni) electrode materials (with the exception of Ni at cathodic overpotentials). In particular, only mechanism 2 reproduces the low frequency inductive behavior, which is consistent with a reaction mechanism involving two adsorbed intermediates. The Warburg impedance (associated with mass-transfer diffusion limitations), which may result from mechanism 4 under certain conditions, was never observed, so the assumption underlying the development of mechanisms 1, 2, and 3 (*i.e.*, that diffusion is a fast process) is justified. The fact that limiting currents are observed is thus not an indication of diffusion limitations, but is probably related to insufficient supply/removal rates of adsorption/desorption processes taking place in the vicinity of the TPB.[98]

4.2.3 Detailed mechanism with kinetic data. A more recent, and perhaps the most comprehensive, analysis of CO charge transfer and reaction kinetics on Ni-YSZ anodes appears in Yurkiv *et al.*[46] The authors examine three possible charge-transfer pathways, but limit their analysis to oxygen-spillover mechanisms only (*i.e.*, only oxygen species are involved in charge transfer at the TPB as oxygen ions in the electrolyte give up electrons and move to the anode). The CO (or any fuel for that matter) is then oxidized by the oxygen that resides on the anode surface. A summary of the surface reactions and three charge-transfer mechanisms appearing in Yurkiv *et al.* are reproduced in Table 6. The kinetic parameters used for each reaction are also given in Table 6. Standard-state thermodynamic properties for reaction species are reproduced from the same reference and appear in Table 7. Note that the values given are referenced to the vacancies of the associated phase.

Reactions 1–4 in Table 6 represent reactions on the Ni surface, reactions 5–7 on the YSZ surface, and the three different charge-transfer mechanisms appear as $O1+O2$, $O3+O4$, and O5, respectively. Each mechanism includes three possible species on the anode surface—CO(Ni), CO_2(Ni), O(Ni)—and empty surface sites (Ni). In $O3+O4$ an additional surface species $O^-(Ni)$ is allowed on the anode surface, for a total of four adsorbed species plus empty sites. The only bulk species is an electron within the anode $e^-(Ni)$. On the electrolyte surface, there are adsorbed CO(YSZ), O(YSZ), oxygen ions $O^{2-}(YSZ)$, and empty sites (YSZ). It is interesting to note that adsorbed atomic oxygen on the electrolyte O(YSZ) is consumed in the forward direction of reaction 7, yet it is not produced in any other reaction. The coverage of O(YSZ) therefore only depends on the equilibrium of reaction 7. An additional YSZ surface species $O^-(YSZ)$ is introduced through the charge-transfer reactions $O1+O2$. Within the bulk electrolyte there are oxygen ions $O_O^\times$ and vacancies $V_O^{\cdot\cdot}$.

The results of a computational model (based on Eq. 10 and the framework following it) that represents the coupled behavior of elementary surface chemistry, electrochemistry, and transport in the vicinity of the TPB are illustrated in Figure 10, reproduced from Yurkiv *et al.*[46]. The model by Bessler and co-workers (see Table 6) is used for the evaluation of CO charge-transfer reaction mechanisms for Ni-YSZ anodes in accordance with patterned-anode data from Lauvstad *et al.*[98] Their results are most consistent with an oxygen-spillover mechanism at the TPB proceeding through steps O1 and O2 in Table 6.

To our knowledge, Yurkiv *et al.*[46] are the first to publish a

Table 6 Summary of the CO-CO_2-Ni-YSZ surface and charge-transfer reactions in Ref. 46 [a]

	Reaction	A [b] or γ_0 [c]	n	E [b] or β_a
1	$CO + (Ni) \rightleftharpoons CO(Ni)$	5.0×10^{-1} [c]	0.0	0.0
2	$CO_2(Ni) \rightleftharpoons (Ni) + CO_2$	$7.0 \times 10^{+11}$	0.0	41.0
3	$CO + O(Ni) \rightleftharpoons (Ni) + CO_2$	$1.0 \times 10^{+23}$	0.0	155.0
4	$CO(Ni) + O(Ni) \rightleftharpoons (Ni) + CO_2(Ni)$	$2.0 \times 10^{+19}$	0.0	123.6
5	$CO + (YSZ) \rightleftharpoons CO(YSZ)$	4.0×10^{-2} [c]	0.0	0.0
6	$CO + O(YSZ) \rightleftharpoons (YSZ) + CO_2$	$1.0 \times 10^{+20}$	0.0	158.1
7	$O^{2-}(YSZ) + V_O^{\cdot\cdot}(YSZ) \rightleftharpoons (YSZ) + O_O^{\times}(YSZ)$	$1.6 \times 10^{+22}$	0.0	90.9
O1	$O^{2-}(YSZ) \rightleftharpoons O^-(YSZ) + e^-(Ni)$	8.4×10^{-6}	0.0	0.5 [d]
O2	$O^-(YSZ) + (Ni) \rightleftharpoons O(Ni) + (YSZ) + e^-(Ni)$	7.4×10^{-1}	0.0	0.5 [d]
O3	$O^{2-}(YSZ) + (Ni) \rightleftharpoons O^-(Ni) + (YSZ) + e^-(Ni)$	5.3×10^{-6}	0.0	0.5 [d]
O4	$O^-(Ni) \rightleftharpoons O(Ni) + e^-(Ni)$	2.1×10^{-1}	0.0	0.5 [d]
O5	$O^{2-}(YSZ) + (Ni) \rightleftharpoons O(Ni) + (YSZ) + 2e^-(Ni)$	4.9×10^{-6}	0.0	0.5 [d]

[a] Ni and YSZ surface-site densities are 6.1×10^{-9} mol/cm^2 and 1.3×10^{-9} mol/cm^2, respectively. Anodic and cathodic symmetry factors of the charge-transfer reactions are 1/2.

[b] Arrhenius parameters for the rate constants written in the form: $k = AT^n \exp(-E/RT)$. The units of A are given in terms of moles, centimeters, and seconds. E is in kJ/mol.

[c] Sticking coefficient in the form of $\gamma = \gamma_0 \exp(-E/RT)$. The sticking coefficient is dimensionless.

[d] Because experimental data were available only at a single temperature of 876°C (1149 K), it was not possible to further separate the rate constants into an activation energy and pre-exponential factor. The number listed in the far right column is the anodic symmetry factor β_a.

Table 7 Standard-state thermodynamic properties for species at 876°C from Ref. 46

Species	H° (kJ/mol)	S° (J/mol/K)
CO	−84	238
CO_2	−353	275
O_2	26	247
(Ni)	0	0
CO(Ni)	−197	193
CO_2(Ni)	−394	205
O(Ni)	−222	39
O^-(Ni)	−222	39
(YSZ)	0	0
CO(YSZ)	−159	172
O^{2-}(YSZ)	−236	0
O^-(YSZ)	−236	0
O(YSZ) [a]	−236	0
$V_O^{\cdot\cdot}$(YSZ)	0	0
$O_O^{\times}$(YSZ)	−236	0

[a] Note that thermochemical data for O(YSZ) is not given in Ref. 46, so we use the same values as those reported for O^-(YSZ) and O^{2-}(YSZ).

two-step charge-transfer description of CO electro-oxidation. The kinetic parameters in Table 6 and thermochemical properties in Table 7 are obtained from various sources (when available) or empirically determined based on numerical simulations formulated around one of the charge-transfer mechanisms (*i.e.*, O1 + O2, O3 + O4, or O5—each of these appears graphically in Fig. 11), allowing for direct comparison to experimental steady-state polarization curves and electrochemical impedance spectra from Lauvstad *et al.* [98] Best agreement with the experimental data is obtained through reaction pathway O1 + O2 (see Fig. 10), in which oxygen spillover occurs in the second step. This is in contrast to O3 + O4, where oxygen spillover at the TPB takes place in the first step, and O5, which is a two-electron net reaction without the intermediate surface species. Although mechanism O1 + O2 yields good agreement with Tafel plots, it fails to reproduce the low-frequency inductive loop that was used as a determining factor in choosing a possible reaction pathway in Lauvstad *et al.*

4.2.4 Summary of published mechanisms. A review of the current literature (some mentioned above, some not) pertaining to CO electro-oxidation exposes several dissimilar or contradictory observations:

1. The dependence of the exchange current density i_0 on the partial pressures of CO (p_{CO}) and CO_2 (p_{CO_2}) are

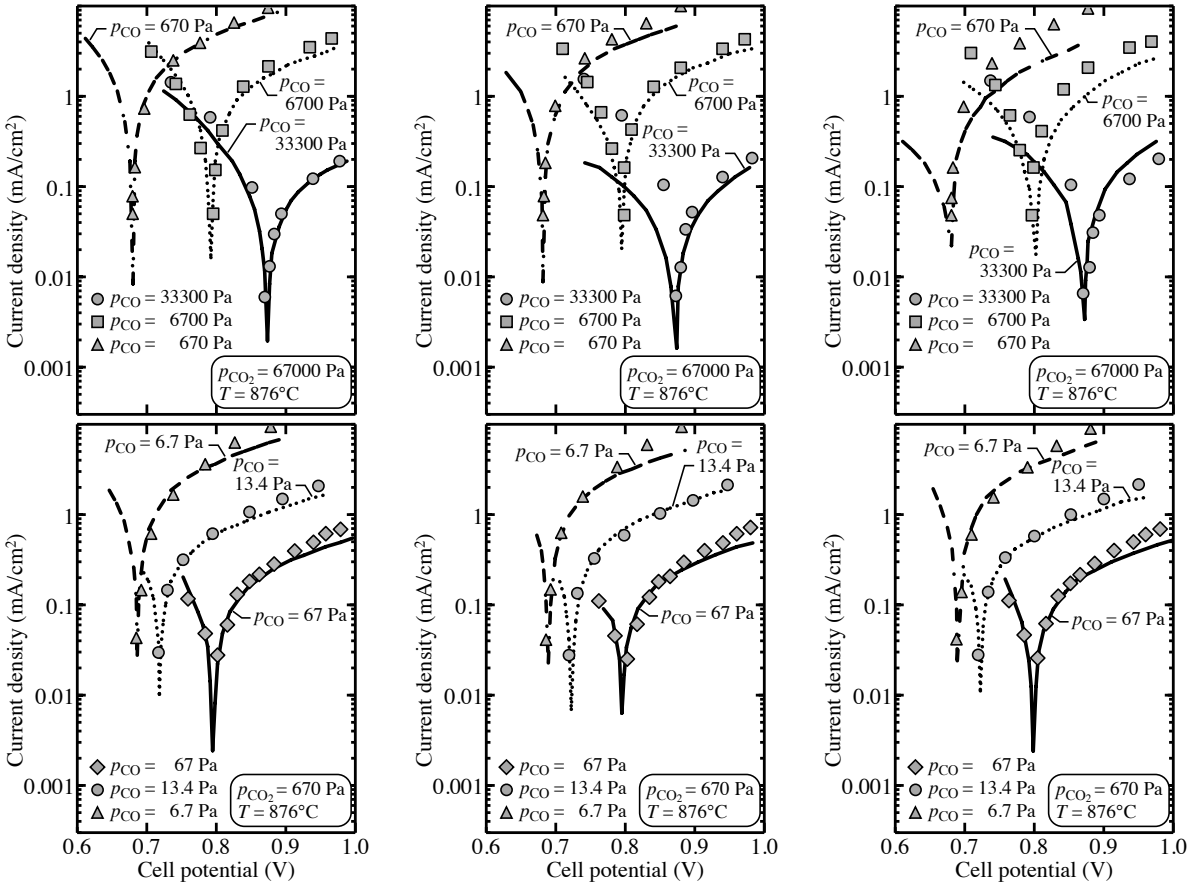

Fig. 10 Comparison between the CO charge-transfer mechanisms in Table 6 and the Lauvstad[98] measurements in the form of Tafel plots. The left pair of plots show results using the oxygen-spillover model described by reactions O1 and O2. The center pair of plots show results using a different oxygen-spillover model (reactions O3 and O4). The right pair of plots show results using the global oxygen-spillover reaction O5. All cases are for fixed p_{CO_2} and varying p_{CO}. The system is isothermal at 876°C and 1 atm (mixtures are balanced with Ar). The reaction A parameters are adjusted to achieve a best fit to the data. Figures reproduced from Yurkiv *et al.*[46]

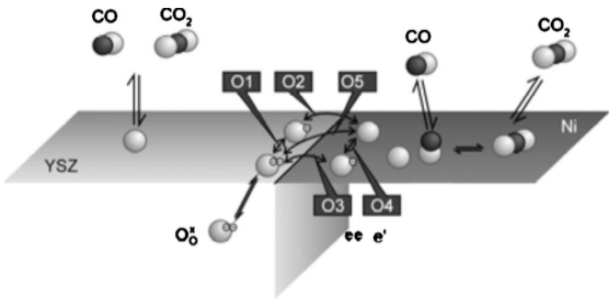

Fig. 11 Schematic illustration of the reaction mechanism and the three different charge-transfer pathways taking place at the three-phase boundary of Ni, YSZ, and gas phase. The reactions O1–O5 appear in Table 6. Picture and caption from Ref. 46.

reported to be $i_0 \propto p_{CO_2}^{1/2} p_{CO}^{1/2}$ by Etsell and Flengas[94] (see Eq. 30), but Boulenouar *et al.*[99] report average reaction orders of $p_{CO}^{1/4}$ and $p_{CO_2}^{1/2}$. However, Etsell and Flengas simultaneously varied both pressures in their experiments (as opposed to Boulenouar *et al.*, who systematically changed only one while keeping the other constant), so the reaction orders from Etsell and Flengas cannot be precisely determined. Nonetheless, there is likely a positive dependence of the exchange current density on both p_{CO} and p_{CO_2};

2. Aaberg *et al.*[97] report an apparent charge-transfer factor of $\alpha_a = \beta_a n_e = 1$, which gives an anodic charge-transfer coefficient of $\beta_a = 1/2$ because two electrons (*i.e.*, $n_e = 2$) are transferred in the overall electrochemical oxidation reaction of CO to CO_2. These values are consistent with

Etsell and Flengas[94] and Lauvstad *et al.*,[98] but they differ from Sukeshini *et al.*[90] who report α_a to be in the range 0.25–0.45;

3. Setoguchi *et al.*[100] report that the CO electrochemical oxidation reaction depends only on oxygen partial pressure (p_{O_2}) and is independent of the fuel partial pressures (which implies that CO and CO_2 do not directly participate in the charge-transfer reactions), but Matsuzaki and Yasuda[91] and Boulenouar *et al.*[99] show the exact opposite (*i.e.*, that CO electro-oxidation depends on the partial pressures p_{CO} and p_{CO_2}, but not p_{O_2});

4. The addition of water to the fuel was found to promote the kinetics of the overall CO electrode reaction in Habibzadeh,[89] but not in Sukeshini *et al.*[90] (Note that these two publications originate from the same group)

In addition to the striking ambiguities on some of the more basic dependencies, the charge-transfer reaction models can be divided into two pathways given by the following net reactions:

1. Oxygen participation in charge transfer as spillover at the TPB region[46,98,100]
$$O_O^{\times}(\mathrm{el}) + (a) \rightleftharpoons O(a) + V_O^{\cdot\cdot}(\mathrm{el}) + 2e^-(a)$$
2. CO (adsorbed or gas-phase) direct participation in charge transfer[89,90,94,97]
$$CO(g/a) + O_O^{\times}(\mathrm{el}) \rightleftharpoons CO_2(g) + V_O^{\cdot\cdot}(\mathrm{el}) + 2e^-(a)$$

The same course of development for charge-transfer pathways is found in the H_2 electrochemistry literature discussed in the foregoing sections. The two most frequently studied pathways in H_2 electrochemistry are a hydrogen-spillover mechanism and an oxygen-spillover mechanism. Vogler *et al.*[85] examine seven possible H_2 charge-transfer pathways, including hydrogen- and oxygen-spillover mechanisms, and find that only hydrogen spillover yields good agreement with the complete experimental data set from Bieberle *et al.*[84] on Ni-patterned anodes. Further, Goodwin *et al.*[42,43] also find support for the hydrogen-spillover mechanism based on comparison between modeling results and experimental data from Mizusaki *et al.*,[77] because it is the only pathway that provides good quantitative representation of measured polarization behavior over a wide range of gas-phase compositions with both anode and cathode biases. It is generally accepted then that hydrogen spillover is the more probable pathway in the H_2 electro-oxidation mechanism.

Clearly, the same understanding of CO electrochemistry does not yet exist, but because of its arguably equal (and sometimes greater, depending on the system) importance, research is actively being pursued in a manner analogous to H_2. To further the point, a general consensus concerning the mechanism of electrochemical oxidation of CO, or the role of the electrode versus that of the electrolyte in the reactions has not yet even been reached.

4.2.5 Unstable reaction rates. Due to carbon deposition on the anode surface and a possible partial delamination of the anode surface, unstable performance has been observed in SOFCs when operating with pure CO and a Ni-YSZ anode at 950°C. Holtappels *et al.*[101] studied the electrochemistry of CO-CO_2 oxidation on Ni-YSZ cermets as a function of CO and CO_2 partial pressures at 1000°C. Time-dependent reaction rates were observed for the CO oxidation reaction for oxygen activities corresponding to open circuit potentials in the range 0.75 to 1.01 V. The electrode changed between a passive state and several active states for the CO-CO_2 reaction. Periodic changes of the reaction rate for CO oxidation were observed every 30 and 80 s. The unstable reaction rates of the electrochemical oxidation of CO have been described by a "modified reconstruction model" as shown in Fig. 12.[101]

The impedance spectra recorded at the rest potential and the overpotential dependence of the CO oxidation rate indicated a change in the number of active sites in the reaction zone. In the active state, the CO oxidation reaction was more than one order of magnitude slower than the hydrogen oxidation reaction in Ni-YSZ cermet electrodes. Holtappels *et al.* point out that the direct observations of structural and chemical changes on Ni-catalyst surfaces after carbon deposition (discussed in Ref. 102) can be taken as indirect support of the described modified reconstruction model.

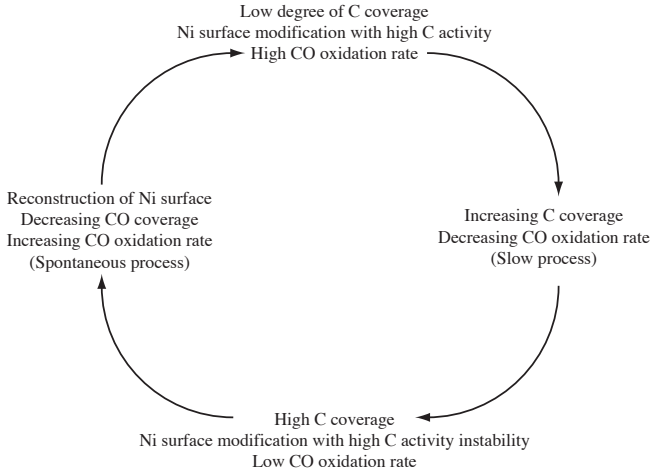

Fig. 12 Illustration of periodically changing CO oxidation rates, initiated by carbon deposition combined with reconstruction of the electrode surface. From Ref. 101.

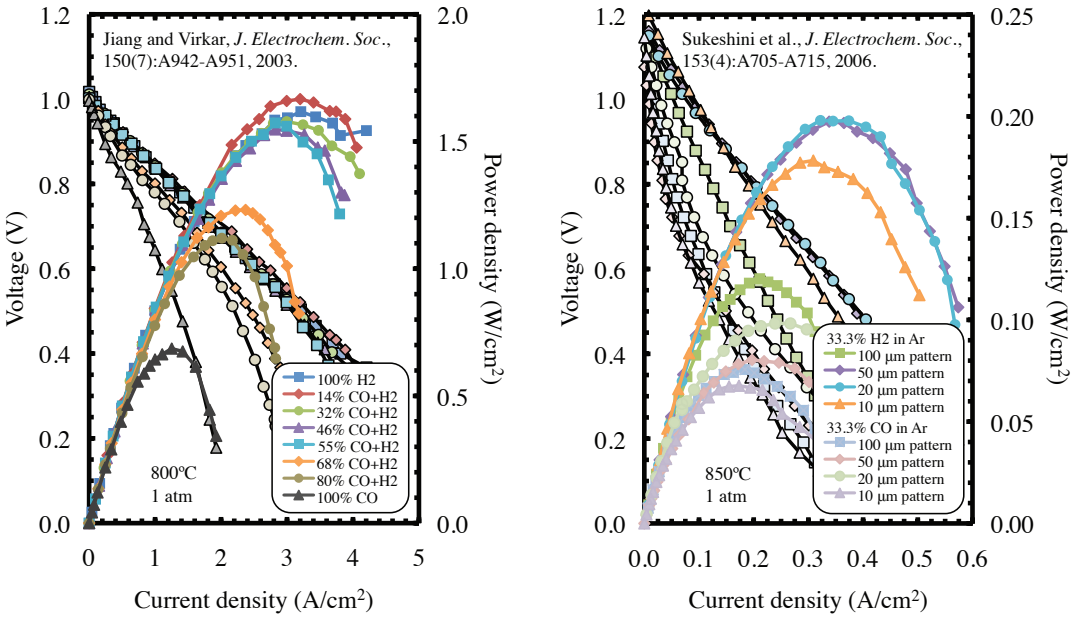

Fig. 13 SOFC performance operating on H_2-CO mixtures. The left panel is a reproduction of experimental measurements by Jiang and Virkar[33] using a Ni-YSZ porous anode at 800°C and 1 atm. The right panel is a reproduction of experimental measurements by Sukeshini *et al.*[90] using a nickel-pattern anode on YSZ at 850°C and 1 atm. Points are connected for clarity.

4.3 Syngas electrochemical oxidation

When CO and H_2 are both present in the fuel stream the mechanism becomes even more complicated because of parallel charge transfer, water-gas shifting, and the involvement and interaction of additional gaseous and adsorbed species. Jiang and Virkar[33] reported very little difference in anode-supported cell performance using H_2 and CO mixtures instead of pure H_2, even with CO concentration is as high as 55% (*e.g.*, refer to the left panel of Fig. 13). These results can be explained through the water-gas shift reaction occurring within the porous anode (water required for the reaction is a product of the electrochemical oxidation of H_2). As long as the H_2 content in the fuel stream is greater than 50%—so that sufficient H_2O can be produced to react with CO—high cell performance can be achieved because only a small amount of CO is left to directly participate in electrochemical oxidation. The cell performance under these conditions is similar to a cell operating with humidified H_2.

Other researchers have obtained results similar to those published by Jiang *et al.* For example, Weber *et al.*[103] studied the oxidation of H_2-CO mixtures in an electrolyte-supported SOFC using Ni-YSZ cermet anodes at 950°C, and observed a decrease in cell performance at high CO content ($>$ 90%). Eguchi *et al.*[92] also studied the effects of H_2 and CO mixture compositions on the performance of an electrolyte-supported Ni-YSZ planar cell. Results from their experiments indicate that H_2-H_2O-N_2 and CO-CO_2-N_2 systems provide almost the same open circuit voltage when the H_2-H_2O and CO-CO_2 ratios are equal at a temperature of 1000°C, as expected from thermodynamic equilibrium (*e.g.*, refer to Fig. 2). However, hydrogen is preferentially consumed by the electrode reaction, as evidenced by higher cell voltages for H_2 than CO under discharge conditions (*i.e.*, the slope of the *i-V* curve is steeper for CO oxidation as the voltage decreases from the open-circuit potential with increasing current density—refer to Fig. 13). The difference in discharge curves is ascribed to activation and/or concentration polarizations, with the latter assumed to be dominant.[92] Sasaki *et al.*[93] investigated the current-voltage characteristics and electrode impedance of a tubular-type SOFC for mixed fuel gases, consisting mainly of H_2, CO, H_2O and a carrier gas at 900°C and 1000°C. Their experiments confirm that CO-rich gases give comparable performance to that of H_2-rich gases, thus concluding that mixed gases such as coal-derived syngas are useful fuels for SOFC applications. Costa-Nunes *et al.*[104] further explore SOFC performance using two different composite anodes (Ni-YSZ and Cu-CeO_2-YSZ) with H_2, CO, and syngas fuels. They found that the kinetics of hydrogen electrochemical oxidation have positive order in H_2 partial pressure for Cu-CeO_2-YSZ and nearly zero order for Ni-YSZ. Likewise, the oxidation of CO was found to have a positive-order dependence on CO par-

tial pressure. They suggest that the higher activity of H_2 is due to spillover of H atoms from the Ni to the YSZ surface where oxidation takes place. In contrast, spillover of CO adsorbed on a metal to an oxide support generally does not occur (thus, reactions are limited to the TPB and less so on the metal and oxide surfaces near the TPB). These spillover effects are not observed for the Cu-CeO_2-YSZ anode since the metal is largely inert and reactions appear to take place on the ceria, which is active for both H_2 and CO oxidation. It is noteworthy that the performance of a cell with a Cu-Co-CeO_2-YSZ anode, even with a relatively thick electrolyte and operating at relatively low temperatures (700°C), exhibits a performance with CO that rivals that of some of the best Ni-YSZ cells operating on H_2.[104]

Habibzadeh[89] experimentally studied the electrochemical oxidation mechanisms and interactions of H_2-CO fuel mixtures on patterned-nickel anodes with different pattern geometries and various operating conditions (*e.g.*, cell working temperature, cell overpotential, fuel partial pressure, water partial pressure). Observations from the experiments are compared to predictions from a detailed electrochemistry model adopted from Bieberle and Gauckler[78,79] and linked to Cantera.[51] The elementary reaction steps used by Habibzadeh are summarized below:

1. Adsorption/desorption
   $CO(g) + (Ni) \rightleftharpoons CO(Ni)$
   $CO_2(g) + (Ni) \rightleftharpoons CO_2(Ni)$
   $O_2(g) + (Ni) \rightleftharpoons 2O(Ni)$
2. Surface reaction
   $CO(Ni) + O(Ni) \rightleftharpoons CO_2(Ni)$
3. One-step electrochemistry
   $CO(Ni) + O^{2-}(YSZ) \rightleftharpoons CO_2(Ni) + (YSZ) + 2e^-(Ni)$
4. Surface diffusion of CO

Evidence indicates that the rate-limiting process is primarily confined to a region very near the TPB. The combination of anode overpotential and cell temperature had clear and obvious effects on the rate-determining process: (*i*) at lower anode overpotential and lower temperature, charge transfer and surface diffusion (or adsorption/desorption) processes are both slow and potentially limiting; (*ii*) at higher anode overpotential or higher temperature, charge transfer is the limiting step. The results also indicate that the addition of H_2O to CO-CO_2 mixtures could reduce the low frequency resistance of the anode and increase the rate of the charge-transfer process (by almost two times for temperatures between 700°C and 800°C). This suggests a major role for the water-gas shift affecting gas-phase species, and/or the ability of H_2O to increase activity of the anode catalyst.

Although Habibzadeh's model is capable of qualitatively reproducing most of the experimental data, there are some notable shortcomings. For simulated EIS, the second loop, which is associated with surface transport of species (*i.e.*, surface diffusion or adsorption/desorption), is about six times smaller than that obtained by experimental measurement. This may be attributed to the fact that the relaxation frequency of the charge-transfer process in the model is about one order of magnitude higher than in experiments. This allows the model to be dominated by the higher frequency mode, and it will therefore not be able to capture processes occurring at lower relaxation frequencies. To capture effects of adsorption/desorption and surface diffusion, further work involving sensitivity studies and tweaking of the surface thermodynamics, particularly for YSZ surfaces, are necessary. This is critical for optimizing Ni-YSZ anode design for operation with CO-rich fuel streams.

Because there is no general agreement on and a lack of understanding of the mechanism for CO electrochemical oxidation when it is the primary fuel species, this in turn impacts the level of understanding for H_2-CO mixtures. There is not a clear or common conclusion on the oxidation mechanism, especially under different operating conditions. More carefully designed and detailed experimental studies, as well as elementary reaction models are needed to clarify the reaction pathways, kinetics, and interactions between H_2, CO, and other species.

4.4 Hydrocarbon electrochemical oxidation

Except for studies focusing on external or internal reforming of hydrocarbon fuels for use in SOFCs, additional interest has been given to the tolerance of SOFC anodes to direct conversion of dry hydrocarbon fuels. Direct conversion of a hydrocarbon means conversion in the SOFC without pre-mixing the fuel gas with steam or CO_2, and without processing the fuel before it enters the stack. There is some difference in the terminology found in the literature, and the use of "direct conversion" by many researchers, as well as the definition adopted here, is taken directly from Mogensen and Kammer.[31] Direct conversion therefore only involves electrochemical oxidation of the fuel and/or cracking products.

Murray *et al.*[28] reported the direct electrochemical oxidation of nearly pure CH_4 in SOFCs using a ceria-based anode, which resulted in power densities up to 0.37 W/cm^2 at 650°C. This performance is comparable to that of fuel cells operating on hydrogen. They concluded that direct oxidation of CH_4 is the primary anode reaction based on several observations. First, even after H_2O and CO_2 production, reforming rates are probably too low to compete with the direct electrochemical oxidation of CH_4. Low reforming rates are a result of small anode area (1 cm^2), low temperature, and flushing of products (*i.e.*, H_2O and CO_2) from the anode compartment

by relatively high fuel flow. Second, supporting evidence for direct oxidation of CH_4 is found in comparison of EIS obtained from anodes subjected to dry and humidified methane fuel. These cases give rise to impedance spectra with different shapes, and since the shape of the curve is related to the mechanism governing fuel oxidation, this revealed that the primary anode reaction was not consistent with a mechanism involving oxidation of hydrogen produced by reforming of humidified methane. Putna *et al.*[29] and Park *et al.*[105] also reported direct oxidation of CH_4 in SOFCs. Park *et al.*[38] more recently reported on the direct electrochemical oxidation of various hydrocarbons (methane, ethane, 1-butene, *n*-butane, and toluene) at 700°C and 800°C with a composite anode of copper and ceria (or samaria-doped ceria). They demonstrate stable operation without carbon formation in the anode, and that the final products of oxidation are CO_2 and H_2O. Experimental measurements of CO_2 production as a function of current density from methane and *n*-butane (C_4H_{10}) fuels using a Cu-ceria composite anode indicate that direct oxidation of CH_4 and C_4H_{10} occurs in a single step

$$\begin{aligned} CH_4 + 4O^{2-} &\rightleftharpoons CO_2 + 2H_2O + 8e^- \\ C_4H_{10} + 13O^{2-} &\rightleftharpoons 4CO_2 + 5H_2O + 26e^- \end{aligned}$$

They also report that only trace levels of CO were observed in the anode outlet when fueling with methane. This observation also supports direct single-step electro-oxidation.

Mogensen and Kammer[31] provide a comprehensive review of the conversion of hydrocarbons in SOFCs, and are critical of the likelihood of single-step electrochemical oxidation of a hydrocarbon fuel, even in the case of the simplest hydrocarbon, CH_4. Instead, the reactions may proceed via the following elementary reaction steps:

$$\begin{aligned} CH_4 + O^{2-} &\rightleftharpoons CH_3OH + 2e^- \\ CH_3OH + 2O^{2-} &\rightleftharpoons HCOOH + H_2O + 4e^- \\ HCOOH + O^{2-} &\rightleftharpoons CO_2 + H_2O + 2e^- \end{aligned}$$

Alternatively, cracking of methane followed by electrochemical oxidation of the cracking products likely follows a path given by[31]

$$\begin{aligned} CH_4 &\rightleftharpoons C + 2H_2 \\ C + 2O^{2-} &\rightleftharpoons CO_2 + 4e^- \\ H_2 + 2O^{2-} &\rightleftharpoons H_2O + 2e^- \end{aligned}$$

Mogensen *et al.* emphasized the importance of clarifying the precise mechanism of the hydrocarbon conversion process. It is important to distinguish between the different reaction pathways because the demands on the anode material differ significantly for these pathways. For example, an electrode designed for direct electrochemical oxidation of hydrocarbon should have a very high turnover rate of the hydrocarbon bond breaking. Cracking followed by electrochemical conversion of the cracking products requires an electrode that is both highly active for the cracking of methane and active for the oxidation of the cracking products. In other words, it is of great importance to know the pathway by which the conversion of hydrocarbon is to proceed in order to determine which properties of the anode should be optimized.[31]

4.5 Carbon electrochemical oxidation

Direct electrochemical oxidation of carbon also plays an important role when fueling SOFCs with carbon-based fuels. Anode stability can be seriously compromised by deposited carbon, and other SOFC components are susceptible to carbon buildup and eventual blockage if some method for removal of solid deposited carbon is not considered. For example, new work has shown that nanostructured barium oxide/nickel (BaO/Ni) interfaces (created by vapor deposition of BaO into Ni-YSZ) facilitate water-mediated carbon-removal reactions in the anode.[32] The nanostructures readily adsorb water, and the dissociated $OH_{ad}(BaO)$ from $H_2O_{ad}(BaO)$ reacts with $C_{ad}(Ni)$ near the BaO/Ni interface to produce CO and H species, which can be electrochemically oxidized at the TPB in the anode. The BaO/Ni-YSZ anode displayed stable operation and high power density in C_3H_8, CO, and gasified carbon fuels at 750°C, with no observable microstructural change and minimal carbon buildup. Refer to Table 1 for a comparison of peak power densities achieved with this cell and others operating with various fuels. To examine the mechanism of carbon removal, Yang *et al.* constructed models for DFT calculations. On the basis of that analysis, the most probable elementary processes on the anode with nanostructured BaO/Ni interfaces are predicted:[32]

Dissociative adsorption of H_2O on BaO:

$$H_2O \rightarrow H_{ad}(BaO) + OH_{ad}(BaO)$$

COH formation on Ni:

$$C_{ad}(Ni) + OH_{ad}(BaO) \rightarrow COH_{ad}(Ni)$$

CO and H formation on Ni (rate-determining):

$$COH_{ad}(Ni) \rightarrow CO_{ad}(Ni) + H_{ad}(Ni)$$

Diffusion to the TPB:

$$CO_{ad}(Ni) \rightarrow CO_{TPB};\ H_{ad}(Ni) \rightarrow H_{TPB}$$

CO oxidation at the TPB:

$$CO_{TPB} + O^{2-} \rightarrow CO_2 + 2e^-$$

H oxidation at the TPB:

$$2H_{TPB} + O^{2-} \rightarrow H_2O + 2e^-$$

In addition, electrochemical oxidation of solid carbon is of great importance to SOFC systems specifically designed for

direct carbon conversion, typically abbreviated SO-DCFC for solid-oxide direct carbon fuel cell (see, *e.g.*, Refs. 106–109). While the literature on electrochemical oxidation of carbon in molten-salt systems is vast, it is beyond the scope of this paper. Very little is known about the direct electrochemical conversion of solid carbon in an all-solid-state system. Pioneering work by the Danish company Dinex Filter Technology A/S on the electrochemical oxidation of carbon in a reactor constructed with porous ceria and catalytic active electrodes has been reported (see Ref. 31 for a reference to this and discussion), but the work is carried out under net oxidizing conditions—for diesel exhaust clean up—and not in an environment that is similar to that of the anode compartment in a fuel cell.

Gür and Huggins,[110] and subsequent more recent work from the same group (see, *e.g.*, Refs. 111–116) are studying SOFCs utilizing fluidized-bed or gasification-driven mechanisms to obtain CO gas from solid carbon via the Boudouard reaction. The design is in principle an integrated gasifier, so that the SOFC is operating on CO as fuel and not directly on solid carbon. While their work is certainly of importance, the direct electrochemical conversion of solid carbon is not the primary current-producing mechanism.

The concept of rechargeable direct carbon fuel cells (RDCFCs) has been published by Ihara *et al.*[118] Their cell used pyrolytic carbon deposited by thermal decomposition of dry methane as fuel, and they showed that the SOFC can generate electrical power in repeated charging (*i.e.*, repeated carbon-deposition cycles) and power-generation cycles—the deposited carbon allowed the cell to essentially operate as a battery, or with a fuel storage mode. Nickel-gadolinium-doped ceria (Ni-GDC) anodes showed 8.6 times higher power density (66.5 mW/cm^2) and 29 times more effective carbon mass used as fuel than traditional Ni-YSZ anodes. Hasegawa and Ihara[117] later studied the reaction mechanism for the oxidation of deposited carbon in a SOFC anode, and suggested the pathways illustrated in Fig. 14. Li *et al.*[106] recently published a more in-depth analysis of the mechanism for carbon direct electrochemical conversion, based on experimental investigation of CH_4-deposited carbon in an anode-supported cell consisting of a Ni-YSZ anode support layer (680 μm), a Ni-scandium-stabilized zirconium (Ni-ScSZ) anode active interlayer (15 μm), a ScSZ electrolyte layer (20 μm), and a LSM-ScSZ cathode layer (15 μm). The proposed mechanism appears as[106]

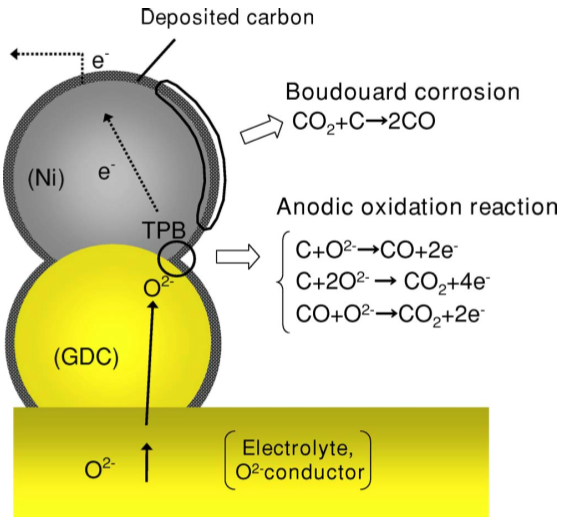

Fig. 14 Anode reaction mechanism of a rechargeable direct carbon fuel cell (RDCFC). TPB indicates the three-phase boundary. Picture and description from Ref. 117.

1. Oxygen-ion transfer between surface and bulk electrolyte
   $O_O^{\times} \rightleftharpoons O^{2-} + V_O^{\cdot\cdot}$
2. First O^{2-} adsorption
   $C_{RS} + O^{2-} \rightleftharpoons C_{RS}O^{2-}$
3. Fast discharge steps
   $C_{RS}O^{2-} \rightleftharpoons C_{RS}O^{-} + e^{-}$
   $C_{RS}O^{-} \rightleftharpoons C_{RS}O + e^{-}$
4. Desorption of CO *or* second O^{2-} adsorption by $C_{RS}O$
   $C_{RS}O \rightarrow CO(g)$
   $C_{RS}O + O^{2-} \rightleftharpoons C_{RS}O_2^{2-}$
5. Fast discharge and CO_2 desorption
   $C_{RS}O_2^{2-} \rightleftharpoons C_{RS}O_2^{-} + e^{-}$
   $C_{RS}O_2^{-} \rightleftharpoons CO_2(g) + e^{-}$

Net global reactions

$$C_{RS} + O^{2-} \rightleftharpoons CO(g) + 2e^{-}$$
$$C_{RS} + O^{2-} \rightleftharpoons CO_2(g) + 4e^{-}$$

During discharge, the O^{2-} is conducted into the anode ionic conductor YSZ, where it reacts with a carbon reactive site C_{RS} of the carbon deposited in the anode. Two single-electron discharge steps follow to form a double-bonded adsorbed structure $C_{RS}O$ (carbonyl group C=O, including adsorption with small and large lattice defects). The $C_{RS}O$ desorbs as CO or absorbs a second O^{2-} to eventually produce CO_2.[106]

A fundamental understanding of carbon electrochemical oxidation is of significant importance for SOFC anode design. Whether the goal is to mitigate carbon deposition to prevent buildup and eventual loss of cell function in SOFCs utilizing hydrocarbon fuels, or direct conversion in SOFCs using solid carbon fuel sources, reaction pathways for carbon electrochemical oxidation are necessary to develop stable and optimized anodes.

5 Thermochemistry in SOFC anodes

Typical operating temperatures of SOFCs are high enough that homogeneous gas-phase chemistry within the anode and fuel channel should be considered with hydrocarbon fuels. Moreover, because the most common anode metal is nickel, there are abundant nickel catalysts to promote thermochemical reactions via heterogeneous chemistry. It is well known that nickel is an efficient catalyst for hydrocarbon cracking, and is highly susceptible to carbon deposition sometimes leading to the growth of carbon nanofibers (or whiskers), which separate the Ni particle from the YSZ.[31,119,120] Both homogeneous and heterogeneous chemistry play key roles in reforming the hydrocarbon fuel into a hydrogen- and CO-rich fuel. Inside the porous anode, homogeneous chemistry is sometimes ignored based on the argument that homogeneous reactions of methane with H_2O and CO_2 are very slow at 800°C or lower.[40,48] However, for higher hydrocarbon fuels, higher temperatures, or partial oxidation conditions, homogeneous reactions are important for controlling the relative composition of gas-phase species. In principle, the majority of the anode channel is exposed to the interconnect material, and only a fraction is exposed to the anode material containing Ni catalysts. Therefore, homogeneous chemistry is of greater importance and cannot be ignored in the channel (*i.e.*, where oxidation products like H_2O and CO_2 combine with and reform the fuel as it moves downstream).[121,122]

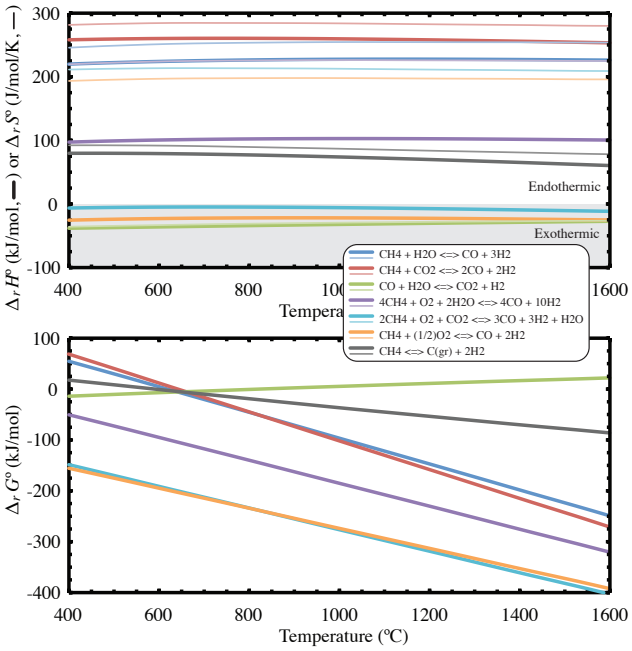

Fig. 15 Plot of the reaction enthalpies (top panel, thick lines), entropies (top panel, thin lines), and Gibbs free energy change (bottom panel) for the reforming reactions and water-gas shift (WGS) as a function of temperature.

5.1 Reforming and shifting reactions

There are various alternatives for the reformation of hydrocarbons, including steam reforming, dry reforming, partial oxidation, autothermal reforming, and thermal decomposition. In the context of SOFCs, the reforming of hydrocarbon fuels may, in general, take place externally in a separate process, or internally inside the hot stack. Each of the aforementioned global reforming processes is briefly discussed below. The reader is referred to Ref. 6 for a comprehensive discussion of and performance predictions of an SOFC using syngas derived from partial oxidation (CPOx) or steam reforming of methane and dodecane, and gasification of coal or biomass.

A thermodynamic summary of each of the reactions is provided graphically in Fig. 15. These reforming reactions proceed through homogeneous and heterogeneous elementary thermochemical reaction steps. Homogeneous elementary chemistry is well developed in the combustion literature, and Hecht *et al.*[40] recently proposed an elementary heterogeneous reaction mechanism for CH_4 on Ni-based catalysts. The reaction mechanism consists of 42 irreversible reactions among 6 gas-phase and 12 surface-adsorbed species. The full mechanism covers the global aspects of steam reforming, dry reforming, the water-gas shift (forward and reverse), and carbon deposition. This mechanism was adopted by Zhu *et al.*[48] and later improved by Janardhanan and Deutschmann.[41] The full mechanism with reaction-rate constants is detailed in Table 8. For steam reforming on nickel-based catalysts, the elementary reaction steps can be summarized according to:[7]

- CH_4 adsorption and dehydrogenation to form the chemisorbed surface species CH_3(Ni), CH_2(Ni), CH(Ni), and C(Ni);
- H_2O adsorption and dissociation to form the surface species OH(Ni), H(Ni), and O(Ni);
- formation of the intermediate surface species CH_xO(Ni), which are related to the formation of the precursors of CO and CO_2;
- coke formation due to CH_4 thermal cracking and Boudouard reaction;
- carbon gasification by CO_2, H_2, and steam.

5.1.1 Steam reforming. Steam reforming (SR), sometimes called steam-methane reforming (SMR), is a process in which high-temperature steam is used to produce a mixture of hydrogen and CO (*i.e.*, syngas) from methane, ethanol, propane, or even gasoline. The lighter hydrocarbons react with hot water vapor in the presence of a catalyst to produce

Table 8 Heterogeneous reaction mechanism for CH_4 reforming on Ni-based catalysts [a]

	Reaction	A [b]	n	E [b]
1	$H_2 + (Ni) + (Ni) \rightarrow H(Ni) + H(Ni)$	1.000×10^{-2} [c]	0.0	0.0
2	$H(Ni) + H(Ni) \rightarrow (Ni) + (Ni) + H_2$	$2.545 \times 10^{+19}$	0.0	81.2
3	$O_2 + (Ni) + (Ni) \rightarrow O(Ni) + O(Ni)$	1.000×10^{-2} [c]	0.0	0.0
4	$O(Ni) + O(Ni) \rightarrow (Ni) + (Ni) + O_2$	$4.283 \times 10^{+23}$	0.0	474.9
5	$CH_4 + (Ni) \rightarrow CH_4(Ni)$	8.000×10^{-3} [c]	0.0	0.0
6	$CH_4(Ni) \rightarrow (Ni) + CH_4$	$8.705 \times 10^{+15}$	0.0	37.5
7	$H_2O + (Ni) \rightarrow H_2O(Ni)$	1.000×10^{-1} [c]	0.0	0.0
8	$H_2O(Ni) \rightarrow (Ni) + H_2O$	$3.732 \times 10^{+12}$	0.0	60.8
9	$CO_2 + (Ni) \rightarrow CO_2(Ni)$	1.000×10^{-5} [c]	0.0	0.0
10	$CO_2(Ni) \rightarrow (Ni) + CO_2$	$6.447 \times 10^{+7}$	0.0	26.0
11	$CO + (Ni) \rightarrow CO(Ni)$	5.000×10^{-1} [c]	0.0	0.0
12	$CO(Ni) \rightarrow (Ni) + CO$	$3.563 \times 10^{+11}$	0.0	111.3
		ε_{CO}		-50.0 [d]
13	$O(Ni) + H(Ni) \rightarrow OH(Ni) + (Ni)$	$5.000 \times 10^{+22}$	0.0	97.9
14	$OH(Ni) + (Ni) \rightarrow O(Ni) + H(Ni)$	$1.781 \times 10^{+21}$	0.0	36.1
15	$OH(Ni) + H(Ni) \rightarrow H_2O(Ni) + (Ni)$	$3.000 \times 10^{+20}$	0.0	42.7
16	$H_2O(Ni) + (Ni) \rightarrow OH(Ni) + H(Ni)$	$2.271 \times 10^{+21}$	0.0	91.8
17	$OH(Ni) + OH(Ni) \rightarrow O(Ni) + H_2O(Ni)$	$3.000 \times 10^{+21}$	0.0	100.0
18	$O(Ni) + H_2O(Ni) \rightarrow OH(Ni) + OH(Ni)$	$6.373 \times 10^{+23}$	0.0	210.9
19	$O(Ni) + C(Ni) \rightarrow CO(Ni) + (Ni)$	$5.200 \times 10^{+23}$	0.0	148.1
20	$CO(Ni) + (Ni) \rightarrow O(Ni) + C(Ni)$	$1.354 \times 10^{+22}$	-3.0	116.1
		ε_{CO}		-50.0 [d]
21	$O(Ni) + CO(Ni) \rightarrow CO_2(Ni) + (Ni)$	$2.000 \times 10^{+19}$	0.0	123.6
		ε_{CO}		-50.0 [d]
22	$CO_2(Ni) + (Ni) \rightarrow O(Ni) + CO(Ni)$	$4.653 \times 10^{+23}$	-1.0	89.3
23	$HCO(Ni) + (Ni) \rightarrow CO(Ni) + H(Ni)$	$3.700 \times 10^{+21}$	0.0	0.0
		ε_{CO}		50.0 [d]
24	$CO(Ni) + H(Ni) \rightarrow HCO(Ni) + (Ni)$	$4.019 \times 10^{+20}$	-1.0	132.2
25	$HCO(Ni) + (Ni) \rightarrow O(Ni) + CH(Ni)$	$3.700 \times 10^{+24}$	-3.0	95.8
26	$O(Ni) + CH(Ni) \rightarrow HCO(Ni) + (Ni)$	$4.604 \times 10^{+20}$	0.0	110.0
27	$CH_4(Ni) + (Ni) \rightarrow CH_3(Ni) + H(Ni)$	$3.700 \times 10^{+21}$	0.0	57.7
28	$CH_3(Ni) + H(Ni) \rightarrow CH_4(Ni) + (Ni)$	$6.034 \times 10^{+21}$	0.0	61.6
29	$CH_3(Ni) + (Ni) \rightarrow CH_2(Ni) + H(Ni)$	$3.700 \times 10^{+24}$	0.0	100.0
30	$CH_2(Ni) + H(Ni) \rightarrow CH_3(Ni) + (Ni)$	$1.293 \times 10^{+23}$	0.0	55.3
31	$CH_2(Ni) + (Ni) \rightarrow CH(Ni) + H(Ni)$	$3.700 \times 10^{+24}$	0.0	97.1
32	$CH(Ni) + H(Ni) \rightarrow CH_2(Ni) + (Ni)$	$4.089 \times 10^{+24}$	0.0	79.2
33	$CH(Ni) + (Ni) \rightarrow C(Ni) + H(Ni)$	$3.700 \times 10^{+21}$	0.0	18.8
34	$C(Ni) + H(Ni) \rightarrow CH(Ni) + (Ni)$	$4.562 \times 10^{+22}$	0.0	161.1
35	$O(Ni) + CH_4(Ni) \rightarrow CH_3(Ni) + OH(Ni)$	$1.700 \times 10^{+24}$	0.0	88.3
36	$CH_3(Ni) + OH(Ni) \rightarrow O(Ni) + CH_4(Ni)$	$9.876 \times 10^{+22}$	0.0	30.4
37	$O(Ni) + CH_3(Ni) \rightarrow CH_2(Ni) + OH(Ni)$	$3.700 \times 10^{+24}$	0.0	130.1
38	$CH_2(Ni) + OH(Ni) \rightarrow O(Ni) + CH_3(Ni)$	$4.607 \times 10^{+21}$	0.0	23.6
39	$O(Ni) + CH_2(Ni) \rightarrow CH(Ni) + OH(Ni)$	$3.700 \times 10^{+24}$	0.0	126.8
40	$CH(Ni) + OH(Ni) \rightarrow O(Ni) + CH_2(Ni)$	$1.457 \times 10^{+23}$	0.0	47.1
41	$O(Ni) + CH(Ni) \rightarrow C(Ni) + OH(Ni)$	$3.700 \times 10^{+21}$	0.0	48.1
42	$C(Ni) + OH(Ni) \rightarrow O(Ni) + CH(Ni)$	$1.625 \times 10^{+21}$	0.0	128.6

[a] Based on Ref. 41, this mechanism can be downloaded from www.detchem.com.

[b] Arrhenius parameters for the rate constants written in the form: $k = AT^n \exp(-E/RT)$. The units of A are given in terms of moles, centimeters, and seconds. E is in kJ/mol.

[c] Sticking coefficient

[d] Coverage-dependent activation energy appearing in $k = AT^n \exp(-E/RT) \exp(-\varepsilon_{CO}\theta_{CO}/RT)$. The total available surface site density is $\Gamma = 2.66 \times 10^{-9}$ mol/cm^2. ε_{CO} is in kJ/mol.

hydrogen, carbon monoxide, and a relatively small amount of carbon dioxide. Steam reforming is extremely endothermic, and therefore requires an external source of heat but can sometimes utilize recycled heat from exothermic processes depending on system configuration. The reforming process is generally followed by the water-gas shift (WGS) reaction (mildly exothermic), where the carbon monoxide can further react with steam to produce more hydrogen. The SR and WGS reactions are, respectively,

$$\mathrm{C}_x\mathrm{H}_y + x\mathrm{H_2O} \rightleftharpoons x\mathrm{CO} + \left(x + \frac{y}{2}\right)\mathrm{H_2}$$
$$(\Delta_r^{\mathrm{CH_4}} H^\circ_{25^\circ\mathrm{C}} = 206.2 \text{ kJ/mol},\ \Delta_r^{\mathrm{CH_4}} H^\circ_{1000^\circ\mathrm{C}} = 227.5 \text{ kJ/mol})$$

$$\mathrm{CO} + \mathrm{H_2O} \rightleftharpoons \mathrm{CO_2} + \mathrm{H_2}$$
$$(\Delta_r H^\circ_{25^\circ\mathrm{C}} = -41.2 \text{ kJ/mol},\ \Delta_r H^\circ_{1000^\circ\mathrm{C}} = -32.1 \text{ kJ/mol})$$

5.1.2 Dry reforming. It is well known that CO_2 can behave as an oxidant for hydrocarbons in the presence of a suitable catalyst, so-called dry reforming or carbon dioxide reforming. Carbon deposition is a particular concern with dry reforming, especially with Ni-based catalysts. Dry reforming is also a strongly endothermic reaction, but it provides a use for sequestered CO_2 to produce useful syngas mixtures. For a general hydrocarbon, the dry-reforming reaction is

$$\mathrm{C}_x\mathrm{H}_y + x\mathrm{CO_2} \rightleftharpoons 2x\mathrm{CO} + \frac{y}{2}\mathrm{H_2}$$
$$(\Delta_r^{\mathrm{CH_4}} H^\circ_{25^\circ\mathrm{C}} = 247.3 \text{ kJ/mol},\ \Delta_r^{\mathrm{CH_4}} H^\circ_{1000^\circ\mathrm{C}} = 259.6 \text{ kJ/mol})$$

5.1.3 Partial oxidation. Partial oxidation (POx) is a chemical reaction between the hydrocarbon and oxygen (generally from air because of its convenience and cost) in a substoichiometric ratio, hence the name "partial oxidation." It is an exothermic process, and typically has lower efficiency than other reforming methods because of energy loss in oxidizing the hydrocarbon. Because there is not a need for an external heat source, POx is characterized by a much faster startup time than steam reformers. Catalytic partial oxidation (CPOx) reduces the required reforming temperature from around 1200°C to 800–900°C through the use of a catalyst (*e.g.*, nickel). Catalyst selection and stability can be an issue for high-sulfur-containing fuels. The CPOx reaction is weakly exothermic, eliminating the need for external thermal inputs. Partial oxidation is characterized by the general reaction

$$\mathrm{C}_x\mathrm{H}_y + \frac{x}{2}\mathrm{O_2} \rightleftharpoons x\mathrm{CO} + \frac{y}{2}\mathrm{H_2}$$
$$(\Delta_r^{\mathrm{CH_4}} H^\circ_{25^\circ\mathrm{C}} = -35.7 \text{ kJ/mol},\ \Delta_r^{\mathrm{CH_4}} H^\circ_{1000^\circ\mathrm{C}} = -21.9 \text{ kJ/mol})$$

5.1.4 Autothermal reforming. Autothermal reforming (ATR) can be thought of as a combination of POx and steam reforming (or dry reforming) as it uses oxygen and steam (or carbon dioxide) in a reaction with methane, for example, to form syngas. It has merits from both processes in that ATR is more flexible than SR with respect to startup time and has higher efficiency than POx. The heat produced by the partial oxidation reaction is used in the reforming reaction. The reactions below are for ATR of methane—when steam is used, the resulting syngas is a mixture of H_2:CO=5:2, whereas when carbon dioxide is used, the syngas mixture has a ratio H_2:CO=1:1.

$$4\mathrm{CH_4} + \mathrm{O_2} + 2\mathrm{H_2O} \rightleftharpoons 4\mathrm{CO} + 10\mathrm{H_2}$$
$$(\Delta_r H^\circ_{25^\circ\mathrm{C}} = 85.3 \text{ kJ/mol},\ \Delta_r H^\circ_{1000^\circ\mathrm{C}} = 102.8 \text{ kJ/mol})$$

$$2\mathrm{CH_4} + \mathrm{O_2} + \mathrm{CO_2} \rightleftharpoons 3\mathrm{CO} + 3\mathrm{H_2} + \mathrm{H_2O}$$
$$(\Delta_r H^\circ_{25^\circ\mathrm{C}} = -15.1 \text{ kJ/mol},\ \Delta_r H^\circ_{1000^\circ\mathrm{C}} = -5.81 \text{ kJ/mol})$$

5.1.5 Thermal decomposition. Thermal decomposition is a chemical decomposition of the hydrocarbon that requires heat to break the chemical bonds. High purity hydrogen can be obtained from such processes, but removal of fuel impurities (*e.g.*, sulfur) and solid carbon will be an issue in SOFCs. Thermal decomposition of methane proceeds by the reaction

$$\mathrm{CH_4} \rightleftharpoons \mathrm{C} + 2\mathrm{H_2}$$
$$(\Delta_r^{\mathrm{C(gr)}} H^\circ_{25^\circ\mathrm{C}} = 74.9 \text{ kJ/mol},\ \Delta_r^{\mathrm{C(gr)}} H^\circ_{1000^\circ\mathrm{C}} = 73.9 \text{ kJ/mol})$$

5.2 Carbon deposition

A significant concern during reforming processes is the formation of solid carbon through undesired side reactions. Amongst other deleterious effects, solid carbon formed in the anode can block the pores and increase transport resistance for gas species trying to reach the TPB, and/or prevent reforming reactions by covering the catalyst particles. At typical SOFC operating temperatures with hydrocarbon or syngas fuels, the extent of carbon formation depends on factors such as the steam/carbon ratio, operating conditions (*e.g.*, temperature, pressure, current density), and anode catalyst. Although it is possible to minimize carbon deposition on traditional Ni-YSZ anodes by providing sufficient H_2O in the fuel stream, the amounts required are generally excessive, diluting the fuel and reducing overall efficiency, in addition to creating device- and systems-scale complexity because of the need for water management solutions. In this light, analysis of carbon deposition in the SOFC anode—including the deposition and growth mechanisms, and material tolerances—is absolutely necessary if SOFCs are to be a viable and economical option for efficiently utilizing carbon-containing fuels.

5.2.1 Deposition and growth mechanisms. There are two primary mechanisms for carbon formation in SOFC anodes: (*i*) heterogeneously formed carbon nanowires or

Table 9 Different pathways for carbon deposition (adapted from Ref. 123)

	Fibrous carbon	Encapsulating polymers	Pyrolytic carbon
Formation pathway	• Heterogeneous chemistry on a metal (*e.g.*, Ni) catalyst • Diffusion of C through the Ni lattice • Nucleation and whisker growth from below the Ni particle, eventually separating the particle from the electrolyte (see Fig. 16)	• Heterogeneous chemistry on a metal (*e.g.*, Ni) catalyst • Slow polymerization of C_nH_m radicals on the Ni surface, eventually forming an encapsulating film	• Homogeneous gas-phase chemistry • Thermal cracking of hydrocarbon • Deposition of C precursors on catalyst
Effects	• No deactivation of Ni surface • Breakdown of catalyst and increasing pressure drop	• Progressive deactivation	• Encapsulation of catalyst particle • Deactivation and increasing pressure drop
Temperature	$>\sim 450^\circ$C(~ 720 K)	$<\sim 500^\circ$C(~ 770 K)	$>\sim 600^\circ$C(~ 870 K)
Critical parameters	• High temperature • Low H_2O:C_nH_m ratio • Low activity • Aromatic feed • No enhanced H_2O adsorption	• Low temperature • Low H_2O:C_nH_m ratio • Low H_2:C_nH_m ratio • Aromatic feed	• High temperature • High void fraction • Low H_2O:C_nH_m ratio • High pressure • Activity of catalyst

nanofibers that grow on the catalyst;[124,125] and (*ii*) homogeneously formed soot that can deposit anywhere in the anode.[126–128] The soot, or pyrolytic carbon, can encapsulate and deactivate catalyst particles. For each of these mechanisms, the formation characteristics and resulting impact on the anode (and therefore, the cell behavior) are summarized in Table 9.

Encapsulating carbon is known to form by slow polymerization of C_nH_m radicals on the Ni surface, most often at temperatures lower than 500°C. Because the operating temperatures of SOFCs are typically well above this, it is not of much concern. However, growth of carbon nanofibers and soot formation are prevalent at elevated temperatures in the range of SOFC operation, and the mechanisms governing their formation have been well investigated. Pyrolytic carbon has been studied extensively in combustion science,[126,127] and can be formed in the absence of a catalyst via gas-phase condensation reactions.[128] Simple hydrocarbon fuels react to form a polyaromatic hydrocarbon (PAH) via abstraction, beta-scission, and addition/recombination. These PAHs are regarded as precursors of carbon deposition or soot formation. The deposition propensity is predicted by the sum of mole fractions of all species containing five or more carbon atoms.[122,128] Alternatively, the formation of carbon fibers involves a dissolution and diffusion of carbon atoms into the metal catalyst (where the source of carbon originates from dissociation of hydrocarbons over the catalyst), followed by precipitation of carbon atoms as a graphite fiber on the surface.[125] The formation of carbon fibers can result in removal of Ni particles from the electrode—a process that occurs when the nickel catalyst is physically lifted from the electrode by its attachment to the growing carbon fiber (see Fig. 16 and Ref. 124)—and can eventually cause the electrode to fracture because of the mechanical stresses induced by many growing fibers.[129]

The propensity for solid carbon formation has also been examined using equilibrium thermodynamic calculations.[35,121,130] Most thermodynamic analyses use thermochemical properties of graphite to represent the carbon phase because these values are readily available. However, assuming graphitic carbon may not be appropriate for predicting the onset of carbon deposition.[125] There is evidence, for example, in which carbon deposition has not been observed experimentally although thermodynamic equilibrium calculations using properties of graphite predict its formation. In contrast, there are reports of carbon formation under conditions where it is predicted to be thermodynamically unfavorable.[125] The predictive failures may result from a lack of thermodynamic information for activation barriers relating to the carbon growth mechanism (*e.g.*, the deposition and growth of hollow carbon tubes would certainly have a different activation energy than a solid fiber, and even more so than a deposited carbon film). Because the growth mechanism depends on operating conditions and catalyst type, the contribution of chemical kinetics, which has similar dependencies, is also likely important.

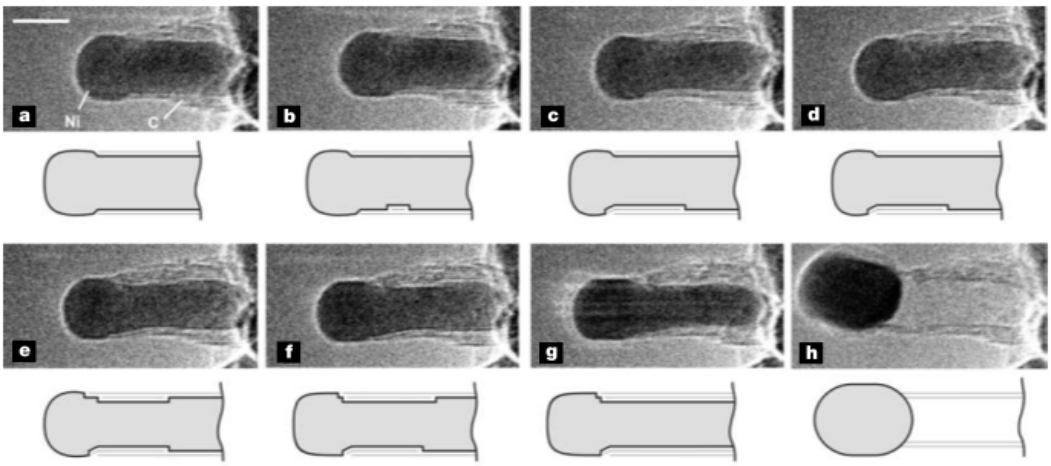

Fig. 16 Image sequence of a growing carbon nanofiber from methane decomposition over supported nickel nanocrystals. Panels a–h illustrate the elongation/contraction process. Drawings are included to guide the eye in locating the positions of mono-atomic Ni step edges at the C/Ni interface. The images are acquired in situ with CH_4:H_2=1:1 at a total pressure of 2.1 mbar with the sample heated to 536°C. All images are obtained with a rate of 2 frames per second. Scale bar (seen in panel a), 5 nm. Image and description from Ref. 124.

5.2.2 Coking resistant anode materials. Although carbon formation on Ni can be suppressed and sometimes avoided altogether if there is sufficient steam to remove carbon faster than it deposits, using SOFCs as a viable and promising technology with non-hydrogen fuels requires better suited anode materials. The SOFC community has given cerium oxide much attention in recent years because of its excellent oxidation catalysis effects for CO and hydrocarbons.[131] In addition, its mixed-ionic-electronic conducting ability in a reducing atmosphere has also attracted interest,[18] making ceria an ideal catalyst in SOFC anodes for hydrocarbon-fuel applications.

A composite anode consisting of Cu-CeO_2-YSZ/SDC has been used to demonstrate the significant performance enhancement (compared to a Cu-YSZ/SDC cell) of a cell operating on hydrocarbon fuels, and therefore, the promise of using ceria.[18,25,38,105,132] Copper is not catalytically active for carbon deposition, but it is effective as a current collector. Because of the lower catalytic activity, Cu-based anodes typically display larger activation polarizations compared to Ni-based counterparts. Further, fabrication procedures for Ni-based anodes are not suitable for Cu-based cermets because the melting point of Cu is lower than Ni. Ceria provides high catalytic activity for hydrocarbon reforming due to its oxygen storage and transport properties.

McIntosh *et al.*[133] examined the changes that occur in hydrocarbon SOFC performance by replacing nickel-based cermets with composites containing Cu and ceria. They reported direct, electrochemical oxidation of various hydrocarbons (methane, ethane, 1-butene, *n*-butane and toluene) at 700°C and 800°C. Ye *et al.*[134] explored the performance of a Cu-CeO_2-ScSZ (scandia-stabilized zirconia) composite anode for a SOFC operating on ethanol fuel. The anode exhibited stable performance for a fuel stream of ethanol and water, without any visible carbon deposition after 50 h.

Instead of complete substitution of nickel with copper, some attention has been given to Cu-Ni alloys to improve the compatibility of Cu-based anodes. Kim *et al.*[129] tested a range of Cu-Ni alloys (with Ni compositions of 0, 10, 20, 50, and 100%) at 800°C with dry CH_4 as fuel. The performance of a cell made with Cu(80%)-Ni(20%) showed a significant increase in power density with time for 500 h of operation. This observation is attributed to an increase in electronic conductivity in the anode due to small carbon deposits, which likely increase connectivity of electronic conduction pathways without being severe enough to have a deleterious effect. Lee *et al.*[135] examined the performance of anodes containing mixtures of Cu and Ni or Cu and Co operated with H_2 and *n*-butane fuels at 700°C and 800°C. The bimetallic anodes exhibited improved performance in H_2 at 700°C compared to Cu-based anodes, and were less susceptible to carbon formation in *n*-butane compared to Ni- or Co-based anodes. Xie *et al.*[136] also researched the performance of metal-alloyed cermet anodes. A tri-metallic alloy of Fe-Co-Ni-SDC was used as the cermet anode (in compositions of $Fe_xCo_{0.5-x}Ni_{0.5}$ with $x = 0.1, 0.2, 0.25, 0.3, 0.4$), with a GDC electrolyte, and $Sm_{0.5}Sr_{0.5}CoO_3$-SDC (SSC-SDC) cathode. With $x = 0.25$, the cells showed the lowest interfacial resistance (*e.g.*, 0.11 Ω cm^2 at 600°C with H_2 and 3% H_2O) and highest power density (*e.g.*, 0.75 W/cm^2 at 600°C with H_2 and 3% H_2O).

Similar work has shown that anode performance can be improved by adding noble metals (*e.g.*, Pt, Rh, Pd, or Ru),

which effectively promote hydrocarbon reforming reactions. Costa-Nunes *et al.*[137] reported that the addition of 1 wt.% Pt into the Cu-CeO_2-based anode greatly improved the performance of a SOFC operating on hydrocarbon fuels. Hibino *et al.*[37,138] used a Ru-Ni-GDC anode and a thin ceria-based electrolyte-film hydrocarbon-fueld SOFC. The Ru catalyst was shown to effectively promote hydrocarbon reforming and the cell achieved a peak power density of 0.75 W/cm^2 with dry methane, which is comparable to 0.769 W/cm^2 with humidified (2.9 vol.% H_2O) hydrogen. Zhan *et al.*[26,39] used a conventional anode with a Ru-CeO_2 catalyst layer to internally reform iso-octane without coking.

Other metals have also been used to decrease carbon deposition on a catalyst. A small amount of gold present in a Ni-based catalyst has been shown to significantly reduce carbon deposits during steam reforming of methane,[139] most likely due to inhibition of methane dissociation by Au.[140,141] For example, Gavrielatos *et al.*[142] tested an Au-modified Ni-YSZ anode (1% Au with respect to Ni) in methane-rich steam reforming conditions, and found the electrode to be highly tolerant to carbon deposits, even at methane-to-water ratios as high as 3, at temperatures in the range 700–900°C.

Perovskites are also commonly used as anode materials, which are metal-oxide compounds with the general formula ABO_3. Cations A and B are able to combine more than two metal ions.[1] Perovskite oxides containing transition metals at B sites have been proven to be effective catalysts not only for electrochemical reduction of oxygen, but also for the combustion of light hydrocarbons (*e.g.*, CH_4, C_2H_6).[143,144] Hydrocarbon oxidation over perovskite oxides is thought to proceed by both suprafacial and intrafacial reactions.[145] The suprafacial reactions take place between the adsorbed species on the surface at relatively low temperatures, and the reaction rates appear to be correlated primarily with the electronic configurations of the surface transition-metal ions. The intrafacial reactions typically occur at high temperatures, with rates that are greatly dependent on the thermodynamic stability of oxygen vacancies adjacent to the transition-metal ion.

Studies have reported that LSCF exhibits good catalytic activity for direct CH_4 oxidation and is less susceptible to deactivation through carbon deposition than conventional Ni-YSZ anode catalysts. Electrochemical oxidation of methane on LSCF catalysts used in a SOFC anode environment is thought to occur via:[146] (1) CH_4 decomposition; (2) electrochemical oxidation of hydrogen species to H_2O; and (3) electrochemical oxidation of CO to O_2. The formation of CO_2 and CO takes place in a parallel pathway (*i.e.*, $C+2O^{2-} \rightleftharpoons CO_2+4e^-$, $C+O^{2-} \rightleftharpoons CO+2e^-$), where the intrinsic rate constant for the formation of CO_2 is greater than that of CO.

Despite the attention given to perovskite materials for applications as anodes in hydrocarbon-fueled SOFCs,[147–157] their performance is still less favorable compared to Ni-YSZ cermet anodes. Aside from relatively low electrochemical activities, other issues must be addressed if perovskites are to be used in SOFC anodes,[1–3] including relatively low stability in a reducing environment, and relatively low electronic conductivity compared with metal catalysts.

5.3 H_2S poisoning and oxidation

5.3.1 H_2S poisoning. Most available hydrocarbon fuels contain some amount of sulfur, which is a poison for nickel steam-reforming catalysts and for many anode catalysts including platinum. The adsorption of sulfur on nickel is reversible at low concentrations. However, at high concentrations, bulk sulfidation occurs causing permanent damage to the catalyst. The sensitivity of nickel to sulfur poisoning decreases with increasing temperature, so SOFCs are able to tolerate higher concentrations of sulfur in the fuel feed than other lower-temperature fuel cells. In general, the concentration of sulfur in the fuel needs to be reduced to 0.2 ppm or lower. Sulfur is mainly found in the form of hydrogen sulfide because organic sulfur compounds, usually included as an odorant, reform to H_2S during desulfurization. The existence of H_2S in the fuel gas decreases the anode electrochemical activity as a result of contamination of reaction sites by sulfur adsorption on the Ni catalyst surface. Outside of the anode, sulfur species can be equally deleterious because H_2S is a highly corrosive gas and its existence can lead to corrosion of other cell components.

To eliminate the need for desulfurization units in natural-gas- or coal-syngas-fueled SOFC systems, developing anode materials with high sulfur tolerance is absolutely crucial. Without having to expend energy to clean the fuel of sulfur, the overall system efficiency can be improved, and system cost and complexity can be reduced. Even small efficiency improvements and reductions in cost can have a big impact on overall cost per kW—the DOE target for SOFCs to be commercially viable is $400/kW—because both the numerator and denominator are contributing to a reduced ratio.

Experiments designed to study the effects of H_2S on the performance of a Ni-YSZ anode show the onset of performance degradation for H_2S concentrations of 0.05, 0.5, and 2 ppm at operating temperatures of 750°C, 900°C, and 1000°C, respectively.[158,159] That is, the cell was able to withstand higher concentrations of H_2S at higher temperatures before decreases in performance were observed. Losses in performance were shown to be recoverable if the sulfur was removed, with better recovery at lower temperature. The degradation phenomenon has been identified and confirmed by others, but the mechanism causing deterioration has yet to be identified. Because of the ability to recover performance—sometimes up to 90% recovery—it is presumed that the strong adsorption of sulfur or H_2S on active sites in the Ni-YSZ anode blocks these

sites from being electrochemically active[160] (*i.e.*, there are less available sites for H_2 species to adsorb, dissociate, and participate in charge transfer). Irreversibilities, on the other hand, are suggested to be the result of NiS formation.[159] Studies of nickel-sulfide interactions by Raman spectroscopy at high temperatures indicate that NiS is the prevalent species at SOFC operating conditions.

Various H_2S-tolerant materials have been studied. A Ni-GDC anode operating for more than 500 h (at 850°C and 0.2 A/cm^2) on simulated coal syngas with up to 240 ppm H_2S had a degradation of 10–12.5% (measured as a decrease in power density compared to the same cell without H_2S).[161] Cheng *et al.*[162,163] analyzed the stability of various perovskites—such as transition-metal carbides, borides, nitrides, and silicides—for tolerance to sulfur in a SOFC anode environment using thermodynamic principles. Estimation of the thermochemical data for oxides with perovskite structure provides valuable predictions about the stability of those materials. Mukundan *et al.*[164] tested several perovskites and found that a $Sr_{0.6}La_{0.4}TiO_3$-YSZ (50-50 wt.%) anode showed no degradation in the presence of up to 5000 ppm of H_2S in a hydrogen fuel. That same anode was able to operate for 8 h with 1% H_2S as a fuel and showed no degradation when the fuel was switched back to hydrogen.

Although a selection of anode materials have potential as candidates when operating with sulfur-containing fuels, other issues remain. For example, the anode must not only tolerate sulfur contaminants while continuing to promote charge-transfer reactions, but it must withstand other impurities that will most certainly be found in coal syngas from coal gasification. Research in areas of material tolerance to contaminants must continue to find effective catalysts in coal-syngas-fueled SOFCs.

5.3.2 H_2S as a fuel, rather than pollutant. Despite the observed performance drop potentially caused by the blockage of surface reactive sites by sulfur species, the cell still has the ability to electrochemically oxidize H_2S,[165–168] which demonstrates the possibility of using it as a fuel.

In a SOFC, oxide ions in the solid-oxide electrolyte can react with H_2S in the anode according to the charge-transfer reactions

$$H_2S + O^{2-} \rightleftharpoons H_2O + \frac{1}{2}S_2 + 2e^- \quad (E_{rev} = 1.066 \text{ V at } 800^\circ\text{C})$$

$$H_2S + 3O^{2-} \rightleftharpoons H_2O + SO_2 + 6e^- \quad (E_{rev} = 0.856 \text{ V at } 800^\circ\text{C})$$

where the reversible Nernst potentials are calculated for a global redox reaction relative to air, and assuming an equilibrated mixture of 98% H_2S and 2% products in equal mole amounts. Note also that the OCVs for the global redox reactions have different dependencies on temperature; the top anodic half-cell reaction yields an OCV that increases with increasing temperature, whereas the OCV associated with the lower half-cell reaction decreases with increasing temperature. In addition to multiple oxidation pathways, the dominant mechanism may also involve thermal decomposition of H_2S on the anode (given by $H_2S \rightleftharpoons H_2 + (1/2)S_2$), as well as reactions between H_2S and SO_2 (*e.g.*, $2H_2S + SO_2 \rightleftharpoons 2H_2O + (3/n)S_n$). To complicate things even further, sulfur species generated in the oxidation reactions can participate in charge transfer as well, *e.g.*,

$$S + 2O^{2-} \rightleftharpoons SO_2 + 4e^-$$

$$S_2 + 4O^{2-} \rightleftharpoons 2SO_2 + 8e^-$$

Anode catalysts comprised of composite metal sulfides derived from mixtures of Mo and other transition metals (e.g, Fe, Co, Ni) have been shown to be stable and effective for conversion of H_2S in SOFCs, with Co-Mo-S admixed with up to 10% Ag exhibiting superior activity and longevity.[167] Other reports in the literature confirm the performance of metal sulfides as viable anode materials for carbon- and sulfur-resistant SOFCs.[165]

There is a general lack of knowledge regarding the oxidation mechanism for H_2S, which is certain to be catalyst-dependent. Monder *et al.*[166] developed a hierarchy of models to describe the performance of a single H_2S-fueled SOFC button cell used previously in experiments.[167] The model objectives were to estimate kinetic parameters associated with electrochemical reactions coupled with mass transfer. The models range in complexity from an algebraic system of equations used to calculate activation, concentration, and ohmic losses, to a physics-based two-dimensional finite-element model. However, comprehensive validation of the models and predicted parameters is still needed. Future work should target detailed electrochemical studies of the electrodes to investigate the fundamental reaction mechanisms, with multi-step elementary reactions including competitive adsorption and desorption of reaction species.

6 Concluding remarks

The high fuel flexibility of solid-oxide fuel cells (SOFCs) makes it possible to use relatively cheap, safe, and readily available hydrocarbon or coal syngas fuels, thereby increasing the feasibility of near-term SOFC commercialization for cleaner and more efficient conversion of these fuels to generate power. In the first part of this paper, the basic operating principles and performance of SOFCs with different fuels were summarized. Results from a wide range of studies indicate that SOFCs have unmatched potential for replacing much dirtier, less efficient combustion systems while operating on the same raw fuel sources. However, most of these results are reported for laboratory- or device-scale experiments and

there are still a set of challenges to overcome before single-cell experiments are scaled up to large stacks and integrated with other components of a power generation system.

Ni-yttria-stabilized zirconia (Ni-YSZ) cermets and slight variations thereof are currently the most common anode material for SOFC applications. The electrochemical reaction mechanisms and transport processes of hydrocarbon and syngas fuels within Ni-YSZ anodes is extremely complex, especially when additional consideration must be given to complications of carbon deposition and sulfur poisoning. In the second part of this paper, we have summarized several possible reaction mechanisms appearing in the literature for the electrochemical oxidation of H_2, CO, CH_4, and solid carbon, as well as other hydrocarbons. Even for the simplest and most studied fuel H_2, there is still not a clear and concise conclusion on the oxidation mechanism, charge-transfer, or rate-determining kinetics, especially under different operating conditions. For all the fuels considered in this paper, more carefully designed experimental studies and elementary reaction models are needed to elucidate the reaction mechanisms and kinetic parameters (at different operating conditions and on different relevant catalysts). It is important to distinguish between the different reaction pathways (especially for hydrocarbon fuels) because the demands on the anode material differ significantly for these pathways.

A significant concern during SOFC operation with hydrocarbon or syngas fuels is the formation of solid carbon through undesired side reactions. The mechanisms for solid carbon deposition are not yet known, but they will almost certainly depend on the material and the operating conditions in the cell. Although carbon formation on Ni can be suppressed or avoided with changes in operating conditions (*e.g.*, temperatures, and most notably, steam content in the fuel stream), novel anode materials or additives must be developed to extend the range of applicability of SOFCs beyond hydrogen-containing fuels (*e.g.*, dry-gasified solid carbon or pure CO). For instance, Cu-based, ceria-based, metal alloys, and perovskite materials have been shown to at least have some potential. These novel anode materials must not only be effective electrocatalysts without being susceptible to coking, but they must also tolerate pollutants in the fuel stream that could diminish SOFC performance. The existence of H_2S in the fuel gas can decrease anode electrochemical activity due to contamination of reactions sites by sulfur adsorption on the Ni catalyst surface. The effects of sulfur in the fuel (some positive, most negative) were also reviewed in this paper.

Electro- and thermochemistry are discussed in the context of SOFC-MEA modeling. The missing piece to a fairly complete model is a representation of the mass transport within the SOFC flow channel and porous electrodes. As a whole SOFC modeling is a complex and crucial component of fuel cell development. The interdependence of heterogeneous chemistry, charge-transfer processes, and transport determine the rate and ability of the cell to deliver current to an external load. This interdependence coupled with physical access limitations means it is difficult to study these processes experimentally (except with well-thought-out setups such as patterned-anode experiments), so mathematical and physical models are absolutely important to study each process and its connection to the others. Understanding the rate-limiting processes and exploring the impact of electrode microstructure on fuel cell performance are critical for optimization, and essential to move SOFC technology to the forefront of cleaner and more efficient power generation for near- and long-term solutions.

Appendix A

Discussion of current-dependent overpotentials

Concentration overpotential. For open-circuit conditions (i.e., no current flow), the species concentrations at the electrode/electrolyte interface—otherwise known as the triple- or three-phase boundary (TPB)—are the same as those at the channel/electrode interface. Denoting the partial pressure of species k in the channels as p_k, the Nernst potential E_{rev} can be written in the form:

$$E_{\text{rev}} = E^\circ + \frac{RT}{n_e F}\sum_{k=1}^{K_g}\left(\nu_{k,a} - \nu'_{k,a} + \nu_{k,c} - \nu'_{k,c}\right)\ln\left(\frac{p_k}{p_{\text{atm}}}\right) \quad \text{(A-1)}$$

where $\nu_{k,a}$ and $\nu_{k,c}$ are the stoichiometric coefficients for the anode-side (fuel) and cathode-side (oxidizer) channel reactants, and $\nu'_{k,a}$ and $\nu'_{k,c}$ the stoichiometric coefficients of the kth product species in the fuel and oxidizer channels, respectively. The number of gaseous species is K_g. The remaining variables are E° the ideal Nernst potential at standard conditions ($p_{\text{atm}} = 1$ atm), T the temperature in K, $R = 8.314$ J/mol/K the universal gas constant, and $F = 96485.34$ C/mol is Faraday's constant. The ideal Nernst potential $E^\circ = -\Delta G^\circ / n_e F$, where ΔG° is the standard-state change in Gibbs free energy associated with the global oxidation reaction. The molar species concentrations $[X_k]$ are related to the partial pressures through the ideal gas equation of state, $[X_k] = p_k/RT$.

When there is nonzero net current, there must be concentration gradients across the electrode structures. This is because gaseous reactant species must be transported from the channel through the porous electrodes to reactive sites where they are consumed, and similarly, product species must be removed. Diffusion processes are the primary transport mechanism to supply the species fluxes and are driven by concentration gradients within the electrodes. Consequently, the molar species concentrations at the TPB $[X_k]^* = p_k^*/RT$ are different from the channel concentrations (i.e., the concentrations of reactant species are higher in the channel, while product species concentrations are higher at the TPB). The Nernst potential E^*_{rev} evaluated at the TPB follows as

$$E^*_{\text{rev}} = E^\circ + \frac{RT}{n_e F}\sum_{k=1}^{K_g}\left(\nu_{k,a} - \nu'_{k,a} + \nu_{k,c} - \nu'_{k,c}\right)\ln\left(\frac{p_k^*}{p_{\text{atm}}}\right). \quad \text{(A-2)}$$

In terms of species concentrations, the potential difference associated with the concentration variation is the concentration overpotential η_{conc}:

$$\begin{aligned}\eta_{\text{conc}} &= E_{\text{rev}} - E^*_{\text{rev}} \\ &= \frac{RT}{n_e F}\sum_{k=1}^{K_g}\left(\nu_{k,a} - \nu'_{k,a} + \nu_{k,c} - \nu'_{k,c}\right)\ln\left(\frac{[X_k]}{[X_k]^*}\right). \quad \text{(A-3)}\end{aligned}$$

The concentration overpotentials for the anode and cathode may be written independently as

$$\eta_{\text{conc},a} = \frac{RT}{n_e F}\sum_{k=1}^{K_g}\left(\nu_{k,a} - \nu'_{k,a}\right)\ln\left(\frac{[X_k]}{[X_k]^*}\right), \quad \text{(A-4)}$$

$$\eta_{\text{conc},c} = \frac{RT}{n_e F}\sum_{k=1}^{K_g}\left(\nu_{k,c} - \nu'_{k,c}\right)\ln\left(\frac{[X_k]}{[X_k]^*}\right). \quad \text{(A-5)}$$

6.0.2.1 Determining the concentrations at the triple-phase boundary. To compute the concentration overpotentials, the concentrations of gas species at the TPB is required. For reactive flow in the porous electrodes, the gas-phase species concentrations must satisfy

$$\frac{\partial [X_k]}{\partial t} = A_s \dot{s}^{\sim}_{\text{gas},k} + \dot{s}_{\text{gas},k} - \nabla\cdot\mathbf{J}_k, \quad k = 1,2,...,K_g \quad \text{(A-6)}$$

where $\mathbf{J}_k$ is the net molar flux vector (units of mol/m^2/s) of species k, A_s the active catalyst area per unit electrode volume (per m), $\dot{s}^{\sim}_{\text{gas},k}$ the production rate of gas species k due to heterogeneous chemistry (mol/m^2/s), and $\dot{s}_{\text{gas},k}$ the production rate of gas species k due to homogeneous gas-phase chemistry (mol/m^3/s).

The net production rates are in general given by

$$\dot{s}_k = \sum_i \nu_{ki} q_i, \quad \text{(A-7)}$$

where q_i is the rate of reaction i and ν_{ki} is the net stoichiometric coefficient of species k in reaction i (taken to be positive for products and negative for reactants). The reaction rates are computed from mass-action kinetics,[59] with temperature-dependent rate coefficients in Arrhenius form $k_i = A_i T^{n_i}\exp(-E_i/RT)$.[48] To compute the net production rates, a multistep reaction mechanism is needed. For example, the reactions of methane on nickel-based catalysts have been extensively studied in the literature, resulting in a reaction mechanism (see Table 8) consisting of 42 irreversible reactions among 6 gas-phase and 12 adsorbed species.[40,41] The multistep heterogeneous chemistry describing the reforming of methane on nickel can be used to calculate $\dot{s}^{\sim}_{\text{gas},k}$ for each species k. This mechanism has been adopted in whole or in part in many SOFC models.[42–44,48,49,57] Likewise, a mechanism describing homogeneous gas-phase thermochemistry can be included to compute $\dot{s}_{\text{gas},k}$. Important thermochemical reactions (e.g., reforming, water-gas shift, POx) are discussed in earlier sections of this paper.

The species molar fluxes $\mathbf{J}_k$ are evaluated with a transport model[60] (e.g., Fick's laws of diffusion, dusty-gas formulations,[61] Stefan-Maxwell diffusion). Species transport in fuel cells has also been modeled using lattice-Boltzmann models[62–64] and Monte-Carlo-type simulations to predict species diffusivities.[19] Fuel cell models must accurately represent the major physical processes that affect transport in porous media, including molecular diffusion, Knudsen diffusion, surface diffusion, and viscous Darcy flow. The most comprehensive transport model is arguably the dusty-gas model (DGM),[61] which is a multicomponent transport model derived from kinetic theory. It is applicable over a full range of Knudsen numbers, from values much larger than 1 (molecule-wall collisions dominate, and Knudsen diffusion is the controlling mechanism), to values much less than 1 (molecule-molecule collisions dominate, and bulk diffusion is controlling).[48] The DGM can be written as an implicit relationship among the molar concentrations $[X_k]$, molar fluxes $\mathbf{J}_k$, concentration gradient, and pressure gradient as

$$\sum_{\ell\neq k}\frac{[X_\ell]\mathbf{J}_k - [X_k]\mathbf{J}_\ell}{[X_T]D^e_{k\ell}} + \frac{\mathbf{J}_k}{D^e_{k,\text{Kn}}} = -\nabla[X_k] - \frac{[X_k]}{D^e_{k,\text{Kn}}}\frac{B}{\mu}\nabla p, \quad \text{(A-8)}$$

for $k = 1,2,...,K_g$. Here, $[X_T] = p/RT$ is the total molar concentration, B is the permeability of the porous electrode, μ the mixture viscosity, and $D^e_{k\ell}$ and $D^e_{k,\text{Kn}}$ the effective ordinary and Knudsen diffusion coefficients, respectively. Because Knudsen diffusion is governed by molecule-wall collisions, it is highly dependent on the porous electrode microstructure, including porosity ϕ, tortuosity τ, and average pore radius r_p. The effective diffusivities can be evaluated as

$$D^e_{k\ell} = \frac{\phi}{\tau}D_{k\ell}, \qquad D^e_{k,\text{Kn}} = \frac{2}{3}r_p\frac{\phi}{\tau}\sqrt{\frac{8RT}{\pi W_k}}, \quad \text{(A-9)}$$

where W_k is the molecular weight of species k. The ordinary multicomponent binary diffusion coefficients $D_{k\ell}$ and mixture viscosity μ are determined from kinetic theory.[59] Alternatively, software packages such as Cantera[51] can be used to easily compute these.

One deficiency of the DGM is the exclusion of surface diffusion. While surface diffusion is neglected in some models because it is assumed that surface species are effectively immobile on length scales larger than an individual particle,[48,49] experiments by Williford et al.[73,88] indicate that species adsorption and surface diffusion limitations near the TPB may be the dominant phenomena giving rise to the concentration polarization. Surface diffusion has been included by some,[58] but its importance is still not entirely known, especially for the various species that may participate in charge-transfer reactions. A more recent analysis by Janardhanan and Deutschmann[169] shows that surface diffusion does not lead to concentration losses in solid oxide fuel cells, but the authors suggest that current-limiting behavior resulting from concentration gradients may originate from the back diffusion of product species at the channel/electrode interface. This effect will only be important for low flow velocities in the channels, giving rise to species diffusion velocities on the same order as the mean flow velocity.

Ohmic overpotential. The three fundamental overpotentials appearing in Eq. 8 describing sources of voltage loss in a fuel cell are the activation overpotentials $\eta_{\text{act},i}$ (due to losses associated with charge-transfer kinetics), concentration overpotentials $\eta_{\text{conc},i}$ (due to losses associated with mass-transport limitations), and the ohmic overpotential η_{ohm} (due to ion- and electron-transport resistances). As in previous sections, the subscript i is used to indicate each electrode ("a" for anode and "c" for cathode). The activation overpotentials are introduced and discussed in the ensuing sections. The

concentration overpotentials and their dependence on mass transport were discussed in the foregoing sections. For the purposes of completeness, it is certainly worthwhile to briefly discuss losses associated with transport of charged species.

The ohmic overpotential η_{ohm}, due primarily to resistance of ion and electron transport, can be represented as[48]

$$\eta_{\text{ohm}} = \Phi_{e,a} - \Phi_{e,c} = iR_{\text{tot}} \tag{A-10}$$

where $R_{\text{tot}} = R_{\text{el}} + R_{\text{ed}}$ is the total area-specific cell resistance, including the solid electrolyte R_{el} and area-specific resistances in the electrodes R_{ed}. The overpotential is also written in terms of the potential difference across the electrolyte $\Phi_{e,a} - \Phi_{e,c}$. In composite cermet electrodes (e.g., Ni-YSZ anodes), the electrode resistance R_{ed} is usually negligible because of sufficient conduction paths for both ions and electrons. However, in ceramic electrodes such as an LSM cathode, the electrode ohmic resistance can be important.[48] The most significant contribution to the total cell resistance is due to the electrolyte R_{el}, which can be determined from the ionic conductivity of the electrolyte σ_{el} as $R_{\text{el}} = L_{\text{el}}/\sigma_{\text{el}}$, where L_{el} is the electrolyte thickness.[48] The ionic conductivity of the electrolyte is expressed as[48,170]

$$\sigma_{\text{el}} = \sigma_0 T^m \exp\left(-\frac{E_{\text{el}}}{RT}\right). \tag{A-11}$$

In this Arrhenius-type expression, σ_0 is the pre-factor, m is a dimensionless exponent (generally less than zero), and E_{el} is the activation energy of O^{2-} transport in the electrolyte. Note that R_{tot}, R_{el}, and R_{ed} are *not* related to the charge-transfer resistance R_{ct}; the former are associated with the ohmic resistance to transport of charge carriers (i.e., ions and electrons), while the latter is a resistance describing the kinetics of charge-transfer chemistry.

A charge-transfer resistance R_{ct} can be derived from the Butler-Volmer equation by taking the partial derivative of the current density i with respect to the activation overpotential,[47]

$$\begin{aligned} R_{\text{ct}}^{-1} &= A_{\text{TPB}} \left(\frac{\partial i}{\partial \eta_{\text{act},i}}\right)_{[X_k],T} \\ &= i_0 A_{\text{TPB}} \frac{F}{RT} \left[\beta_a \exp\left(\beta_a \frac{F\eta_{\text{act},i}}{RT}\right) \right. \\ &\qquad \left. + \beta_c \exp\left(-\beta_c \frac{F\eta_{\text{act},i}}{RT}\right)\right]. \end{aligned} \tag{A-12}$$

In this equation A_{TPB} is area of the TPB at which charge transfer occurs. At zero activation overpotential, one obtains a relationship between the exchange current density and charge-transfer resistance

$$R_{\text{ct}} = \frac{RT}{i_0 A_{\text{TPB}} F}, \tag{A-13}$$

where $\beta_a + \beta_c = 1$ has been used. The charge-transfer resistance can be determined from electrochemical impedance spectroscopy (EIS) measurements.[171,172]

References

1 S. C. Singhal and K. Kendall, *High Temperature Solid Oxide Fuel Cells: Fundamentals, Design and Applications*, Elsevier: Oxford, UK, 2003.
2 N. Q. Minh, *Solid State Ionics*, 2004, **174**, 271–277.
3 J. Larminie and A. Dicks, *Fuel Cell Systems Explained*, John Wiley & Sons: Chichester, England, 2000.
4 *Modeling Solid Oxide Fuel Cells: Methods, Procedures and Techniques*, ed. R. Bove and S. Ubertini, Springer, 2008.
5 EG&G Technical Services, Inc., *Fuel Cell Handbook*, USDOE-NETL: Morgantown, WV, USA, 7th edn, 2004.
6 R. J. Kee, H. Zhu, A. M. Sukeshini and G. S. Jackson, *Combust. Sci. Technol.*, 2008, **180**, 1207–1244.
7 R. J. Kee, H. Zhu and D. G. Goodwin, *Proc. Combust. Inst.*, 2005, **30**, 2379–2404.
8 M. D. Gross, J. M. Vohs and R. J. Gorte, *J. Mater. Chem.*, 2007, **17**, 3071–3077.
9 M. C. Williams, J. P. Strakey, W. A. Surdoval and L. C. Wilson, *Solid State Ionics*, 2006, **177**, 2039–2044.
10 J. B. Goodenough, *Nature*, 2000, **404**, 821–823.
11 O. Yamamoto, *Electrochim. Acta*, 2000, **45**, 2423–2435.
12 N. P. Brandon, S. Skinner and B. C. H. Steele, *Annu. Rev. Mater. Res.*, 2003, **33**, 183–213.
13 J. Fleig, *Annu. Rev. Mater. Res.*, 2003, **33**, 361–382.
14 J. W. Fergus, *Solid State Ionics*, 2006, **177**, 1529–1541.
15 S. P. Jiang and S. H. Chan, *J. Mater. Sci.*, 2004, **39**, 4405–4439.
16 E. V. Tsipis and V. V. Kharton, *J. Solid State Electrochem.*, 2008, **12**, 1039–1060.
17 W. Z. Zhu and S. C. Deevi, *Mater. Sci. Eng., A*, 2003, **362**, 228–239.
18 S. McIntosh and R. J. Gorte, *Chem. Rev.*, 2004, **104**, 4845–4865.
19 J. Hanna, *PhD thesis*, California Institute of Technology, Pasadena, CA, USA, 2010.
20 Y. Shi, N. Cai, C. Li, C. Bao, E. Croiset, J. Qian, Q. Hu and S. Wang, *J. Power Sources*, 2007, **172**, 235–245.
21 Y. Shi, N. Cai, C. Li, C. Bao, E. Croiset, J. Qian, Q. Hu and S. Wang, *J. Power Sources*, 2007, **172**, 246–252.
22 F. Lefebvre-Joud, G. Gauthier and J. Mougin, *J. Appl. Electrochem.*, 2009, **39**, 535–543.
23 M. Mogensen, N. M. Sammes and G. A. Tompsett, *Solid State Ionics*, 2000, **129**, 63–94.
24 B. C. H. Steele, *Solid State Ionics*, 2000, **129**, 95–110.
25 C. Lu, W. L. Worrell, R. J. Gorte and J. M. Vohs, *J. Electrochem. Soc.*, 2003, **150**, A354–A358.
26 Z. Zhan and S. A. Barnett, *J. Power Sources*, 2006, **157**, 422–429.
27 L. Jia, Y. Tian, Q. Liu, C. Xia, J. Yu, Z. Wang, Y. Zhao and Y. Li, *J. Power Sources*, 2010, **195**, 5581–5586.
28 E. P. Murray, T. Tsai and S. A. Barnett, *Nature*, 1999, **400**, 649–651.
29 E. S. Putna, J. Stubenrauch, J. M. Vohs and et al., *Langmuir*, 1995, **11**, 4832–4837.
30 A. Atkinson, S. Barnett, R. J. Gorte, J. T. S. Irvine, A. J. McEvoy, M. Mogensen, S. C. Singhal and J. Vohs, *Nat. Mater.*, 2004, **3**, 17–27.
31 M. Mogensen and K. Kammer, *Annu. Rev. Mater. Res.*, 2003, **33**, 321–331.
32 L. Yang, Y. Choi, W. Qin, H. Chen, K. Blinn, M. Liu, P. Liu, J. Bai, T. A. Tyson and M. Liu, *Nat. Commun.*, 2011, **2**, 357.
33 Y. Jiang and A. V. Virkar, *J. Electrochem. Soc.*, 2003, **150**, A942–A951.
34 J. Liu and S. A. Barnett, *Solid State Ionics*, 2003, **158**, 11–16.
35 Y. Lin, Z. Zhan, J. Liu and S. A. Barnett, *Solid State Ionics*, 2005, **176**, 1827–1835.
36 Z. Shao, J. Mederos, W. C. Chueh and S. M. Haile, *J. Power Sources*, 2006, **162**, 589–596.
37 T. Hibino, A. Hashimoto, M. Yano, M. Suzuki and M. Sano, *Electrochim. Acta*, 2003, **48**, 2531–2537.
38 S. Park, J. M. Vohs and R. J. Gorte, *Nature*, 2000, **404**, 265–267.
39 Z. Zhan and S. A. Barnett, *Science*, 2005, **308**, 844–847.

40 E. S. Hecht, G. K. Gupta, H. Zhu, A. M. Dean, R. J. Kee, L. Maier and O. Deutschmann, *Appl. Catal., A*, 2005, **295**, 40–51.

41 V. M. Janardhanan and O. Deutschmann, *J. Power Sources*, 2006, **162**, 1192–1202.

42 D. G. Goodwin, Solid Oxide Fuel Cells IX, 2005, pp. 699–707.

43 D. G. Goodwin, H. Zhu, A. M. Colclasure and R. J. Kee, *J. Electrochem. Soc.*, 2009, **156**, B1004–B1021.

44 S. C. DeCaluwe, H. Zhu, R. J. Kee and G. S. Jackson, *J. Electrochem. Soc.*, 2008, **155**, B538–B546.

45 W. G. Bessler, S. Gewies and M. Vogler, *Electrochim. Acta*, 2007, **53**, 1782–1800.

46 V. Yurkiv, D. Starukhin, H.-R. Volpp and W. G. Bessler, *J. Electrochem. Soc.*, 2011, **158**, B5–B10.

47 H. Zhu and R. J. Kee, *J. Power Sources*, 2003, **117**, 61–74.

48 H. Zhu, R. J. Kee, V. M. Janardhanan, O. Deutschmann and D. G. Goodwin, *J. Electrochem. Soc.*, 2005, **152**, A2427–A2440.

49 W. Y. Lee, D. Wee and A. F. Ghoniem, *J. Power Sources*, 2009, **186**, 417–427.

50 P. Chinda, S. Chanchaona, P. Brault and W. Wechsatol, *J. Sustainable Energy & Environ.*, 2010, **1**, 185–196.

51 D. G. Goodwin, *Cantera*, 2001–2005, http://code.google.com/p/cantera/.

52 R. J. Kee, H. Zhu and D. G. Goodwin, *J. Combust. Soc. Japan*, 2005, **47**, 192–204.

53 J.-W. Kim, A. V. Virkar, K.-Z. Fung, K. Mehta and S. C. Singhal, *J. Electrochem. Soc.*, 1999, **146**, 69–78.

54 F. Zhao and A. V. Virkar, *J. Power Sources*, 2005, **141**, 79–95.

55 Y. Shi, C. Li and N. Cai, *J. Power Sources*, 2011, **196**, 5526–5537.

56 A. J. Bard and L. R. Faulkner, *Electrochemical Methods: Fundamentals and Applications*, John Wiley & Sons: New York, 2nd edn, 2000.

57 W. Y. Lee, *MSc thesis*, Massachusetts Institute of Technology, Cambridge, MA, USA, 2006.

58 Y. Shi, N. Cai and C. Li, *J. Power Sources*, 2007, **164**, 639–648.

59 R. J. Kee, M. E. Coltrin and P. Glarborg, *Chemically Reacting Flow: Theory and Practice*, John Wiley & Sons: Hoboken, NJ, USA, 2003.

60 R. Suwanwarangkul, E. Croiset, M. W. Fowler, P. L. Douglas, E. Entchev and M. A. Douglas, *J. Power Sources*, 2003, **122**, 9–18.

61 E. A. Mason and A. P. Malinauskas, *Gas Transport in Porous Media: The Dusty-Gas Model*, Elsevier: New York, 1983.

62 W. K. S. Chiu, A. S. Joshi and K. N. Grew, *Eur. Phys. J. Special Topics*, 2009, **171**, 159–165.

63 A. S. Joshi, A. A. Peracchio, K. N. Grew and W. K. S. Chiu, *J. Phys. D: Appl. Phys.*, 2007, **40**, 2961–2971.

64 A. S. Joshi, A. A. Peracchio, K. N. Grew and W. K. S. Chiu, *J. Phys. D: Appl. Phys.*, 2007, **40**, 7593–7600.

65 H. Iwai, N. Shikazono, T. Matsui, H. Teshima, M. Kishimoto, R. Kishida, D. Hayashi, K. Matsuzaki, D. Kanno, M. Saito, H. Muroyama, K. Eguchi, N. Kasagi and H. Yoshida, *J. Power Sources*, 2010, **195**, 955–961.

66 J. J. R. Izzo, A. S. Joshi, K. N. Grew, W. K. S. Chiu, A. Tkachuk, S. H. Wang and W. Yun, *J. Electrochem. Soc.*, 2008, **155**, B504–B508.

67 B. Rüger, J. Joos, A. Weber, T. Carraro and E. Ivers-Tiffée, *ECS Trans.*, 2009, **25**, 1211–1220.

68 J. R. Wilson, M. Gameiro, K. Mischaikow, W. Kalies, P. W. Voorhees and S. A. Barnett, *Microsc. Microanal.*, 2009, **15**, 71–77.

69 J. R. Wilson and S. A. Barnett, *Electrochem. Solid-State Lett.*, 2008, **11**, B181–B185.

70 J. R. Wilson, W. Kobsiriphat, R. Mendoza, H.-Y. Chen, J. M. Hiller, D. J. Miller, K. Thornton, P. W. Voorhees, S. B. Adler and S. A. Barnett, *Nat. Mater.*, 2006, **5**, 541–544.

71 J. O. Bockris, A. K. N. Reddy and M. Gamboa-Aldeco, *Modern Electrochemistry 2A: Fundamentals of Electrodics*, Kluwer Academic/Plenum Publishers: New York, 2nd edn, 2000.

72 C. Sun and U. Stimming, *J. Power Sources*, 2007, **171**, 247–260.

73 R. E. Williford, L. A. Chick, G. D. Maupin, S. P. Simner and J. W. Stevenson, *J. Electrochem. Soc.*, 2003, **150**, A1067–A1072.

74 P. Holtappels, L. G. J. de Haart and U. Stimming, *J. Electrochem. Soc.*, 1999, **146**, 1620–1625.

75 S. P. Jiang and S. P. S. Badwal, *Solid State Ionics*, 1999, **123**, 209–224.

76 B. de Boer, *PhD thesis*, University of Twente, Netherlands, 1998.

77 J. Mizusaki, H. Tagawa, T. Saito, K. Kamitani, T. Yamamura, K. Hirano, S. Ehara, T. Takagi, T. Hikita, M. Ippommatsu, S. Nakagawa and K. Hashimoto, *J. Electrochem. Soc.*, 1994, **141**, 2129–2134.

78 A. Bieberle, *PhD thesis*, Swiss Federal Institute of Technology, Zurich, Switzerland, 2000.

79 A. Bieberle and L. J. Gauckler, *Solid State Ionics*, 2002, **146**, 23–41.

80 W. G. Bessler, J. Warnatz and D. G. Goodwin, *Solid State Ionics*, 2007, **177**, 3371–3383.

81 M. Mogensen and T. Lindegaard, Solid Oxide Fuel Cells III, 1993, pp. 484–493.

82 M. Mogensen, S. Sunde and S. Primdahl, author, 1996, pp. 77–100.

83 S. P. Jiang and S. P. S. Badwal, *J. Electrochem. Soc.*, 1997, **144**, 3777–3784.

84 A. Bieberle, L. P. Meier and L. J. Gauckler, *J. Electrochem. Soc.*, 2001, **148**, A646–A656.

85 M. Vogler, A. Bieberle-Hütter, L. Gauckler, J. Warnatz and W. G. Bessler, *J. Electrochem. Soc.*, 2009, **156**, B663–B672.

86 S. Gewies and W. G. Bessler, *J. Electrochem. Soc.*, 2008, **155**, B937–B952.

87 M. Ihara, T. Kusano and C. Yokoyama, *J. Electrochem. Soc.*, 2001, **148**, A209–A219.

88 R. E. Williford and L. A. Chick, *Surf. Sci.*, 2003, **547**, 421–437.

89 B. Habibzadeh, *PhD thesis*, University of Maryland, College Park, MD, USA, 2007.

90 A. M. Sukeshini, B. Habibzadeh, B. P. Becker, C. A. Stoltz, B. W. Eichhorn and G. S. Jackson, *J. Electrochem. Soc.*, 2006, **153**, 705–715.

91 Y. Matsuzaki and I. Yasuda, *J. Electrochem. Soc.*, 2000, **147**, 1630–1635.

92 K. Eguchi, H. Kojo, T. Takeguchi, R. Kikuchi and K. Sasaki, *Solid State Ionics*, 2002, **152/153**, 411–416.

93 K. Sasaki, Y. Hori, R. Kikuchi, K. Eguchi, A. Ueno, H. Takeuchi, M. Aizawa, K. Tsujimoto, H. Tajiri, N. Nishikawa and Y. Uchida, *J. Electrochem. Soc.*, 2002, **149**, A227–A233.

94 T. H. Etsell and S. N. Flengas, *J. Electrochem. Soc.*, 1971, **118**, 1890–1900.

95 G. Ø. Lauvstad, R. Tunold and S. Sunde, *J. Electrochem. Soc.*, 2002, **149**, E497–E505.

96 J. Mizusaki, H. Tagawa, Y. Miyaki, S. Yamauchi, K. Fueki, I. Koshiro and K. Hirano, *Solid State Ionics*, 1992, **53–56**, 126–134.

97 R. J. Aaberg, R. Tunold, S. Tjelle and R. Ødegård, High Temperature Electrochemistry: Ceramics and Metals, 1996, pp. 511–518.

98 G. Ø. Lauvstad, R. Tunold and S. Sunde, *J. Electrochem. Soc.*, 2002, **149**, E506–E514.

99 F. Z. Boulenouar, K. Yashiro, M. Oishi, A. Kaimai, Y. Nigara, T. Kawada and J. Mizusaki, Solid Oxide Fuel Cells VII, 2001, pp. 759–768.

100 T. Setoguchi, K. Okamoto, K. Eguchi and H. Arai, *J. Electrochem. Soc.*, 1992, **139**, 2875–2880.

101 P. Holtappels, L. G. J. de Haart, U. Stimming, I. C. Vinke and M. Mogensen, *J. Appl. Electrochem.*, 1999, **29**, 561–568.

102 J. R. Rostrup-Nielsen, *Steam Reforming Catalysts*, Springer-Verlag: Berlin, 1984.

103 A. Weber, B. Sauer, A. C. Müller, D. Herbstritt and E. Ivers-Tiffée, *Solid State Ionics*, 2002, **152/153**, 543–550.

104 O. Costa-Nunes, R. J. Gorte and J. M. Vohs, *J. Power Sources*, 2005,

141, 241–249.
105 S. Park, R. Craciun, J. M. Vohs and R. J. Gorte, *J. Electrochem. Soc.*, 1999, **146**, 3603–3605.
106 C. Li, Y. Shi and N. Cai, *J. Power Sources*, 2011, **196**, 754–763.
107 P. Desclaux, S. Nürnberger, M. Rzepka and U. Stimming, *Int. J. Hydrogen Energy*, 2011, **36**, 10278–10281.
108 S. Nürnberger, R. Bußar, P. Desclaux, B. Franke, M. Rzepka and U. Stimming, *Energy Environ. Sci.*, 2010, **3**, 150–153.
109 T. Horita, N. Sakai, T. Kawada, H. Yokokawa and M. Dokiya, *J. Electrochem. Soc.*, 1995, **142**, 2621–2624.
110 T. M. Gür and R. A. Huggins, *J. Electrochem. Soc.*, 1992, **139**, L95–L97.
111 B. R. Alexander, R. E. Mitchell and T. M. Gür, *J. Electrochem. Soc.*, 2011, **158**, B505–B513.
112 T. M. Gür, M. Homel and A. V. Virkar, *J. Power Sources*, 2010, **195**, 1085–1090.
113 T. M. Gür, *J. Electrochem. Soc.*, 2010, **157**, B751–B759.
114 A. C. Lee, R. E. Mitchell and T. M. Gür, *J. Power Sources*, 2009, **194**, 774–785.
115 A. C. Lee, S. Li, R. E. Mitchell and T. M. Gür, *Electrochem. Solid-State Lett.*, 2008, **11**, B20–B23.
116 S. Li, A. C. Lee, R. E. Mitchell and T. M. Gür, *Solid State Ionics*, 2008, **179**, 1549–1552.
117 S. Hasegawa and M. Ihara, *J. Electrochem. Soc.*, 2008, **155**, B58–B63.
118 M. Ihara, K. Matsuda, H. Sato and C. Yokoyama, *Solid State Ionics*, 2004, **175**, 51–54.
119 R. J. Gorte, H. Kim and J. M. Vohs, *J. Power Sources*, 2002, **106**, 10–15.
120 J. R. Rostrup-Nielsen, J. Sehested and J. K. Nørskov, *Adv. Catal.*, 2002, **47**, 65–139.
121 G. K. Gupta, E. S. Hecht, H. Zhu, A. M. Dean and R. J. Kee, *J. Power Sources*, 2006, **156**, 434–447.
122 K. M. Walters, A. M. Dean, H. Zhu and R. J. Kee, *J. Power Sources*, 2003, **123**, 182–189.
123 *Catalysis: Science and Technology*, ed. J. R. Anderson and M. Boudart, Springer-Verlag: Berlin; New York, 1984, vol. 5.
124 S. Helveg, C. López-Cartes, J. Sehested, P. L. Hansen, B. S. Clausen, J. R. Rostrup-Nielsen, F. Abild-Pedersen and J. K. Nørskov, *Nature*, 2004, **427**, 426–429.
125 T. Kim, G. Liu, M. Boaro, S. Lee, J. M. Vohs, R. J. Gorte, O. H. Al-Madhi and B. O. Dabbousi, *J. Power Sources*, 2006, **155**, 231–238.
126 J. Appel, H. Bockhorn and M. Frenklach, *Combust. Flame*, 2000, **121**, 122–136.
127 A. Kazakov, H. Wang and M. Frenklach, *Combust. Flame*, 1995, **100**, 111–120.
128 C. Y. Sheng and A. M. Dean, *J. Phys. Chem. A*, 2004, **108**, 3772–3783.
129 H. Kim, C. Lu, W. L. Worrell, J. M. Vohs and R. J. Gorte, *J. Electrochem. Soc.*, 2002, **149**, A247–A250.
130 J.-H. Koh, B.-S. Kang, H. C. Lim and Y.-S. Yoo, *Electrochem. Solid-State Lett.*, 2001, **4**, A12–A15.
131 S. Deshpande, S. Patil, S. V. N. T. Kuchibhatia and S. Seal, *Appl. Phys. Lett.*, 2005, **87**, 133113.
132 B. C. H. Steele, P. H. Middleton and R. A. Rudkin, *Solid State Ionics*, 1990, **40/41**, 388–393.
133 S. McIntosh, J. M. Vohs and R. J. Gorte, *J. Electrochem. Soc.*, 2003, **150**, A470–A476.
134 X.-F. Ye, B. Huang, S. R. Wang, Z. R. Wang, L. Xiong and T. L. Wen, *J. Power Sources*, 2007, **164**, 203–209.
135 S. Lee, J. M. Vohs and R. J. Gorte, *J. Electrochem. Soc.*, 2004, **151**, A1319–A1323.
136 Z. Xie, W. Zhu, B. Zhu and C. Xia, *Electrochim. Acta*, 2006, **51**, 3052–3057.
137 O. Costa-Nunes, J. M. Vohs and R. J. Gorte, *J. Electrochem. Soc.*, 2003, **150**, A858–A863.
138 T. Hibino, A. Hashimoto, K. Asano, M. Yano, M. Suzuki and M. Sano, *Electrochem. Solid-State Lett.*, 2002, **5**, A242–A244.
139 F. Besenbacher, I. Chorkendorff, B. S. Clausen, B. Hammer, A. M. Molenbroek, J. K. Nørskov and I. Stensgaard, *Science*, 1998, **279**, 1913–1915.
140 J. R. Rostrup-Nielsen and I. Alstrup, *Catal. Today*, 1999, **53**, 311–316.
141 N. C. Triantafyllopoulos and S. G. Neophytides, *J. Catal.*, 2006, **239**, 187–199.
142 I. Gavrielatos, V. Drakopoulos and S. G. Neophytides, *J. Catal.*, 2008, **259**, 75–84.
143 R. Schneider, D. Kiessling, G. Wendt, W. Burckhardt and G. Winterstein, *Catal. Today*, 1999, **47**, 429–435.
144 L. Forni and I. Rossetti, *Appl. Catal., B*, 2002, **38**, 29–37.
145 V. C. Belessi, A. K. Ladavos and P. J. Pomonis, *Appl. Catal., B*, 2001, **31**, 183–194.
146 J. C. Fisher and S. S. C. Chuang, *Catal. Commun.*, 2009, **10**, 772–776.
147 Y.-H. Huang, R. I. Dass, J. C. Denyszyn and J. B. Goodenough, *J. Electrochem. Soc.*, 2006, **153**, A1266–A1272.
148 Y.-H. Huang, R. I. Dass, Z.-L. Xing and J. B. Goodenough, *Science*, 2006, **312**, 254–257.
149 A. L. Sauvet and J. T. S. Irvine, *Solid State Ionics*, 2004, **167**, 1–8.
150 A.-L. Sauvet, J. Fouletier, F. Gaillard and M. Primet, *J. Catal.*, 2002, **209**, 25–34.
151 A. L. Sauvet and J. Fouletier, *Electrochim. Acta*, 2001, **47**, 987–995.
152 J. C. Ruiz-Morales, J. Canales-Vázquez, J. P. na Martinez, D. M. López and P. N. nez, *Electrochim. Acta*, 2006, **52**, 278–284.
153 G. Pudmich, B. A. Boukamp, M. Gonzalez-Cuenca, W. Jungen, W. Zipprich and F. Tietz, *Solid State Ionics*, 2000, **135**, 433–438.
154 A. Sin, E. Kopnin, Y. Dubitsky, A. Zaopo, A. S. Aricò, L. R. Gullo, D. La Rosa and V. Antonucci, *J. Power Sources*, 2005, **145**, 68–73.
155 S. P. Jiang, X. J. Chen, S. H. Chan and J. T. Kwok, *J. Electrochem. Soc.*, 2006, **153**, A850–A856.
156 X. J. Chen, Q. L. Liu, S. H. Chan, N. P. Brandon and K. A. Khor, *Fuel Cells Bulletin*, 2007, **2007**, 12–16.
157 P. Vernoux, M. Guillodo, J. Fouletier and A. Hammou, *Solid State Ionics*, 2000, **135**, 425–431.
158 Y. Matsuzaki and I. Yasuda, Solid Oxide Fuel Cells VII, 2001, pp. 769–779.
159 Y. Matsuzaki and I. Yasuda, *Solid State Ionics*, 2000, **132**, 261–269.
160 E. H. Edwin, H. Karoliussen and R. Odegard, Solid Oxide Fuel Cells V, 1997, pp. 839–846.
161 J. P. Trembly, A. I. Marquez, T. R. Ohrn and D. J. Bayless, *J. Power Sources*, 2006, **158**, 263–273.
162 Z. Cheng, S. Zha and M. Liu, *J. Electrochem. Soc.*, 2006, **153**, L23.
163 Z. Cheng, S. Zha and M. Liu, *J. Electrochem. Soc.*, 2006, **153**, A1302–A1309.
164 R. Mukundan, E. L. Brosha and F. H. Garzon, *Electrochem. Solid-State Lett.*, 2004, **7**, A5–A7.
165 C. M. Grgicak, M. M. Pakulska, J. S. O'Brien and J. B. Giorgi, *J. Power Sources*, 2008, **183**, 26–33.
166 D. S. Monder, K. Nandakumar and K. T. Chuang, *J. Power Sources*, 2006, **162**, 400–414.
167 M. Liu, G. Wei, J. Luo, A. R. Sanger and K. T. Chuang, *J. Electrochem. Soc.*, 2003, **150**, A1025–A1029.
168 N. U. Pujare, K. W. Semkow and A. F. Sommells, *J. Electrochem. Soc.*, 1987, **134**, 2639–2643.
169 V. M. Janardhanan and O. Deutschmann, *Electrochim. Acta*, 2011, **56**, 9775–9782.
170 L. Ying, G. Jiang-Hong, T. Zi-Long, X. Yu-Sheng and Z. Zhong-Tai, *Acta Phys.-Chim. Sin.*, 2001, **17**, 792–796.
171 *Impedance Spectroscopy, Theory, Experiment, and Applications*, ed. E. Barsoukov and J. R. Macdonald, John Wiley & Sons: Hoboken, NJ,

USA, 2nd edn, 2005.
172 M. E. Orazem and B. Tribollet, *Electrochemical Impedance Spectroscopy*, John Wiley & Sons: Hoboken, NJ, USA, 2008.